

Recommendations for Static Electricity Meters Beyond Standards Requirements

Renán Gabriel Quijano Cetina

A thesis submitted for the degree of Doctor of Philosophy to
Department of Electronic and Electrical Engineering
University of Strathclyde, Glasgow

May 16, 2022

This thesis is the result of the author's original research. It has been composed by the author and has not been previously submitted for examination which has led to the award of a degree.

The copyright of this thesis belongs to the author under the terms of the United Kingdom Copyright Acts as qualified by University of Strathclyde Regulation 3.50. Due acknowledgement must always be made of the use of any material contained in, or derived from, this thesis.

Abstract

The ongoing smart grid transition involves large-scale integration of power electronic converters, along with intelligence gained from the transfer of measurement information at all levels of the grid. This requires an accurate response of electricity meters, which must be designed to cater for present and future power network conditions. In particular, the accuracy of electricity meters under nonsinusoidal conditions is critical for industry and electricity consumers. Numerous studies have been conducted in order to identify the causes of erroneous measurements reported by static electricity meters when exposed to nonsinusoidal voltage and current signals, but there is a gap in these studies relating to nonsinusoidal situations.

This thesis addresses this gap by providing a clear understanding of static electricity meter response to nonsinusoidal signals from typical power electronic equipment in modern grids. The thesis proposes a methodology for testing the accuracy of electricity meters beyond standard requirements, including a set of waveforms with fast-changing waveform phenomena. The results of applying such waveforms exposes limitations in energy metering integrated circuit (IC) technology produced by its internal components.

An important contribution of this thesis is the detailed investigation of the impact of crest factor and power factor in metering error. This thesis proposes, for the first time, a new type of test designed to provide a consistent method for comparing metering IC capabilities, and to define the limits of accurate operation. This work can be used as a starting point to define future standards for evaluating the accuracy of static electricity meters and current transducers exposed to realistic fast-changing currents.

Furthermore, this thesis proposes a novel method for compensating the errors in measurements reported by electricity meters under certain nonsinusoidal conditions. This contribution thereby provides a practical solution to address the identified drop in performance, which will ensure the robust operation of meters even under extreme operating conditions in future grids.

Acknowledgements

I would like to express my sincerely gratitude to my supervisors Dr Steven Blair and Prof Graeme Burt for the support I got from them during my PhD journey. They have been a truly inspiration for me and I have learned so much from them.

I would also like to thank Dr Andrew Roscoe for the opportunity to start a PhD at Strathclyde. From the beginning, he pushed me in the right direction and I consider him a great mentor and friend.

I ought to extend my gratitude to the National Physical Laboratory, for the opportunity to be part of the Post Graduate Institute, where I learned lots of things and had a great time as well. Special thanks to Dr. Paul Wright who was my external supervisor, giving me always good advice. Also many thanks to Linden Fradet and NPL staff who supported my research and enriched my experience.

I owe a lot of gratitude to the colleagues at the Dynamic Power System Laboratory and TIC building. I truly appreciate the collaborative working environment where I learned and met new friends. Thanks Richard, Yljon, Joanna, Syiska, Christian, Rafa and Mazher for your continuous help and friendship.

I wish to express my gratitude to the Mexican Council of Science and Technology CONACYT to fund my research project and to the Autonomous University of Yucatan for the support during this journey.

Finalmente, los agradecimientos más especiales son para mi familia, a quienes debo todo lo que soy en esta vida. Muchas gracias mamá, siempre has sido la mejor. Muchas gracias papá, Rossana, Patty y David. A ustedes les dedico esta tesis.

Todo el esfuerzo hubiera sido en vano si no hubiera contado con el apoyo incondicional de mi amada esposa Cecilia, a quien debo mucho y a quien también le dedico este trabajo. Ella y mi hija Lucía son mi principal motivación para seguir adelante.

Contents

| | |
|---|-------------|
| Abstract | iii |
| Acknowledgements | iv |
| List of Figures | ix |
| List of Tables | xiv |
| Glossary of Abbreviations | xvii |
| 1 Introduction | 1 |
| 1.1 Introduction to the Research | 1 |
| 1.2 Research Motivation | 3 |
| 1.3 Thesis Aim and Objectives | 5 |
| 1.4 Principal Contributions | 6 |
| 1.5 Thesis Overview | 7 |
| 1.6 Associated Publications | 8 |
| 2 Review of Standard Requirements and Electric Power Definitions for Static Electricity Meters | 10 |
| 2.1 Introduction | 10 |
| 2.2 Electric Power Quantities Definitions | 11 |
| 2.2.1 Single-Phase: sinusoidal | 12 |
| 2.2.2 Single-Phase: nonsinusoidal | 15 |
| 2.2.3 Supplementary Quantities | 21 |

Contents

| | | |
|----------|--|-----------|
| 2.3 | Standards and Regulations for Electricity Meters | 22 |
| 2.3.1 | North American Standards | 23 |
| 2.3.1.1 | ANSI C12 Series | 23 |
| 2.3.2 | International Standards | 23 |
| 2.3.2.1 | IEC Standards | 23 |
| 2.3.2.2 | MID Standards | 25 |
| 2.3.2.3 | Accuracy Tests | 27 |
| 2.3.3 | Supporting Standards/Documents | 31 |
| 2.3.3.1 | OIML R 46 | 31 |
| 2.4 | Calculating Electricity Meter Maximum Permissible Error | 33 |
| 2.4.1 | Chapter Summary | 38 |
| 3 | Analysis of Static Electricity Meter Design and Reported Accuracy | |
| | Errors | 40 |
| 3.1 | Introduction | 40 |
| 3.2 | Analogue Front-End | 41 |
| 3.2.1 | Sensors/Transducers | 41 |
| 3.2.1.1 | Voltage Sensors | 42 |
| 3.2.1.2 | Current Sensors | 43 |
| 3.2.2 | Anti-Aliasing Filter | 44 |
| 3.2.3 | Gain Stage | 44 |
| 3.2.4 | Protection and Isolation Components | 45 |
| 3.2.5 | Analogue to Digital Converter | 46 |
| 3.3 | Digital Signal Processing | 49 |
| 3.3.1 | Energy Metering Integrated Circuits | 50 |
| 3.3.2 | Gain, Offset and Phase Adjustment | 53 |
| 3.3.3 | Digital Filters | 53 |
| 3.3.4 | Digital Integrator | 54 |
| 3.3.5 | Measurement of Electric Power Quantities | 54 |
| 3.3.6 | Energy Accumulation | 55 |

Contents

| | | |
|----------|---|-----------|
| 3.4 | Reported Accuracy Errors in Static Electricity Meters | 56 |
| 3.4.1 | Conducted Electromagnetic Interference on Electricity Meters . . | 57 |
| 3.4.2 | Comparative Tests | 58 |
| 3.4.3 | Performance Tests | 59 |
| 3.4.4 | Testbed and Calibration Under Nonsinusoidal Conditions Proposals | 60 |
| 3.5 | Chapter Summary | 61 |
| 4 | Energy Metering Integrated Circuit Tests and Modelling | 63 |
| 4.1 | Introduction | 63 |
| 4.2 | Experimental Tests Description | 65 |
| 4.2.1 | Sinusoidal Tests | 65 |
| 4.2.2 | Standard nonsinusoidal Tests | 66 |
| 4.2.3 | Real-world Current Signal Tests | 66 |
| 4.2.4 | Crest Factor Tests | 67 |
| 4.3 | Measurement System Description | 70 |
| 4.3.1 | Electrical Current and Voltage Level Definitions | 76 |
| 4.3.2 | Electricity Meter Design | 76 |
| 4.3.2.1 | ADE7878A Energy Metering IC | 77 |
| 4.3.2.2 | ADE7878A Metrics | 78 |
| 4.4 | ADE7878A Model | 89 |
| 4.4.1 | ADE7878A Model Requirements | 89 |
| 4.4.2 | ADE7878A Model Implementation | 89 |
| 4.4.3 | ADE7878A Model Operation | 91 |
| 4.4.4 | ADE7878A IC Model Accuracy | 94 |
| 4.5 | Chapter Summary | 96 |
| 5 | Experimental Results and Analysis | 98 |
| 5.1 | Sinusoidal Tests Results | 99 |
| 5.1.1 | Phase Angle Error | 101 |
| 5.1.2 | Total active power at $PF = 0$ and Reactive Power at $PF = 1$. . | 102 |
| 5.1.3 | Sinusoidal Phase Swept Test Results | 105 |

Contents

| | | |
|----------|--|------------|
| 5.2 | Standard nonsinusoidal Test Results | 107 |
| 5.3 | Real-world Current Signal Tests Results | 112 |
| 5.4 | Crest Factor Tests Results | 116 |
| 5.4.1 | ADE7878A Waveform Sampling | 121 |
| 5.5 | Chapter Summary | 125 |
| 6 | Energy Measurements Error Compensation for Current Signals with High Crest Factor | 126 |
| 6.1 | CF Measurement Error Compensation | 127 |
| 6.2 | Total Active Energy Measurement Error compensation | 129 |
| 6.3 | Total Apparent Energy Measurement Error Compensation | 132 |
| 6.4 | Fundamental Active Energy Measurement Error Compensation | 134 |
| 6.5 | ADE7878A IC model measurement error estimation for high crest factor current signals | 137 |
| 6.6 | Applying Error Compensation to ADE7878A IC Measurements of High Crest Factor Current Signals | 138 |
| 6.7 | Recommendations for Electricity Meter Designers | 138 |
| 6.8 | Chapter Summary | 139 |
| 7 | Conclusions and Future Work | 140 |
| 7.1 | Conclusions | 140 |
| 7.2 | Future Work | 143 |
| 7.2.1 | Analysis of the Effect of Signal Parameters in Voltage and Current Transducers Accuracy | 144 |
| 7.2.2 | Analysis of the Effect of Signal Parameters in Metering IC Digital Integrators | 144 |
| 7.2.3 | Further Evaluation of the Effect of Different Values of Signal Slope in Metering IC Accuracy | 145 |
| 7.2.4 | Refinement of Metering IC Model | 145 |
| 7.2.5 | Determine a suitable crest factor threshold for measurement error compensation | 145 |

Contents

| | |
|--|------------|
| A Total Apparent Power S Decomposition | 147 |
| B Rated Operating Accuracy Test Conditions | 151 |
| C ADE7878A Calibration | 153 |
| D Waveform Parameters | 161 |
| E Step-like Shaped Current Waveforms Gallery | 163 |
| F ADE7878A Model Calculations | 170 |
| Bibliography | 179 |

List of Figures

| | | |
|------|---|----|
| 2.1 | Typical electromechanical electricity meter been replaced by static electricity meter | 11 |
| 2.2 | Sinusoidal waveform of instantaneous voltage v , instantaneous current i and instantaneous active power p | 14 |
| 2.3 | Nonsinusoidal waveform of “Peaked” signal: instantaneous voltage v , instantaneous current i and instantaneous total active power p | 16 |
| 2.4 | Peaked waveform harmonic current components | 17 |
| 2.5 | Harmonics test waveform. | 29 |
| 2.6 | d.c. and even harmonics test signal: waveform and Fourier analysis . . . | 30 |
| 2.7 | Odd harmonic test: phase fired waveform. | 31 |
| 2.8 | Sub-harmonic test: burst fired waveform | 32 |
| 2.9 | OIML R46 Quadriform voltage and current waveforms. | 33 |
| 2.10 | OIML R46 Peaked voltage and current waveforms. | 34 |
| 3.1 | Electricity meter analogue front-end. | 41 |
| 3.2 | Voltage sensors: inductive transformer and resistive voltage divider. . . | 42 |
| 3.3 | SAR ADC architecture | 47 |
| 3.4 | Sigma-delta ADC architecture | 47 |
| 3.5 | Single phase energy metering integrated circuit block diagram. | 51 |
| 4.1 | Standard nonsinusoidal tests waveforms. | 66 |
| 4.2 | Real-world current signal tests waveforms. | 67 |
| 4.3 | Crest factor tests waveforms. | 68 |

List of Figures

| | | |
|------|--|-----|
| 4.4 | Experimental setup. | 72 |
| 4.5 | Signal generator LabVIEW application flow chart. | 74 |
| 4.6 | ADE7878AEBZ board and LabVIEW interface application flow chart. | 75 |
| 4.7 | EVAL-ADE7878AEBZ evaluation board simplified diagram. | 76 |
| 4.8 | ADE7878A rms signal processing. | 79 |
| 4.9 | ADE7878A phase angle calculation: measured time delay between voltage and current signals [73]. | 81 |
| 4.10 | ADE7878A IC model total active energy calculation block diagram [73]. | 86 |
| 4.11 | ADE7878A IC model total apparent energy calculation block diagram [73]. | 87 |
| 4.12 | ADE7878A IC model total reactive energy calculation block diagram [73]. | 88 |
| 4.13 | ADE7878A IC model functional block diagram (single-phase). | 90 |
| 4.14 | ADE7878A IC model graphical user interface. | 92 |
| 4.15 | ADE7878A IC model full block diagram. | 93 |
| 4.16 | Error difference between IC's model and IC's real measurements | 95 |
| | | |
| 5.1 | Sinusoidal tests results from 0.2 to 1% ADC full scale. | 100 |
| 5.2 | Sinusoidal tests results from 1 to 100% ADC full scale. | 101 |
| 5.3 | Phase angle error. | 102 |
| 5.4 | Total active power absolute error. | 103 |
| 5.5 | Total apparent power and total reactive power relative error. | 104 |
| 5.6 | Total apparent power and total active power relative error. | 105 |
| 5.7 | Total reactive power absolute error. | 105 |
| 5.8 | Total active power relative error versus phase shift. | 106 |
| 5.9 | Total reactive power relative error versus phase shift. | 107 |
| 5.10 | Voltage rms relative error. | 108 |
| 5.11 | Current rms relative error. | 108 |
| 5.12 | Total active power relative error. | 109 |
| 5.13 | Total apparent power relative error. | 109 |
| 5.14 | Total active energy relative error. | 110 |

List of Figures

| | | |
|------|--|-----|
| 5.15 | Fundamental active energy relative error. | 110 |
| 5.16 | Total apparent energy relative error. | 111 |
| 5.17 | Fundamental reactive energy relative error. | 111 |
| 5.18 | Voltage and current rms relative error. | 112 |
| 5.19 | Peak current relative error. | 113 |
| 5.20 | Total active power P and total apparent power S relative error. | 114 |
| 5.21 | Total active energy E and total apparent energy E_S relative error. | 115 |
| 5.22 | Fundamental active energy E_1 and fundamental reactive energy E_{Q_1} relative error. | 116 |
| 5.23 | “Leading” and “Falling” I_{rms} relative error vs crest factor. | 117 |
| 5.24 | “Leading” and “Falling” total apparent energy E_S relative error vs crest factor. | 118 |
| 5.25 | “Leading” and “Falling” i_{peak} relative error vs crest factor. | 118 |
| 5.26 | “Leading” and “Falling” total active energy E relative error vs crest factor. | 120 |
| 5.27 | “Leading” fundamental active energy E_1 relative error vs crest factor. | 121 |
| 5.28 | “Falling” fundamental active energy E_1 relative error vs crest factor. | 121 |
| 5.29 | ADC “leading” sampled waveforms. | 122 |
| 5.30 | ADC “1/8 leading” sampled waveform zoom-in. | 122 |
| 5.31 | ADC “falling” sampled waveforms. | 123 |
| 5.32 | ADC “1/8 falling” sampled waveform zoom-in. | 124 |
| 6.1 | Calculated CF_{meas} values versus true CF values. | 127 |
| 6.2 | CF_{meas} and CF_c relative error. | 129 |
| 6.3 | CF_c versus E relative error. | 130 |
| 6.4 | E_{meas} and E_c relative error. | 131 |
| 6.5 | CF_C versus E_{Smeas} relative error. | 132 |
| 6.6 | E_{Smeas} and E_{Sc} relative error. | 134 |
| 6.7 | E_{1meas} relative error versus CF_C | 135 |
| 6.8 | E_{1meas} and E_{1c} relative error. | 136 |

List of Figures

| | | |
|------|--|-----|
| 6.9 | Modified ADE7878A IC model functional block diagram (single-phase). | 137 |
| 6.10 | Measurement error compensation flow diagram. | 138 |
| A.1 | Traditional power triangle | 147 |
| A.2 | IEEE 1459 total apparent power S decomposition | 148 |
| A.3 | IEEE 1459 total apparent power S decomposition: geometrical representation | 149 |
| A.4 | IEEE 1459 total apparent power S decomposition: geometrical representation of a sinusoidal case | 149 |
| A.5 | IEEE 1459 nonactive apparent power S_N decomposition: geometrical representation | 150 |
| D.1 | Positive-going transition | 161 |
| D.2 | Negative-going transition | 162 |
| E.1 | Pulsed current waveforms drawn by a set of pure active load with dimmer and two CFLs | 163 |
| E.2 | Current waveform NRC WF1363 | 164 |
| E.3 | Pulsed current waveform drawn by a LED TV | 164 |
| E.4 | Current waveforms generated by remote control in combination with a water pump | 165 |
| E.5 | Current waveforms generated by a water pump with included dimmer used for fish ponds | 165 |
| E.6 | Current waveform generated by a set of 30 non-dimmable energy-saving lamps controlled by a dimmer set at 135 degrees | 166 |
| E.7 | Pulsed current measured waveforms of household appliances | 166 |
| E.8 | Theoretically designed step-like current waveforms: falling and rising edge dimming in the first quarter of a cycle | 167 |
| E.9 | Theoretically designed step-like current waveforms: falling and rising edge dimming in the second quarter of a cycle | 168 |

List of Figures

| | |
|--|-----|
| E.10 Theoretically designed step-like current waveforms: falling and rising edge dimming | 169 |
| F.1 ADE7878A IC model rms calculation. | 170 |
| F.2 ADE7878A IC model current peak value calculation. | 171 |
| F.3 ADE7878A IC model phase angle calculation. | 171 |
| F.4 ADE7878A IC model total active power calculation. | 172 |
| F.5 ADE7878A IC model total reactive power calculation. | 173 |
| F.6 ADE7878A IC model total apparent power calculation. | 173 |
| F.7 ADE7878A IC model total active energy calculation. | 174 |
| F.8 ADE7878A IC model fundamental active energy calculation. | 176 |
| F.9 ADE7878A IC model total reactive energy calculation. | 177 |
| F.10 ADE7878A IC model fundamental reactive energy calculation. | 178 |

List of Tables

| | | |
|-----|--|----|
| 2.1 | Percentage error limits for the accuracy classes 2, 1, 0.5S and 0.2S (IEC 62053-21/22:2021). | 24 |
| 2.2 | Percentage error limits for the accuracy classes A, B and C (EN 50470-1:2006+A1:2018). | 26 |
| 2.3 | Waveform THD at reference conditions. | 27 |
| 2.4 | Limits of error due to variation of influence quantities. | 28 |
| 2.5 | Percentage error limits for the accuracy classes A, B, C and D (OIML R 46). | 32 |
| 2.6 | Quadriform waveform harmonic content. | 34 |
| 2.7 | Peaked waveform harmonic content. | 35 |
| 2.8 | Harmonic content influence accuracy tests. | 39 |
| 3.1 | Current sensor technologies: benefits and drawbacks. | 43 |
| 3.2 | Simultaneous-sampling ADCs comparison. | 49 |
| 3.3 | Energy Metering ICs comparison. | 52 |
| 3.4 | Digital Filters: advantages and disadvantages. | 53 |
| 4.2 | Rigol DG952 AWG specifications. | 70 |
| 4.1 | Test waveforms parameters. | 71 |
| 4.3 | Raspberry 3 Model B+ specifications. | 73 |
| 4.4 | Definitions of meter quantities. | 76 |
| 4.5 | ADE7878A ADC's specifications. | 77 |
| 4.6 | ADE7878A measurements. | 78 |

List of Tables

| | | |
|-----|--|-----|
| 4.7 | ADE7878A IC model test results. | 94 |
| 4.8 | ADE7878A IC real measurements results. | 95 |
| 6.1 | Crest factor measurements and its relative error for the “leading” CF tests. | 127 |
| 6.2 | Crest factor measurements compensation and its relative error. | 128 |
| 6.3 | Total active energy measurement error. | 129 |
| 6.4 | Total active energy compensated measurement error. | 131 |
| 6.5 | Total apparent energy measurement error. | 132 |
| 6.6 | Total active energy compensated measurement error. | 133 |
| 6.7 | Fundamental active energy measurement error. | 134 |
| 6.8 | Fundamental active energy compensated measurement error. | 136 |
| B.1 | Voltage and current balance. | 152 |
| B.2 | Reference conditions. | 152 |
| C.1 | Definitions of meter quantities for calibration. | 153 |

Glossary of Abbreviations

AA Anti-Aliasing filter.

ADC Analogue to Digital Converter.

AFE Analogue Front-End.

AMI Advanced Metering Infrastructure.

AMR Automatic Meter Reading.

ANSI American National Standards Institute.

AWG Arbitrary Waveform Generator.

CENELEC European Committee for Electrotechnical Standardization.

CF Crest Factor.

CFL Compact Fluorescent Lamp.

CMRR Common Mode Rejection Ratio.

CPU Central Processing Unit.

csv Comma-Separated Values.

CT Current Transformer.

DSP Digital Signal Processing.

DUT Device Under Test.

Glossary of Abbreviations

EEM Electromechanical Electricity Meter.

EN European Standards.

ENOB Effective Number of Bits.

EPRI Electric Power Research Institute.

FIR Finite Impulse Response.

FPGA Field-Programmable Gate Array.

GUI Graphical User Interface.

GUM Guide to the Expression of Uncertainty in Measurement.

HPF High-Pass Filter.

HRC High Rupturing Capacity fuse.

HSDC High Speed Data Capture.

IC Integrated Circuit.

IEC International Electrotechnical Commission.

IEEE Institute of Electrical and Electronics Engineers.

IIR Infinite Impulse Response.

ISO International Organization for Standardization.

LCD Liquid Crystal Display.

LED Light-Emitting Diode.

MID Measuring Instruments Directive.

MPE Maximum Permissible Error.

Glossary of Abbreviations

NPL National Physical Laboratory.

OED Optimal Design of Experiments.

OIML International Organization of Legal Metrology.

PANDA equiPment hArmoNic DAtabase.

PC Personal Computer.

PDS Power Drive System.

PF Power Factor.

PGA Programmable Gain Amplifier.

PMU Phasor Measurement Unit.

rms Root Mean Square.

RPi Raspberry Pi single computer board.

RVD Resistive Voltage Divider.

SAR Successive Approximation Register.

SEM Static Electricity Meter.

SNR Signal to Noise Ratio.

THD Total Harmonic Distortion.

VSL Dutch Metrology Institute.

VSWR Voltage Standing Wave Ratio.

VT Voltage Transformer.

ZX Zero-Crossing.

Chapter 1

Introduction

1.1 Introduction to the Research

An electricity meter is a device designed to measure the amount of electrical energy consumed or produced by an electrical utility’s customer, such as residences and businesses. They were originally electromechanical devices, but they have been replaced by electronic versions provided with communications capabilities and other features to achieve advanced monitoring in modern and future grids. The transition from a traditional electrical grid to the smart grid involves significant changes that create new challenges for electricity meters [1]. In this dynamic scenario where energy could flow in both directions and the expected sinusoidal waveforms are highly distorted (i.e. above the allowed 3% sine wave distortion as prescribed by standards for testing and calibration [2–6]), accuracy becomes a crucial factor for the correct values of electrical power and energy for the purposes of revenue and control. A massive deployment of “smart” static electricity meters (SEM) is currently taking place in many countries around the world, replacing the reliable electro-mechanical electricity meter (EEM) and even previous versions of SEMs. The Asia-Pacific electricity market (China, Japan, South Korea, India, Australia, and New Zealand), for example, is the largest and fastest growing market and it is expected to reach 975 million units of smart SEMs installed by 2024 [7]. Thus, even small and subtle inaccuracies in the calculation of electrical energy consumption (or production) will have a great economical impact in aggregate.

Standards for electricity meters [2–6], currently used for international certification, provide requirements for revenue meters that lack definitions for nonsinusoidal waveforms [8]. These standards apply to electro-mechanical or static meters and cover specific tests and test conditions. Regarding the accuracy, the IEC 62053-21 and IEC 62053-22 standards indicate the limits of error for static energy meters due to variations of the current and other influencing quantities and clearly state how the “normal” test conditions should be performed [4, 5]. For nonsinusoidal situations, for example, standard tests in the presence of harmonics include only the 5th harmonic which does not fully represent modern power grid scenarios.

Experimental-based studies have been conducted in order to analyse the effects of nonsinusoidal waveforms on several electricity meters [9]; nonetheless, most of these studies are focused only on harmonic contents produced by non-linear loads [10–13] or injected to the load through the power grid [14, 15]. Although many authors have proposed procedures and methods to calibrate meters under nonsinusoidal waveforms, the tests and the test conditions differ widely within the literature [16–19]. Even more, there are not proposed methods or procedures to evaluate the response of electricity meters when exposed to waveforms with an impulsive current behaviour, i.e. current signals with high amplitude changes of short duration. This thesis address this gap by proposing a novel set of waveforms to evaluate the accuracy of electricity meters under fast-changing current situations.

Additional efforts (i.e. standard extension, technical reports and recommendations) have been made trying to address the non-ideal scenarios for electricity meters under nonsinusoidal and unbalanced conditions. Some of the most important documents issued in this regard are the electric power quantities for nonsinusoidal and unbalanced situations defined in [20], the recommendations for testing meters under the influence of harmonics prescribed in [21] or the tests for immunity to disturbances and signalling described in [22]. Nevertheless, such recommendations are not mandatory for revenue electricity meters to be approved by regulatory bodies up to this day.

Another relevant issue that electricity meters manufacturers face is the broad flexibility to implement different algorithms to calculate the electrical energy consumed

by a customer, since there is not a unique, formal algorithm to implement in digital metering [23], when nonsinusoidal conditions exist. This flexibility leads to revenue losses for utilities and in some cases, unfair billing for customers, as there is a chance to be overcharged when absorbing harmonics from a neighbouring customer which is “polluting” the grid [24].

For a better understanding of the causes of metering error in SEMs when exposed to nonsinusoidal waveforms, an in-depth analysis of SEM internal components and its response to specific signal characteristics is needed. This thesis examines the response of typical SEM analogue and digital components to both sinusoidal and nonsinusoidal signals.

1.2 Research Motivation

Numerous changes in electrical grid schemes, like the inclusion of renewable energy, the rise of non-linear loads and the emergence of electric vehicle charging, increases variable power quality conditions of the grid. When power quality disturbances like harmonics, inter-harmonics and unbalance exist in the electrical grid, the error of electricity meters could be significant, depending on the design of the meter and the measurement techniques adopted (i.e. transducers, electrical quantities definitions, measurement algorithm) [25]. This non-ideal power quality scenario can produce an error in electricity meters, that is not yet well known since there is no standardised procedure to calibrate meters under typical or emerging nonsinusoidal waveform conditions. Errors in the assessment of electrical power and energy values have significant ramifications for revenue, billing and power system control.

The metrology requirements for the on-going and foreseeable smart grid deployment are moving to require accurate measurements of more electrical quantities calculated by SEMs. This is particularly important when the conditions of the electrical grid are nonsinusoidal and the power factor (PF) is low. Traditional EEM technology of typical 1% - 2% accuracy class is being replaced by SEMs which claim higher accuracy levels from 1% up to 0.2% relative error which holds for sinusoidal situations.

Since the early deployments of SEMs, many concerns and complaints from customers who do not trust smart meter accuracy have appeared [25]. As a result, researchers of many institutions have been testing electricity meters under nonsinusoidal waveform conditions and proposing methods to calibrate such meters in more representative real-world operating conditions. Some of the already installed SEMs have experienced significant deviations with respect to an electromechanical reference meter, in the order of +500% [26], when exposed to certain nonsinusoidal current signals. However, not all the tested SEMs are affected in the same manner by nonsinusoidal signals. Some meters are able to measure electrical quantities of nonsinusoidal signals with a relative error within per class maximum permissible error while others present positive or negative relative errors outside the standard test requirements, i.e. overestimating or underestimating the measured quantity value. All such deployed meters have been tested and certified by regulatory bodies such as the European Measuring Instruments Directive (MID) which could generate worry and distrust among electricity consumers. Applicable accuracy standards and regulations indicate a maximum distortion factor of 3% of the sinusoidal waveform for voltage and current during the calibration, which is not representative of many modern dynamic power quality scenarios, where current distortion of typical electrical appliances could be as high as 96.06% for a compact fluorescent lamp (CFL), 205.19% for a smartphone during battery charge, 72.47% for a desktop computer or 8.41% for a electrical vehicle charging [27].

Therefore, there is a need for developing new methods for systematically testing SEMs under nonsinusoidal conditions, and understanding the key underpinning influences. In order to provide a testbed and a set of test waveforms which assure accurate measurements of nonsinusoidal signals, the following considerations should be taken:

- It is important to identify the characteristics of nonsinusoidal waveforms responsible of triggering significant errors in SEMs. In this regard, key parameters like the signal slope, crest factor (CF), transition duration and phase angle between the voltage and current signals should be carefully evaluated to understand how are influencing meters accuracy and not merely rely on the signal harmonic content.

- The overall accuracy of measured electrical quantities depends on individual error contributions from different stages of the signal path within the measurement instrument, as well as power quality conditions of the grid [28]. Thus, splitting the SEM signal path into its components to evaluate the impact of nonsinusoidal signal individual parameters on meter accuracy is needed. The assessment of the influence of each parameter through the signal path will allow identification accuracy boundaries of SEM components.
- Electric power quantities appropriate to electrical energy measuring instruments under sinusoidal and nonsinusoidal conditions have been defined in the IEEE 1459-2010 standard [20] and should be adopted by SEM designers and regulatory organizations. The algorithms to implement such definitions should be also assessed and if possible, standardized.
- A set of waveforms with characteristics known to cause relative errors on SEMs outside prescribed standard limits, should be included in type-approval tests along with a suitable testbed and reference meter (or source).

1.3 Thesis Aim and Objectives

The aim of this research is to investigate the root causes of total energy measurement error in electricity meters when exposed to nonsinusoidal signals beyond prescribed standard accuracy testing waveforms. The objectives of this thesis are as follows:

1. Developing a set of nonsinusoidal waveforms for testing the accuracy of electricity meters beyond the standards' requirements. Moreover, the proposed nonsinusoidal waveform set should contain waveform parameters which are known to cause errors in the total active energy measurements from static electricity meters.
2. Applying the proposed nonsinusoidal waveform set to a representative energy metering integrated circuit, which is typically responsible for performing the total energy calculations, and is representative of most deployed electricity meters.

3. The results of applying the nonsinusoidal waveform set should be evaluated to identify the root causes of measurement errors and, if possible, to propose a methods for error compensation.

In order to achieve the aim and objectives of this thesis, the research approach involves the following key steps:

1. Identify the waveform parameters that are responsible for errors in the measurement of total active energy in static electricity meters.
2. Develop a testbed for testing an energy metering integrated circuit under sinusoidal and nonsinusoidal conditions.
3. Develop a set of nonsinusoidal waveforms for evaluating the accuracy of the energy metering integrated circuit's total active energy calculations.
4. Model the energy metering integrated circuit to evaluate its theoretical response to sinusoidal and diverse nonsinusoidal waveforms.
5. Apply the proposed nonsinusoidal waveform set to the energy metering integrated circuit and compared the obtained measurements to the model calculations.
6. Analyze the measurement results and investigate a method for error compensation.

1.4 Principal Contributions

This thesis provides the following contributions to knowledge:

- Identification and analysis of the key parameters in nonsinusoidal waveforms which are responsible for causing errors in SEMs.
- Design of an implementation of an electrical metering integrated circuit (IC) model to simulate its response to nonsinusoidal waveforms. Components in the

model and its parameters can be manipulated to improve simulated measurements' accuracy, leading to improved IC performance under nonsinusoidal situations.

- For the first time, an SEM, traditionally seen as a black-box, has been examined in this work from the internal view, shedding some light on the mechanisms that produce errors in electricity meters.
- Design, application and analysis of a novel methodology to evaluate the response of metering IC technology to impulsive (i.e. fast-changing) currents. The methodology includes a proposed set of synthesized waveforms intended to reveal and provide understanding of the metering limitations through the signal path.
- A new method for the compensation of errors introduced by fast-changing nonsinusoidal waveforms, thereby providing a complete and improved future-proof system for all electricity metering applications.

1.5 Thesis Overview

Chapter 2 reviews the fundamentals of how accuracy of electricity meters is calculated. Relevant standard requirements are presented along with recommendations prescribed by regulatory bodies. Meter quantities such as nominal, minimum and maximum currents are defined. The maximum error allowed per metering class and the standard accuracy tests are described. The definition of suitable electrical quantities for electrical measurements under sinusoidal and nonsinusoidal conditions are provided.

Chapter 3 presents a detailed description of SEM components, from the analogue front-end (AFE) to the digital signal processing. The chapter also introduces typical energy metering integrated circuit technology including analysis and description of its components.

Later, Chapter 3 provides examples of electricity meter erroneous measurements reported in the literature and reviews existing attempts to address this problem. The metering errors are organized in four sections categorizing tests according to its pur-

Chapter 1. Introduction

pose or methodology implemented. This provides clarity of the existing literature and research.

In Chapter 4, an experimental setup and a set of test signals to evaluate the accuracy of a representative energy metering IC, beyond the limits established by prior work, is described. The selection of signals includes sinusoidal and standard nonsinusoidal situations, as well as nonsinusoidal real-world captured current waveforms and signals specifically designed to mimic the behaviour of impulsive currents typically produced by power electronic devices. The results of performed tests are reported and analysed in chapter 5.

A novel procedure to compensate measurement errors produced by current signals with high crest factor value is proposed in Chapter 6 as a practical solution for deployed electricity meters exposed to fast-changing current conditions.

Chapter 7 summarizes the conclusions and novel contributions of this thesis and suggests future work on this topic which has been identified through the research.

1.6 Associated Publications

The following publications have been completed during the course of this PhD:

Published

Y. Seferi, R. G. Q. Cetina and S. M. Blair, “*Review of PMU Algorithms Suitable for Real-Time Operation With Digital Sampled Value Data*”, 2021 IEEE 11th International Workshop on Applied Measurements for Power Systems (AMPS), 2021, pp. 1-6, doi: 10.1109/AMPS50177.2021.9586034. <https://strathprints.strath.ac.uk/78316/>

R. Quijano Cetina, Y. Seferi, S. M. Blair and P. S. Wright, “*Energy Metering Integrated Circuit Behaviour Beyond Standards Requirements*”, MDPI journal of Energies, Special Issue “Measurements, Sensors and Instrumentation for Electrical Power Systems”. <https://www.mdpi.com/1996-1073/14/2/390>

R. Quijano Cetina, Y. Seferi, S. M. Blair and P. S. Wright, “*Analysis and selection of appropriate components for power system metrology instruments*”, 2019 2nd International Colloquium on Smart Grid Metrology (SMAGRIMET), Split, Croatia, 2019, pp. 1-6, doi: 10.23919/SMAGRIMET.2019.8720362. <https://strathprints.strath.ac.uk/67315/>

R. Quijano Cetina, A. J. Roscoe and A. C. Atoche, “*Low-cost power systems metrology laboratory based on raspberry Pi*”, 2018 First International Colloquium on Smart Grid Metrology (SmaGriMet), Split, 2018, pp. 1-2, doi: 10.23919/SMAGRIMET.2018.8369843. <https://strathprints.strath.ac.uk/63582/>

Quijano Cetina, R. A. J. Roscoe and P. S. Wright, “*Challenges for Smart Electricity Meters due to Dynamic Power Quality Conditions of the Grid: A Review*”, 2017 IEEE International Workshop on Applied Measurements for Power Systems (AMPS), Liverpool, 2017, pp. 1-6, doi: 10.1109/AMPS.2017.8078345. <https://strathprints.strath.ac.uk/61521/>

R. Quijano Cetina, A. J. Roscoe and P. S. Wright, “*A review of electrical metering accuracy standards in the context of dynamic power quality conditions of the grid*”, 2017 52nd International Universities Power Engineering Conference (UPEC), Heraklion, 2017, pp. 1-5, doi: 10.1109/UPEC.2017.8231871. <https://strathprints.strath.ac.uk/61571/>

Chapter 2

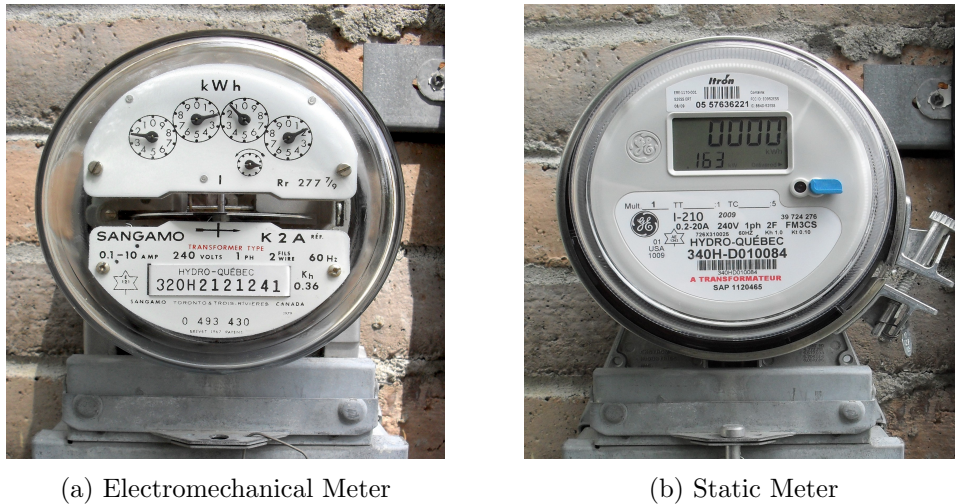
Review of Standard Requirements and Electric Power Definitions for Static Electricity Meters

2.1 Introduction

A static electricity meter is an electronic measuring device designed to quantify the amount of electrical energy flowing through a particular point of an electrical system, by means of sampling the voltage and current signals. It is widely used by electrical suppliers for billing each customer's electrical consumption and more recently to measure the electrical production and consumption of new type of customer named prosumers (producer and consumer client).

Static electricity meters have been replacing electromechanical electricity meters since the 1980s (Figure 2.1), and becoming the norm in the 1990s [29]. One of the main reasons which drove this transition is the higher level of accuracy that this type of meters can achieve and maintain over time due to the lack of rotating elements prone to wear and tear.

Chapter 2. Review of Standard Requirements and Electric Power Definitions for Static Electricity Meters



(a) Electromechanical Meter

(b) Static Meter

Figure 2.1: Typical electromechanical electricity meter (a) has been replaced by static electricity meter (b) [30].

Electronic meters have been also provided with communication capabilities, making it possible to establish Automatic Metering Reading (AMR). When the meter is able to perform two-way communication with the utility or supplier, and has been provided with additional features such as higher time resolution for measurements [31], the industry refers to such devices as smart electricity meters, or smart meters. Smart meters are a fundamental component of the Advanced Metering Infrastructure (AMI) along with the equipment needed to collect and process data to be delivered to the grid operator.

Despite the aforementioned advantages, static meters, under certain circumstances, can exhibit accuracy errors beyond the limits established by relevant standards. In this chapter, section 2.2 reviews the power quantity definitions that electrical measurement instruments should apply, section 2.3 presents a review of the error allowed by the standards, and the formulas used to estimate this error are given in section 2.4.

2.2 Electric Power Quantities Definitions

Applicable standards for static electricity meters (i.e. IEC 62053, EN 50470 and OIML R 46, later reviewed in section 2.3) only cover accuracy requirements for measured

active energy and very few definitions for electric power quantities are provided, i.e. total active power, total power factor and total apparent power. Furthermore, those definitions are valid only for sinusoidal waveforms and, in the case of three-phase systems, balanced conditions. Fundamental quantities such as fundamental active power, fundamental power factor and fundamental apparent power are not included.

For nonsinusoidal (and unbalanced) situations, the IEEE 1459:2010 standard [20] provides definitions for electric power quantities suitable for revenue purposes. A set of new definitions are listed in this standard, to overcome the problem of previous definitions should only be applied for nearly sinusoidal voltage and current waveforms. To date, the definitions prescribed by IEEE 1459 are not mandatory to be implemented by static meters in order to obtain MID approval, however, it has been demonstrated that implementation of different definitions lead to different results when nonsinusoidal situations occurs [23].

In this section, the most relevant definitions for electrical revenue metering are presented, organized in definitions suitable for sinusoidal and nonsinusoidal conditions, for single-phase systems. Despite the IEEE 1459:2010 standard presenting all valid formulas for calculating electrical quantities, in this document only preferred (recommended) formulas are presented.

2.2.1 Single-Phase: sinusoidal

Instantaneous voltage v and instantaneous current i

A perfect voltage signal applied to a linear load by a power source produces sine waveforms for the current and instantaneous power signals as can be seen in Figure 2.2. Instantaneous voltage v and instantaneous current i values from sinusoidal waveforms (Figure 2.2 (a)) are described as follows:

$$v = \sqrt{2}V \sin(\omega t) \tag{2.1}$$

$$i = \sqrt{2}I \sin(\omega t - \theta) \tag{2.2}$$

Chapter 2. Review of Standard Requirements and Electric Power Definitions for Static Electricity Meters

where:

V is the rms value of the voltage (V)

I is the rms value of the current (A)

ω is the angular frequency $2\pi f$ (rad/s)

f is the power system frequency (Hz)

θ is the phase angle of the current with respect to the voltage (rad)

t is the time (s)

Total Active Power P

Also called real power, total active power is the mean (averaged) value of the instantaneous power p (Figure 2.2 (b))

$$P = \frac{1}{kT} \int_{\tau}^{\tau+kT} p dt = VI \cos\theta \quad (2.3)$$

where:

$T = 1/f$ is the cycle time (s)

k is a positive integer number

τ is the moment when the measurement starts

$p = vi$ is the product of instantaneous voltage and instantaneous current values

V is the rms value of the voltage (V)

I is the rms value of the current (A)

θ is the phase angle of the current with respect to the voltage (rad)

Reactive Power Q

This quantity represents the amplitude of instantaneous power oscillations between a nonlinear load and the power source. Reactive power Q “quantifies the rate of flow of the energy exchanged among load and source and even among different loads” [32]. Its expression is:

$$Q = VI \sin\theta \quad (2.4)$$

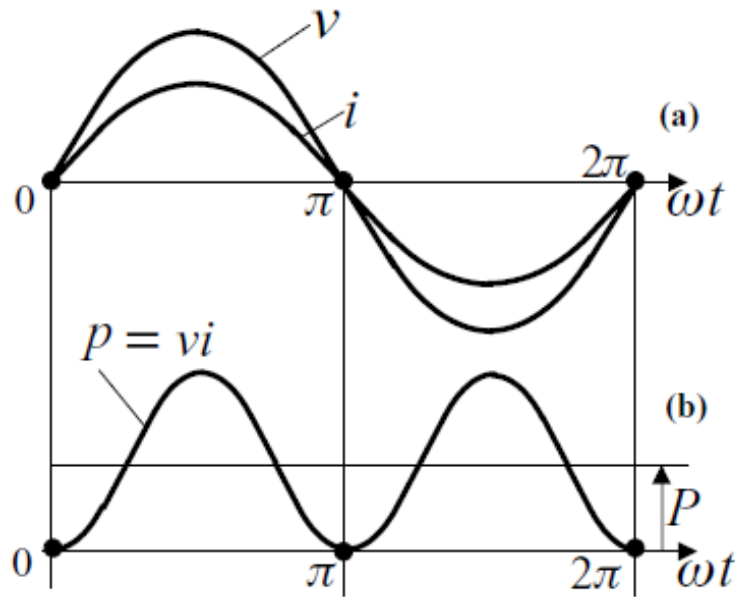


Figure 2.2: Sinusoidal waveform of: (a) instantaneous voltage v and instantaneous current i ; (b) instantaneous active power p . Figure taken from [32].

IEEE 1459 standard categorizes reactive power Q as a nonactive power because the aforementioned exchange of energy does not contribute to a net transfer of energy between the load and the source. Additionally, reactive power Q is responsible for power losses in conductors that supply the load.

Apparent Power S

Apparent power S is a electrical quantity whose definition is still a matter of discussion among the scientific community [32–35] with two main schools of thought (i.e. theoretical approach and practical approach) prevailing at this time [36]. It is a very useful quantity which helps to estimate the size, losses, aging and life-span of electrical equipment [32]. The most commonly adopted definition of apparent power (the practical approach definition) is the product of voltage V and current I rms values as follows:

$$S = VI \tag{2.5}$$

This apparent power definition leads to the well-known power triangle which holds only for sinusoidal waveforms. The traditional power triangle, an updated power rep-

Chapter 2. Review of Standard Requirements and Electric Power Definitions for Static Electricity Meters

resentation for nonsinusoidal cases and the newly IEEE 1459 total apparent power S decomposition are provided in Appendix A.

Power Factor PF

Power factor is defined as the ratio of the total active power P to the apparent power S

$$PF = \frac{P}{S} \quad (2.6)$$

PF is a figure which helps to evaluate the utilization of a transmission line (or a feeder), due to conductor losses included in apparent power S .

Active Energy E

Usually expressed in kWh units, active energy E is the most important quantity measured by utilities for revenue purposes. Active energy is simply the instantaneous power p integrated over a period of time T

$$E(T) = \int_0^T p(t)dt = \int_0^T v(t)i(t)dt \quad (2.7)$$

2.2.2 Single-Phase: nonsinusoidal

A non-linear load will draw a nonsinusoidal current waveform, even when a sinusoidal voltage signal is applied to its terminals. Furthermore, due to the non-zero value of a real power grid impedance, the voltage will be also nonsinusoidal due to the non-linear load (Figure 2.3(a)). The resulting instantaneous active power signal p will also be nonsinusoidal (Figure 2.3(b)).

A nonsinusoidal periodical waveform of current or voltage is composed by two elements: fundamental frequency components v_1 and i_1 and non-fundamental frequency components v_H and i_H

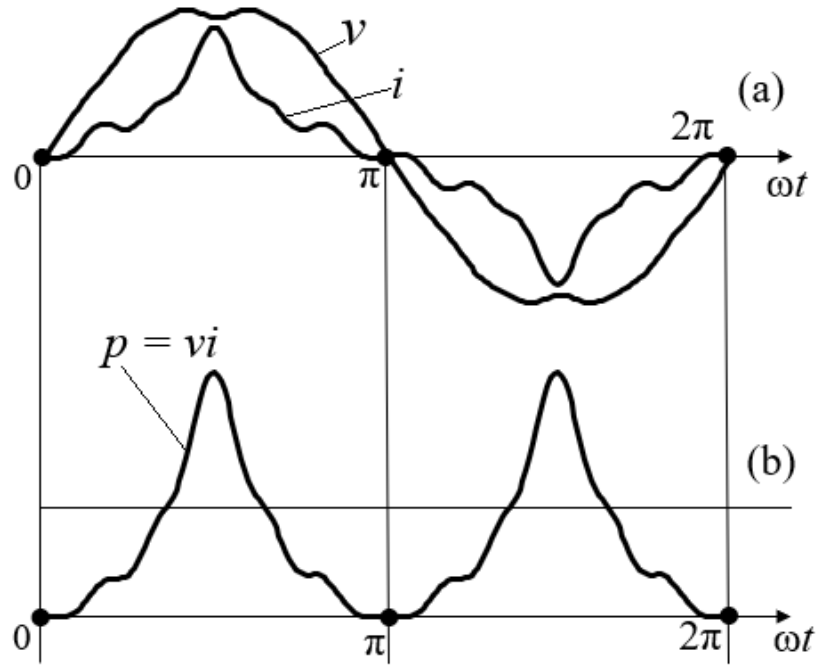


Figure 2.3: Nonsinusoidal waveform of “Peaked” signal: (a) instantaneous voltage v and instantaneous current i ; (b) instantaneous total active power p .

$$v = v_1 + v_H \quad (2.8)$$

and

$$i = i_1 + i_H \quad (2.9)$$

where

$$v_1 = \sqrt{2}V_1 \sin(\omega t - \alpha_1)$$

$$i_1 = \sqrt{2}I_1 \sin(\omega t - \beta_1)$$

$$v_H = V_0 + \sqrt{2} \sum_{h \neq 1} V_h \sin(h\omega t - \alpha_h)$$

h = harmonic order

$$i_H = I_0 + \sqrt{2} \sum_{h \neq 1} I_h \sin(h\omega t - \beta_h)$$

$$V_H^2 = V_0^2 + \sum_{h \neq 1} V_h^2 = V^2 - V_1^2$$

$$I_H^2 = I_0^2 + \sum_{h \neq 1} I_h^2 = I^2 - I_1^2$$

A pure sine waveform such as the voltage depicted in Figure 2.2 (a), for example, will only include fundamental frequency components, i.e. $v = v_1$ and because there are no harmonic components $v_H = 0$. The nonsinusoidal signal of instantaneous current i of “peaked” waveform in Figure 2.3 (a), on the other hand, is composed of fundamental current i_1 and harmonic currents i_3, i_5, i_7, i_{11} and i_{13} (see Table 2.7 and Figure 2.4).

Thus, equations 2.8 and 2.9 are appropriate to be used to estimate instantaneous voltage and current values of periodical signals regardless of its waveform.

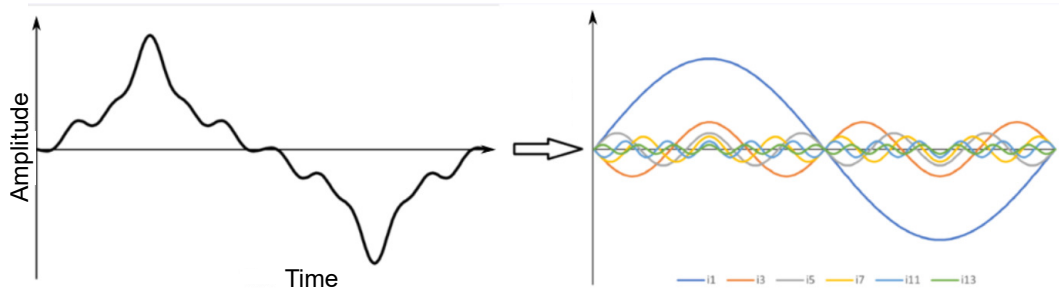


Figure 2.4: Peaked waveform and its harmonic current components.

Total active power includes both fundamental and harmonic active power components as follows:

$$P = P_1 + P_H \quad (2.10)$$

where fundamental active power P_1 is defined by

$$P_1 = \frac{1}{kT} \int_{\tau}^{\tau+kT} v_1 i_1 dt = V_1 I_1 \cos \theta_1 \quad (2.11)$$

θ_1 , also called fundamental phase angle, is the phase angle between the fundamental voltage and the fundamental current signals.

The harmonic active power P_H is defined by

$$P_H = V_0 I_0 + \sum_{h \neq 1} V_h I_h \cos \theta_h = P - P_1 \quad (2.12)$$

where θ_h , also called harmonic phase angle, is the phase angle between the harmonic voltage and the harmonic current signals, taking the voltage as the reference.

Although electricity meters measure the total active power P for billing purposes, it is worth noting that fundamental active power P_1 is the only product being traded by electrical utilities, as the nominal frequency prescribed by the standard EN 50160-2010+A3 [37] for low, medium and high voltage networks is 50 Hz. There is no active power at frequencies different from the fundamental being sold or purchased by either customer or the utility [35]. Furthermore, harmonic active power P_H is an undesirable consequence of a combination of factors such as the interaction of customers' non-linear loads, grid impedance and the harmonic power imported from a neighbouring customer. It has been demonstrated [35] that by measuring the total active power P , a customer generating harmonic power P_H (i.e. injecting harmonic power to the grid) earns a discount in the electricity bill, whereas a customer absorbing harmonic power gets a penalty as per formula 2.10. Thus, separation of total active power P into its components allows fairer ways to bill customers according to the utilized electrical active power at all frequencies. Moreover, it is possible to allocate responsibilities to grid-polluting customers by means of implementing IEEE 1459 definitions such as total harmonic distortion or voltage and current distortion powers (defined below) in order to recover costs caused by harmonics on the grid.

Total Harmonic Distortion (THD)

Total harmonic distortion is defined as the overall deviation of a distorted signal from its fundamental form. This value is used by standards to indicate allowed level of distortion of a sine waveform for accuracy tests.

$$THD_V = \frac{V_H}{V_1} = \sqrt{\left(\frac{V}{V_1}\right)^2 - 1} \quad (2.13)$$

$$THD_I = \frac{I_H}{I_1} = \sqrt{\left(\frac{I}{I_1}\right)^2 - 1} \quad (2.14)$$

Harmonic Power Factor (HPF)

The harmonic power factor PF_{THD} is defined as the ratio of the total active power to apparent power due to distortion caused by harmonic content. The harmonic power factor, also known as distortion power factor, is calculated as follows:

$$PF_{THD} = \sqrt{\frac{1}{1 + (THD)^2}} \quad (2.15)$$

Voltage and Current Distortion Powers D_V and D_I

The IEEE 1459 standard has defined distortion power quantities for voltage and current signals, which provide useful insights regarding the nature and possible source of distortion in power systems.

$$D_V = V_H \times I_1 \quad (2.16)$$

$$D_I = V_1 \times I_H \quad (2.17)$$

In power systems, current distortion is mainly caused by customers' nonlinear loads, generating current at harmonic frequencies, whereas voltage distortion is mostly due to the utility's non-zero source impedance, producing voltages at harmonic frequencies [34]. Thus, both voltage and current distortion power quantities may be useful for

revenue metering.

Fundamental Reactive Power Q_1

The fundamental reactive power Q_1 represents energy oscillations between load and source (or among loads) only at fundamental frequency (e.g. 50Hz or 60Hz).

$$Q_1 = V_1 I_1 \sin\theta_1 \quad (2.18)$$

Fundamental Apparent Power S_1

The product of fundamental voltage and current rms values is known as fundamental apparent power:

$$S_1 = V_1 I_1 \quad (2.19)$$

$$S_1^2 = P_1^2 + Q_1^2 \quad (2.20)$$

For sinusoidal waveforms, $S = S_1$, whereas for nonsinusoidal signals, S is usually larger than S_1 .

Fundamental Power Factor PF_1

Similar to the total power factor PF , fundamental power factor PF_1 helps to evaluate individually the fundamental power flow conditions:

$$PF_1 = \cos\theta_1 = \frac{P_1}{S_1} \quad (2.21)$$

Nonfundamental Apparent Power S_N

Under nonsinusoidal conditions, total apparent power S is composed by fundamental apparent power S_1 and nonfundamental apparent power S_N as follows:

$$S_N = \sqrt{S^2 - S_1^2} \quad (2.22)$$

Chapter 2. Review of Standard Requirements and Electric Power Definitions for Static Electricity Meters

Because nonfundamental components are responsible for distortion in the current and voltage signals, nonfundamental apparent power S_N could also be expressed in terms of voltage and current distortion powers, and the harmonic apparent power S_H :

$$S_N^2 = D_1^2 + D_V^2 + S_H^2 \quad (2.23)$$

where harmonic apparent power S_H is the product of harmonic voltage V_H and harmonic current I_H rms values:

$$S_H = V_H I_H = S_1 (THD_I) (THD_V) \quad (2.24)$$

Harmonic apparent power S_H could be also expressed in terms of active harmonic power P_H and harmonic distortion power D_H :

$$S_H = \sqrt{P_H^2 + D_H^2} \quad (2.25)$$

where

$$D_H = \sqrt{S_H^2 - P_H^2} \quad (2.26)$$

Nonactive Power N

Nonactive power N combine both fundamental and nonfundamental nonactive components:

$$N = \sqrt{S^2 - P^2} \quad (2.27)$$

This power was previously called “fictitious power” and shall not be confused with a reactive power [20].

2.2.3 Supplementary Quantities

Peak Current i_{peak}

Maximum absolute value of a current signal with respect to the reference current.

Crest Factor CF

Ratio of the peak value to the rms value of a signal. As voltage signals in real power grids do not present crest factor values that are significantly high (i.e. above typical 1.41 crest factor value), in this thesis, only the current CF is revised.

$$CF = \frac{|i_{peak}|}{I} \quad (2.28)$$

where I is the rms value of the current (A)

2.3 Standards and Regulations for Electricity Meters

As early as 1910, the first standard for electricity metering was issued, the ANSI C12 Code, which has the following written in its Preface: *“While the Code is naturally based upon scientific and technical principles, the commercial side of the metering has been constantly kept in mind as of very great importance”* [38]. This sentences makes a significant statement about the need of keep trade in mind, because electricity is a service which can be sold and purchased. Thus, legal metrology requirements were defined.

Later, in 1931, the International Electrotechnical Commission issued the standard IEC 43 and established accuracy class 2.0 (i.e. meters of allowed 2% relative error) for electricity meters, which still remains as an acceptable accuracy class for domestic electrical metering.

From a utility’s point of view, accuracy, durability and dependability are the most important qualities an electricity meter should satisfy, whereas for customers, accuracy is probably the most important feature as there is a chance to be over-charged for their electricity usage, if the meter is not accurate enough [29].

From this perspective, regulatory bodies make efforts to try to keep electrical metering accuracy at the higher possible levels, updating periodically the standards to meet expectations and needs from an electrical grid that is constantly evolving.

In the following subsections, the most recently versions of the key standards and

related international recommendations are summarised.

2.3.1 North American Standards

2.3.1.1 ANSI C12 Series

ANSI C12 series is the American national standard intended for electricity meter certification. In this code, requirements for a.c. Watt-hour meters have been defined, as well as accuracy tests and the acceptable performance criteria. The most recent editions of such codes are the ANSI C12.1-2014 [39], which specifies requirements and tests for both electromechanical and electronic meters, and ANSI C12.20-2015 [40] which “sets the physical aspects and acceptable criteria for 0.1, 0.2 and 0.5 accuracy class electricity meters” [41].

2.3.2 International Standards

2.3.2.1 IEC Standards

The International Electrotechnical Commission (IEC), an international standards organization, has also published standards for electricity metering equipment, similar to those published by ANSI. The standards are organized in various documents, covering accuracy tests and defining accuracy classes. These standards are widely used outside the United States of America, as an alternative to ANSI standards. Some of the most relevant standards among the IEC for a.c. electrical measuring equipment are:

- **IEC 62052-11:2021** Electricity metering equipment (a.c.) - General requirements, tests and test conditions - Part 11: Metering equipment
- **IEC 62053-11:2003+A1:2017** Electricity metering equipment (a.c.) - Particular requirements - Part 11: Electromechanical meters for active energy (classes 0.5, 1 and 2)
- **IEC 62053-21:2021+A11:2021** Electricity metering equipment (a.c.) - Particular requirements - Part 21: Static meters for active energy (classes 1 and 2)

- **IEC 62053-22:2021** Electricity metering equipment (a.c.) - Particular requirements - Part 22: Static meters for active energy (classes 0.2S and 0.5S)
- **IEC 62053-23:2021+A11:2021** Electricity metering equipment (a.c.) - Particular requirements - Part 23: Static meters for reactive energy (classes 2 and 3)
- **IEC 62053-24:2021+A11:2021** Electricity metering equipment (a.c.) - Particular requirements - Part 24: Static meters for reactive energy at fundamental frequency (classes 0.5S, 1S and 1)

As per the purposes of this thesis, only static meters are revised with a particular focus on the accuracy allowance for electrical active energy measurements. The percentage error limits for the total active energy measurements prescribed by IEC standards for static electricity meters [4, 5] are shown in table 2.1 as a function of the current value and power factor. These limits are valid for the rated operating conditions shown in appendix B. Additional percentage error due to variation of influence quantities, such as temperature or harmonic content, is allowed by the IEC and could be consulted in the aforementioned IEC 62053-21/22 standards.

Table 2.1: Percentage error limits for the accuracy classes 2, 1, 0.5S and 0.2S (IEC 62053-21/22:2021).

| Value of current | Power factor | Accuracy class | | | |
|--------------------------------|----------------|----------------|------|------|------|
| | | 2 | 1 | 0.5S | 0.2S |
| $I_{min} \leq I < 0.1I_n$ | 1 | ±2.5 | ±1.5 | ±1.0 | ±0.4 |
| $0.1I_n \leq I \leq I_{max}$ | 1 | ±2.0 | ±1.0 | ±0.5 | ±0.2 |
| $0.1I_n^{(1)} \leq I < 0.2I_n$ | 0.5 inductive | ±2.5 | ±1.5 | ±1.0 | ±0.5 |
| | 0.8 capacitive | – | ±1.5 | ±1.0 | ±0.5 |
| $0.2I_n \leq I \leq I_{max}$ | 0.5 inductive | ±2.0 | ±1.0 | ±0.6 | ±0.3 |
| | 0.8 capacitive | – | ±1.0 | ±0.6 | ±0.3 |

Note⁽¹⁾: $0.02I_n \leq I < 0.2I_n$ for accuracy classes 0.5S and 0.2S

IEC 62052-11:2021 [3] defines meter quantities for current as follows:

- **starting current** (I_{st}) for AC meters, the value of current at which the meter is required to start and continue to register active electrical energy at $\cos(\Theta)$

Chapter 2. Review of Standard Requirements and Electric Power Definitions for Static Electricity Meters

= 1 (and in case of polyphase meters, with balanced load) or reactive electrical energy at $\sin(\Theta) = 1$ (inductive or capacitive, and in case of polyphase meters, with balanced load)

NOTE: The term “current” indicates RMS values unless otherwise specified.

- **rated current** (I_n) current in accordance with which the relevant performance of the meter is fixed
- **maximum current** (I_{max}) highest current the meter can carry continuously and remain safe, and at which it purports to meet the accuracy requirements of the relevant standard
- **minimum current** (I_{min}) lowest current at which the meter accuracy requirements are specified

The nomenclature among standards is often slightly different. To avoid confusion, the “value of current” row in Table 2.1 has been harmonized for an easy comparison between MID standards and OIML R 46 recommendation (MID standards and R 46 recommendation are introduced below).

2.3.2.2 MID Standards

The European Measuring Instruments Directive is a directive of the European Parliament, implemented in October 2006 [42] to harmonise many aspects of legal metrology, including the requirements for static electricity meters for active energy. The European Committee for Electrotechnical Standardization (CENELEC) approved in May 2016 the EN 50470-1/3 [43,44] standards for “newly manufactured watt-hour meters, measuring active electrical energy, intended for residential, commercial and light industrial use, for use on 50 Hz electrical networks”. All electricity meters should have MID approval in order to be used in any EU member state.

The standard EN 50470-1 is related to IEC 62052-11, but some modifications have been provided for compliance with the MID requirements. Similarly, EN 50470-3 is related to the IEC 62053-21 and IEC 62053-22 standards.

Chapter 2. Review of Standard Requirements and Electric Power Definitions for Static Electricity Meters

In Table 2.2, the percentage error limits for the total active energy measurements at reference conditions prescribed in EN 50470-3 are shown. It is noticeable that EN 50470-3 defines accuracy classes designated by an uppercase letter which correspond to an equivalent IEC class. Thus, classes 2 and 1 defined in IEC corresponds to classes A and B in EN, respectively. Class 0.5S on IEC is very similar to class C, however, the percentage error limits differ slightly when power factor is not equal to 1. Class 0.2S defined in IEC standard does not have any related class defined by MID.

Table 2.2: Percentage error limits for the accuracy classes A, B and C (EN 50470-1:2006+A1:2018).

| Value of current | Power factor | Accuracy class | | |
|------------------------------|-----------------------|----------------|------|------|
| | | A | B | C |
| $I_{min} \leq I < I_{tr}$ | 1 | ±2.5 | ±1.5 | ±1.0 |
| $I_{tr} \leq I \leq I_{max}$ | 0.5 ind...1...cap 0.8 | ±2.0 | ±1.0 | ±0.5 |

EN 50470-1 standard defines meter quantities for current similarly to IEC 62052-11, introducing the terms I , I_{tr} and I_{ref} as follows:

- **current** (I) the electrical current flowing through the meter
- **minimum current** (I_{min}) the lowest value of the current at which this European Standard specifies requirements. At and above (I_{min}), up to (I_{tr}) relaxed accuracy requirements apply
- **transitional current** (I_{tr}) the value of the current at, and above which, up to (I_{max}) full accuracy requirements of this European Standard apply
- **reference current** (I_{ref})

– for direct connected meters, 10 times the transitional current

NOTE 1 This value is the same as basic current, (I_b) defined in IEC 62052-11

– for current transformer operated meters, 20 times the transitional current

NOTE 2 This value is the same as rated current, (I_n) defined in IEC 62052-11

- **rated current** (I_n) in case of a transformer operated meter, the value of the current for which the meter has been designed

NOTE In case of transformer operated meters, the terms “reference current” and “rated current” are synonymous

2.3.2.3 Accuracy Tests

Both IEC and EN standards define tests for the compliance with accuracy percentage error shown in Tables 2.1 and 2.2 at reference conditions which can be consulted in B. In Table 2.3 the allowed waveform distortion factor (i.e. the THD) to estimate the intrinsic error at reference conditions for meters of different classes is shown. While the accuracy tests tolerate a small percentage of distortion of sine waveforms, the current and voltage signals in modern real-world power grid situations are often distorted significantly higher than tolerated reference conditions [45, 46]. In this regard, accuracy tests in the presence of harmonics are designed to evaluate the response of meters by including higher waveform distortion in type approval tests.

Table 2.3: Waveform THD at reference conditions.

| Influence quantity | Reference value | Distortion factor (THD) less than: | | | |
|--------------------|----------------------------------|------------------------------------|------|---------|------|
| | | 2(A) | 1(B) | 0.5S(C) | 0.2S |
| Waveform | Sinusoidal voltages and currents | 3% | 2% | 2% | 2% |

The same standards also allow an additional percentage error due to the change of influence quantities such as harmonic content, temperature, humidity, etc. For non-sinusoidal situations (i.e. harmonic contents on the voltage and current signals), the allowed additional percentage error for total active energy measurements is shown in Table 2.4.

Accuracy test in the presence of harmonics

For the accuracy test in the presence of harmonics superposed to a voltage and current signals of fundamental frequency equal to 50 Hz, the test conditions are:

- fundamental frequency current: $I_1 = 0.5I_{max}$
- fundamental frequency voltage: $U_1 = U_n$
- fundamental frequency power factor: 1
- content of 5th harmonic voltage: $U_5 = 10\%$ of U_n

Table 2.4: Limits of error due to variation of influence quantities.

| Disturbance | Value of current | | Power factor | Limits of variation in % error | | | |
|--|----------------------------|----------------------|--------------|--------------------------------|------|---------|------|
| | Direct connected | Transformer operated | | 2(A) | 1(B) | 0.5S(C) | 0.2S |
| Harmonics components in the current and voltage circuits | $0.5I_{max}$ | $0.5I_{max}$ | 1 | 1.0 | 0.8 | 0.5 | 0.4 |
| d.c. and even harmonics in the a.c. current circuit | $\frac{I_{max}}{\sqrt{2}}$ | — | 1 | 6.0 | 3.0 | — (1.5) | — |
| Odd harmonics in the a.c. current circuit | $0.5I_b$ | $0.5I_n$ | 1 | 6.0 | 3.0 | — (1.5) | — |
| Sub-harmonics in the a.c. current circuit | $0.5I_b$ | $0.5I_n$ | 1 | 6.0 | 3.0 | (1.5) | 0.6 |

Chapter 2. Review of Standard Requirements and Electric Power Definitions for Static Electricity Meters

- content of 5th harmonic current: $I_5 = 40\%$ of fundamental current
- harmonic power factor: 1
- fundamental and harmonic voltages are in phase, at zero crossing

The resulting waveform is shown in Figure 2.5.

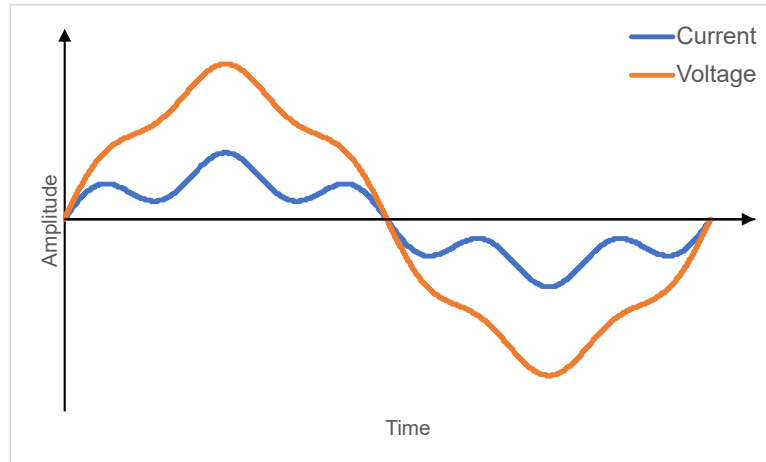


Figure 2.5: Harmonics test waveform.

From the aforementioned harmonic content, it can be observed that the maximum additional percentage waveform distortion allowed in type approval test is 10% and 40% for the voltage and current signals, respectively. While this percentage is typically acceptable for voltage signals [47], current distortion is often much more higher than 40%. It has been reported in the recent literature, results from measurements taken in real-world low-voltage power systems which present current distortion of typical appliances as follows: 78 - 120% for televisions, 25 - 200% for electronic converters and 113% for computers [45, 46].

The issue of high levels of harmonic distortion are expected to increase due to high penetration of renewable energy sources and the rise of saving energy devices, electric charging vehicles and other non-linear loads [48], which can produce fast-changing (pulsed) current signals. Therefore, this thesis aims to demonstrate the importance of updating requirements of standard accuracy tests, to accommodate a higher percentage of distortion for current signals at reference conditions.

Chapter 2. Review of Standard Requirements and Electric Power Definitions for Static Electricity Meters

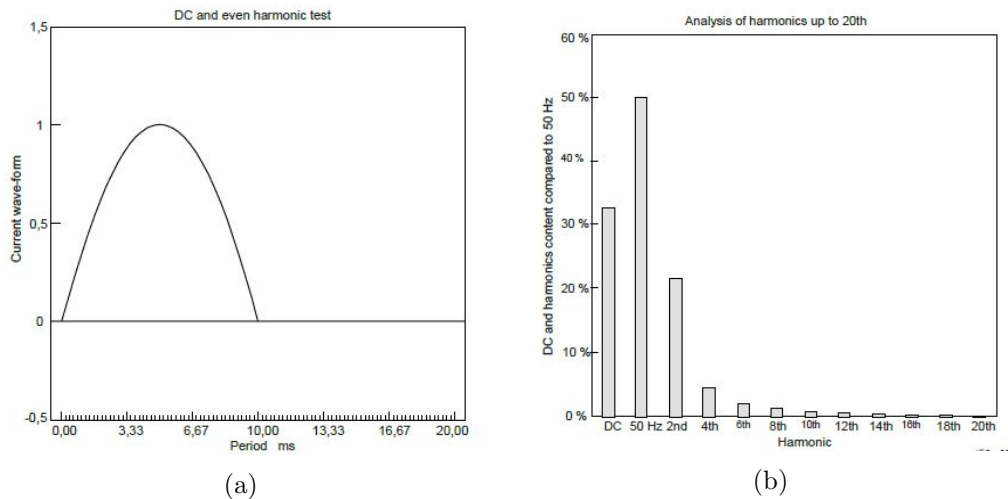


Figure 2.6: d.c. and even harmonics test signal: (a) waveform, (b) Fourier analysis. Figures taken from [44].

Tests of the influence of d.c. and even harmonics

The test for d.c. and even harmonics in a.c. circuit is only applicable to direct connected meters. In Figure 2.6 the half-wave rectified waveform (Figure 2.6a) used for this test is depicted. This kind of waveforms is typically produced by rectified power supplies and other electrical devices using diodes. The Fourier analysis for the half-wave up to the 20th harmonic, can be observed in Figure 2.6b.

Tests of the influence of odd harmonics

The test for the influence of odd harmonics in the error of electricity meters uses a phase fired waveform (Figure 2.7), representing electrical loads with a 90° phase-fired angle control.

Tests of the influence of sub-harmonics

For the sub-harmonic accuracy compliance test, a burst-fired waveform is prescribed. This waveform (burst fired) should be two cycles on and two cycles off, as can be seen in Figure 2.8. The sub-harmonic test is intended to ensure that electricity meters can accurately measure electrical energy of devices employing switching-load control tech-

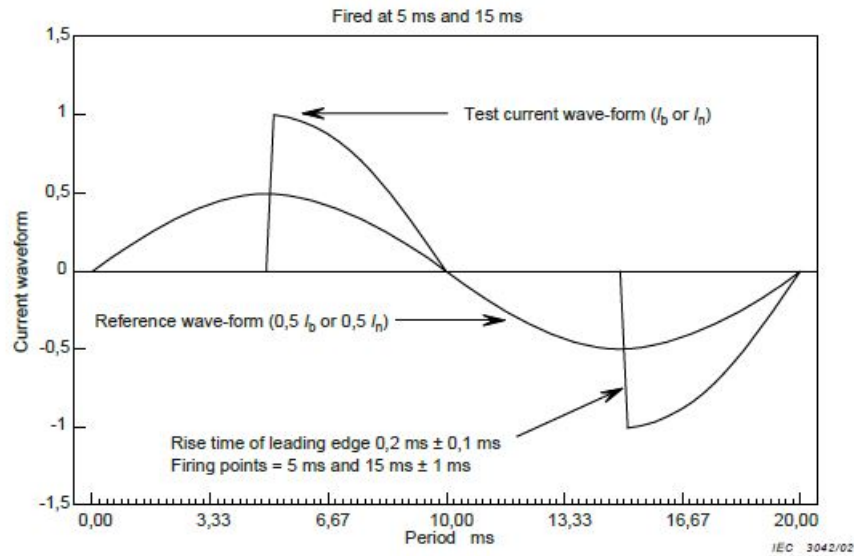


Figure 2.7: Phase fired waveform. Figure taken from [44].

niques (e.g. relay contact bounce, switched inductive loads) which produces transients characterized by a number of cycles on followed by a number of cycles off [49,50]. It is important to note that the prescribed burst-fired waveform has been recently criticized, as there is no real sub-harmonic content and it only appears to be sub-harmonics when a four cycle FFT is (incorrectly) applied [49]. Nevertheless, the test is useful to evaluate the ability of meters to cope with fast switching loads.

2.3.3 Supporting Standards/Documents

Extending the scope of the aforementioned standards with the aim to meet real operational conditions of modern power systems, the International Organization of Legal Metrology has issued complementary documents (denominated International Recommendations) which will be described in this section.

2.3.3.1 OIML R 46

OIML R 46 [21] is an International Recommendation issued in 2012. This document extend the test requirements for electricity meters under sinusoidal, nonsinusoidal, balanced and unbalanced conditions. Particularly, the test conditions for accuracy er-

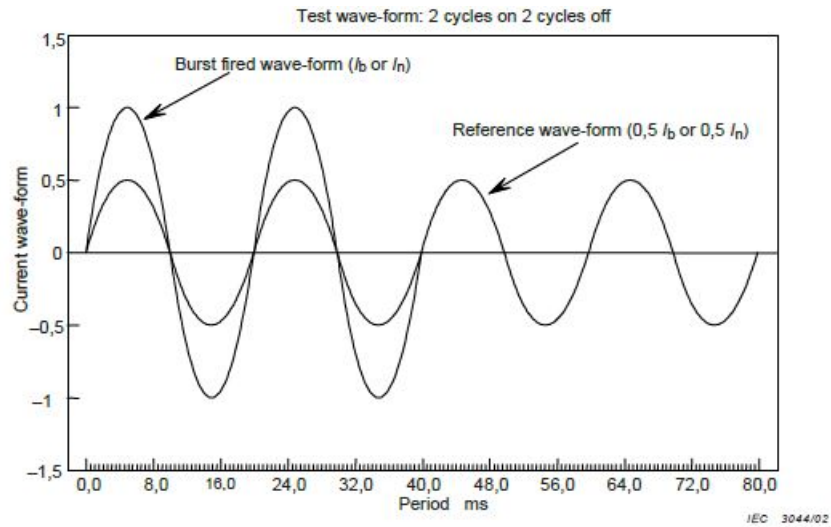


Figure 2.8: Burst fired waveform. Figure taken from [44].

ror due to harmonic distortion have been well defined. Tests for sub-harmonic and high-order harmonic contents have been also included in this document. The recommendations apply only to active electrical energy meters up to 690 V or transformer operated.

Similar to EN 50470 Standards, OIML R 46 defines meter classes designated by an uppercase letter, including class D, which is equivalent to the IEC 65052 0.2S class. In Table 2.5, the percentage error limits for total active energy measurements for meters of each class is shown. These limits are prescribed to estimate the meter intrinsic error at reference conditions with sinusoidal waveform for voltage and current (THD \leq 2%).

Table 2.5: Percentage error limits for the accuracy classes A, B, C and D (OIML R 46).

| Value of current | Power factor | Accuracy class | | | |
|------------------------------|--------------------|---------------------|---------------------|---------------------|---------------------|
| | | A | B | C | D |
| $I_{st} \leq I < I_{min}$ | 1 | $\pm 2.5 \cdot I_l$ | $\pm 1.5 \cdot I_l$ | $\pm 1.0 \cdot I_l$ | $\pm 0.4 \cdot I_l$ |
| $I_{min} \leq I < I_{tr}$ | 1 | ± 2.5 | ± 1.5 | ± 1.0 | ± 0.4 |
| | 0.5 ind to 0.8 cap | ± 2.5 | ± 1.8 | ± 1.0 | ± 0.5 |
| $I_{tr} \leq I \leq I_{max}$ | 1 | ± 2.0 | ± 1.0 | ± 0.5 | ± 0.2 |
| | 0.5 ind to 0.8 cap | ± 2.5 | ± 1.5 | ± 0.6 | ± 0.3 |

Note: $I_l = I_{min}/I$

Accuracy tests for nonsinusoidal conditions

OIML R 46 [21] adopts the same tests prescribed by IEC and MID standards to verify the error shift in meters due to sub-harmonics, d.c. and even harmonics content in the a.c. circuit.

For the compliance with the requirements of maximum error shift due to harmonic contents, OIML R 46 prescribe two waveforms not implemented by IEC or MID standards, but recently adopted by ANSI C12.20-2015. The harmonic content of these waveforms, called Quadriform (Figure 2.9) and Peaked (Figure 2.10), are described in Tables 2.6 and 2.7, respectively. While these waveforms do not correspond to a specific type of electrical loads, they have been designed to include harmonic content and phase shift values commonly found in real-world power systems. The magnitude of each harmonic has been mathematically pre-defined [8].

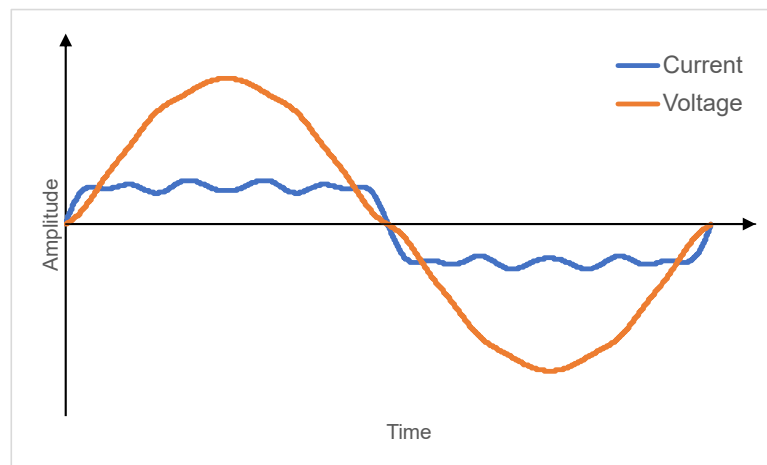


Figure 2.9: Quadriform voltage and current waveforms.

2.4 Calculating Electricity Meter Maximum Permissible Error

All the standards and recommendations outlined in previous subsections establish error limits for electricity meters expressed as a percentage. This relative error is calculated using equation 2.29, according to the ISO guide to the expression of uncertainty of

Table 2.6: Quadriform waveform harmonic content.

| Harmonic number | Current amplitude | Current phase angle | Voltage amplitude | Voltage phase angle |
|-----------------|-------------------|---------------------|-------------------|---------------------|
| 1 | 100 % | 0° | 100 % | 0° |
| 3 | 30 % | 0° | 3.8 % | 180° |
| 5 | 18 % | 0° | 2.4 % | 180° |
| 7 | 14 % | 0° | 1.7 % | 180° |
| 11 | 9 % | 0° | 1 % | 180° |
| 13 | 5 % | 0° | 0.8 % | 180° |

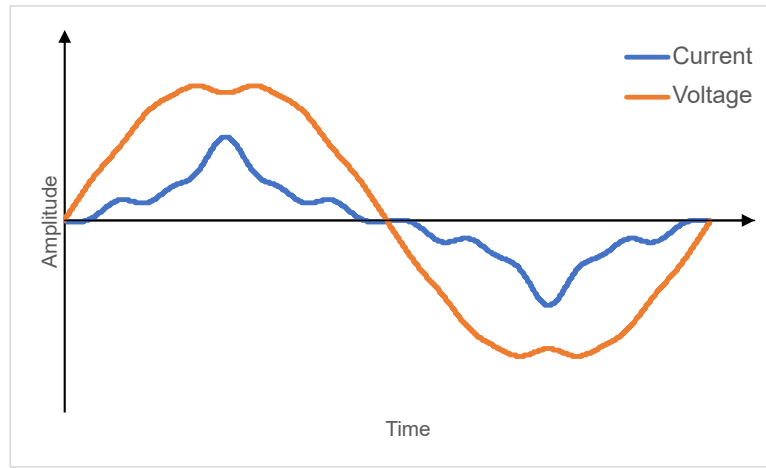


Figure 2.10: OIML R46 Peaked voltage and current waveforms.

measurement (GUM) [51].

$$\text{Percentage error} = \frac{\text{energy registered by the meter} - \text{true energy}}{\text{true energy}} \times 100 \quad (2.29)$$

NOTE Since the true value cannot be determined due to errors introduced by measuring instruments, it is approximated by a value with a stated uncertainty that can be traced to standards agreed upon between manufacturer and user or to national standards [2].

Equation 2.29 is used to calculate the intrinsic error, which refers to the meter error at reference conditions. However, when an influence quantity produces additional percentage error allowed by the standards, the composite error and the maximum permissible error (MPE) should be calculated.

OIML R 46 and EN 50470-1 provide the following useful definitions:

Table 2.7: Peaked waveform harmonic content.

| Harmonic number | Current amplitude | Current phase angle | Voltage amplitude | Voltage phase angle |
|-----------------|-------------------|---------------------|-------------------|---------------------|
| 1 | 100 % | 0° | 100 % | 0° |
| 3 | 30 % | 180° | 3.8 % | 0° |
| 5 | 18 % | 0° | 2.4 % | 180° |
| 7 | 14 % | 180° | 1.7 % | 0° |
| 11 | 9 % | 180° | 1 % | 0° |
| 13 | 5 % | 0° | 0.8 % | 180° |

- **intrinsic error**

percentage error of a meter under reference conditions

- **additional percentage error due to an influence quantity**

additional percentage error of the meter compared to the intrinsic error for the same measurand, when only one influence quantity assumes two specified values, one of them being the reference value

- **composite error**

percentage error calculated from the measured values of the intrinsic error and the additional percentage error due to influence quantities

- **maximum permissible error (MPE)**

extreme value of measurement error, with respect to a known reference quantity value, permitted by specifications or regulations for a given measurement, measuring instrument or measuring system

- **base maximum permissible error**

extreme value of the error of indication of a meter, permitted by relevant standard, when the current and power factor are varied within the intervals given by the rated operating conditions, and when the meter is otherwise operated at reference conditions

In order to calculate the combined maximum permissible error, according to OIML R 46 Annex B, the following assumptions should be made:

Chapter 2. Review of Standard Requirements and Electric Power Definitions for Static Electricity Meters

- a) the integrating (averaging) effect of the meter may be ignored
- b) none of the effects of the influence factors are correlated
- c) the values of the influence quantities are more likely to be close to the reference values than to limits of the rated operated conditions
- d) the influence quantities, and the effects of the influence factors, can be treated as Gaussian distributions, and thus a value of half the maximum permissible error shift can be used for the standard uncertainty

then the combined maximum permissible error v (assuming a coverage factor of two corresponding to a coverage probability of approximately 95 %) can be estimated using the formula:

$$v = 2 * \sqrt{\frac{v_{base}^2}{4} + \frac{v_{voltage}^2}{4} + \frac{v_{frequency}^2}{4} + \frac{v_{unbalance}^2}{4} + \frac{v_{harmonic}^2}{4} + \frac{v_{temperature}^2}{4}} \quad (2.30)$$

where:

- v_{base} is the base maximum permissible error;
- $v_{voltage}$ is the maximum error shift permitted for voltage variation;
- $v_{frequency}$ is the maximum error shift permitted for frequency variation;
- $v_{unbalance}$ is the maximum error shift permitted for unbalance variation;
- $v_{harmonic}$ is the maximum error shift permitted for the variation of harmonic content;
- $v_{temperature}$ is the maximum error shift permitted for temperature variation.

OIML R 46 Annex B also provides guidance to estimate the combined error based on type tests results and specific conditions. Two methods are proposed, depending on the statistical error distribution, i.e. Gaussian or rectangular distribution (i.e. the error distribution has a constant probability) may apply.

Chapter 2. Review of Standard Requirements and Electric Power Definitions for Static Electricity Meters

If the assumption of a Gaussian distribution is valid, the combined maximum permissible error can be estimated from a combination of test results using the formula:

$$e_{c(p,i)} = \sqrt{(e^2(PF_p, I_i) + \delta e_{p,i}^2(T) + \delta e_{p,i}^2(U) + \delta e_{p,i}^2(f))} \quad (2.31)$$

where:

for each current I_i and power factor PF_p

- $e(PF_p, I_i)$ is the intrinsic error of the meter measured in the course of the tests, at current I_i and power factor PF_p ;
- $\delta e_{p,i}(T)$, $\delta e_{p,i}(U)$, $\delta e_{p,i}(f)$ are the maximum additional errors measured in the course of the test, when the temperature, the voltage and the frequency are respectively varied over the whole range specified in the rated operated conditions, at current I_i and power factor PF_p

When assuming that a Gaussian distribution may no longer be valid, instead a rectangular distribution should be assumed for the effects of influence factors. Thus, the combined maximum error can then be estimated from a combination of test results using the formula:

$$e_c = 2 * \sqrt{\frac{e_{base}^2}{3} + \frac{e_{voltage}^2}{3} + \frac{e_{frequency}^2}{3} + \frac{e_{unbalance}^2}{3} + \frac{e_{harmonic}^2}{3} + \frac{e_{temperature}^2}{3}} \quad (2.32)$$

where:

e_{base} is the maximum error obtained in the test for base maximum error;

$e_{voltage}$ is the maximum error shift obtained in the test for voltage variation;

$e_{frequency}$ is the maximum error shift obtained in the test for frequency variation;

$e_{unbalance}$ is the maximum error shift obtained in the test for unbalance variation;

$e_{harmonic}$ is the maximum error shift obtained in the test for variation of harmonic content;

$e_{temperature}$ is the maximum error shift obtained in the test for temperature variation.

Chapter 2. Review of Standard Requirements and Electric Power Definitions for Static Electricity Meters

All maximum error components in formula 2.32 (i.e. e_{base} , $e_{harmonic}$, etc.) takes into account the measurement uncertainty of the type test.

2.4.1 Chapter Summary

This chapter has firstly presented a review of the main accuracy requirements prescribed by standards applicable to electricity meters, with focus on the tests and test conditions for nonsinusoidal situations applied to SEMs in order to be certified by organizations such as MID. A brief summary of the reviewed standards and supporting documents with coverage related to nonsinusoidal signal tests is given in Table 2.8.

In Table 2.8, a summary of the accuracy tests and the related waveforms applied to electricity meters in order to meet the requirements of different standards is presented. From the reviewed tests, it has been discussed that allowed nonsinusoidal signals are designed with predefined harmonic content based on a conservative survey-based approach which does not fully represent the very large number of shapes a nonsinusoidal signal can have. These test requirements are relatively easy to meet by electronic electricity meters. However, certified electricity meters can exhibit significant errors (as described in Chapter 3), beyond prescribed limits, when exposed to nonsinusoidal signals with two characteristics omitted in the standard tests: fast amplitude changes and a non-zero phase shift. These two signal parameters (time duration of amplitude changes and phase shift) are missing and are therefore further analyzed by this thesis.

Secondly, in this chapter, the newest electric power quantities definitions issued in the IEEE 1459 standard have been described. These formulas are appropriate for revenue metering applications and can be easily implemented by SEMs, although their implementation is not yet compulsory to any electricity meter in order to obtain MID approval.

Finally, separation of total and fundamental electric power quantities, as suggested by IEEE 1459 standard, allows fairer ways to bill customers for consumed electrical energy and makes a step forward to clearly identify the sources of undesirable voltage and current distortion at the metering point.

Table 2.8: Harmonic content influence accuracy tests.

| | | ANSI C12.1 | ANSI C12.20 | IEC 62053-21 | IEC 62053-22 | EN 50470-3 | OIML R 46-2 |
|---|-----|------------|-------------|--------------|--------------|------------|-------------|
| Accuracy class (expressed as a full scale percentage error) | 2 | – | – | X | – | X | X |
| | 1 | X | – | X | – | X | X |
| | 0.5 | – | X | – | X | X | X |
| | 0.2 | – | X | – | X | – | X |
| | 0.1 | – | X | – | – | – | – |
| Harmonic accuracy tests | | | | | | | |
| Harmonic components in the current and voltage circuits (5th harmonic only) | | – | – | X | X | X | X |
| d.c. and even harmonics in the a.c. circuit (half recti- fied) | | – | – | X | X | X | X |
| Odd harmonics in the a.c. current circuit (phase fired) | | – | X | X | X | X | X |
| Sub-harmonics in the a.c. circuit (burst fired) | | – | – | X | X | X | X |
| Quadriiform | | – | X | – | – | – | X |
| Peaked | | – | X | – | – | – | X |

Chapter 3

Analysis of Static Electricity Meter Design and Reported Accuracy Errors

3.1 Introduction

Modern and future power systems require accurate measurements for a wide range of applications such as control, protection, and electrical energy consumption billing. The overall accuracy of measured electrical quantities depends on individual error contributions from different stages of the signal path within the measurement instrument, as well as the power quality conditions of the grid. Present developments in hardware and signal processing techniques allow accurate measurements of voltage and current signals in almost any possible scenario. Nevertheless, in order to achieve the required level of accuracy, considerations should be given when choosing components for the different stages of the measuring instrument design. In this chapter, a review and analysis of some of the most common hardware components and signal processing techniques for electrical metering instruments is presented.

3.2 Analogue Front-End

The analogue front-end (AFE) components (Figure 3.1) for sampling-based instruments designed to measure electrical quantities typically follow a similar design regardless of the function of the device (e.g. smart electricity meter, power quality analyser, or protection relay). However, depending on the particular application, certain features or characteristics, should be considered for each stage. In this section, an analysis of the AFE components and their influence on the accuracy of electricity meters under nonsinusoidal waveform conditions is provided.

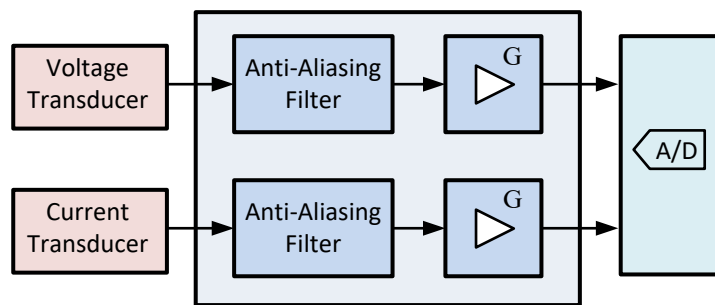


Figure 3.1: Electricity meter analogue front-end.

3.2.1 Sensors/Transducers

Transducers are known to be the main sources of uncertainty in measurement digital equipment as their errors are, in most cases, one order of magnitude greater than other uncertainty contributions [17], and this is particularly true for electricity metering devices. The most common transducers for power systems metrology applications are: voltage transformers (VT) or resistive voltage divider (RVD) for the voltage inputs; and current transformers (CT), current shunt resistors, Rogowski coils, zero-flux transformers or Hall effect clamps for the current inputs. When using a particular transducer (or sensor) technology it is important to consider not only the accuracy of the transducer itself, typically provided by the manufacturer in the data sheet, but also some characteristics such as frequency response and phase delay must be known or characterized in order to reduce additional sources of error.

The requirement to have a d.c.-coupled input is also relevant to the choice of the

transducer, as power system metrology applications for power quality often need to measure very low frequencies, such as subsynchronous interharmonics. A d.c.-coupled transducer also achieves a better input match or voltage standing wave ratio (VSWR) performance, compared to an a.c.-coupled transducer, due to the absence of a large in-series capacitor.

3.2.1.1 Voltage Sensors

Inductive voltage transformers are broadly used in measurement systems together with electricity meters, phasor measurement units (PMUs) and power quality analyzers, as they are very accurate and provide inherent galvanic isolation. However, this sensor type introduces a ratio error and a phase displacement error [52, 53] which should be compensated accurately. VT frequency response is limited and in general lower compared to the frequency response of a resistive voltage divider [54]. Therefore, for applications that require measurement of high frequencies, such as harmonics or other power quality phenomena which are characterized by frequencies considerably higher than 50 or 60 Hz, resistive voltage dividers might be a better choice compared to inductive transformers. Examples of sensor equivalent circuits (for VT and RVD) for line voltage measurements on power systems are shown in figure 3.2.

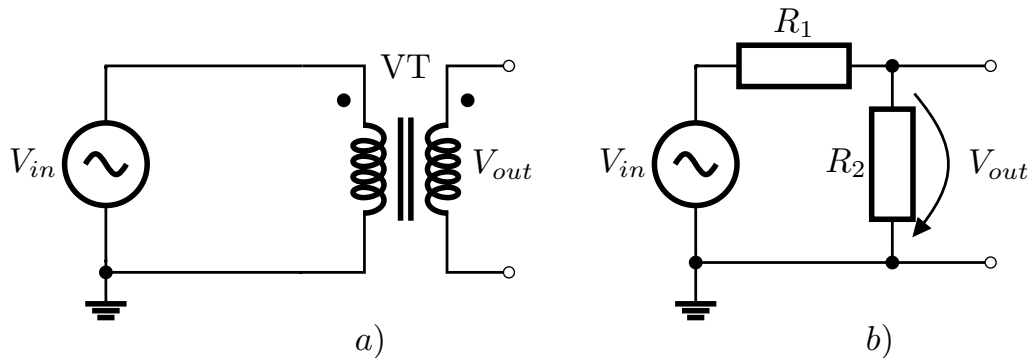


Figure 3.2: Voltage sensors: a) inductive transformer, b) resistive voltage divider.

3.2.1.2 Current Sensors

The various technologies for sensing current signals offer benefits and drawbacks which should be considered, and are summarised in Table 3.1. It is important that the selected current sensor meets the targeted accuracy over the full intended dynamic range [55].

Table 3.1: Current sensor technologies: benefits and drawbacks.

| Sensor | Benefits | Drawbacks |
|-----------------------------|---|---|
| Low Resistance Shunt | Very low cost, good linearity | Poor high current capability, d.c. offset, parasitic inductance |
| Current Transformer | Good high current performance, low power consumption | Hysteresis/saturation due to d.c., phase shift, susceptible to external magnetic fields |
| Hall Effect Sensor | Good high current performance, wide dynamic range | Hysteresis/saturation, higher cost, temperature drift |
| Rogowski Coil (Air-Core CT) | Low cost, no saturation limit, low power consumption, immunity to d.c. offset, wide dynamic range, very low temperature range | Output is derivative of voltage signal—requires an analogue (or digital) integrator. EMI sensitivity. |

The phase response is particularly important for power measurements, and clamps and Hall effect devices can often have phase errors of several degrees. Phase is also important for waveform shape reconstruction, where increasing phase errors at higher frequency harmonics can distort the time domain shape of a captured waveform. If the phase error is stable and can be measured, it is possible to correct the response using deconvolution methods [56].

Openable Rogowski coils and Hall clamps have the advantage of non-invasive measurements without the need to break the current circuit. However, they are susceptible to significant errors due to rotation and position on the current carrying conductor [26, 57, 58]. Furthermore, recent studies have pointed out that Rogowski coils and Hall sensors as the sensing technology most prone to introduce large errors under non-sinusoidal situations [26, 59–61] on residential electricity meters. The aforementioned studies do not explain the causes of the error introduced by Rogowski coils or Hall-effect current sensors, but such errors are related to their physical design (i.e. the geometry)

and their frequency response when measuring non-linear systems.

3.2.2 Anti-Aliasing Filter

An anti-aliasing (AA) filter is an analogue low-pass filter designed to prevent the alias effect caused by undesirable signals with a frequency greater than half the sampling frequency of an analogue to digital converter (ADC). The purpose of an anti-aliasing filter is to restrict the bandwidth of a signal to satisfy the Nyquist theorem which states that an analogue signal should be sampled at more than twice the highest frequency component of the signal [62]. Depending on the ADC sampling frequency, appropriate AA filters should be placed directly after the transducers. Oversampling ADCs eases the design requirements of the AA filter allowing for low order filters that can be implemented passively. For power and energy applications, the cut-off frequency of the filter should prevent aliasing effect but it should not filter out signals in the frequency band of interest. Furthermore, it has been demonstrated that the cut-off frequency of AA low-pass filters has a strong impact on the measured energy value when the amplitude of harmonic components on the voltage or current signals is significant [63].

AA filters for voltage and current signals should be identical to prevent large energy errors at lower power factors [64]. The phase of the AA filter adds to the error of the instrument and needs to be characterized and corrected. When digital filters are used with oversampling ADCs, the group delay of these filters is a factor which must be corrected for measuring absolute phase [65,66].

3.2.3 Gain Stage

For some instruments, the gain stage may be not mandatory, as long as the signals from the transducer are within the ADC input range. Nevertheless, for a more flexible design, a differential input programmable gain amplifier (PGA) is desirable. This PGA will allow changing transducers in the future, without the need for re-designing the rest of the system. The PGA gain should be selected in such a way that the signals never exceed the ADC input range.

The gain stage can also act as an impedance buffer preventing loading of the trans-

Chapter 3. Analysis of Static Electricity Meter Design and Reported Accuracy Errors

ducer by the ADC input impedance (if this is insufficiently high). This is particularly important for shunts and RVD transducers where a relatively low impedance will load the transducer and give a predicable and correctable error.

The following additional factors may need to be considered:

- The gain stage may also incorporate an integrator for Rogowski coils. The integrator, typically implemented as a digital block in a DSP unit, could restrict the meter frequency response and introduce a delay that should be compensated.
- The temperature coefficient of gain setting resistors is an important factor for instrumentation.
- d.c. offsets in amplifiers are important for d.c.-coupled systems and when integrators are used.
- The bandwidth and time constant of the amplifier must be considered.
- The common mode rejection ratio (CMRR) is important, particularly for current measurements where one side of the circuit is not at earth potential.
- Noise is also a factor which could introduce measurement errors, and the desired effective number of bits (ENOB) should be considered [67] to minimize additional sources of error.

3.2.4 Protection and Isolation Components

Overload protection circuits are also used in commercial instruments; these may be fused circuits using diode or transient voltage suppression (transorb) circuits. High rupturing capacity (HRC) fuses should be used for substation situations where the fault level is high. Care should be taken that these circuits do not introduce amplitude and phase errors.

For safety reasons, galvanic isolation should be placed between the power signals and the measurement system. Although some sensors provide inherent galvanic isolation, it is good practice to include either analogue or digital isolation inside the meter.

Analogue isolators available on the market use different isolation technologies, such as capacitive or inductive barrier, and may introduce amplitude and phase errors which can be easily compensated, due to their linear behaviour.

Digital isolators, on the other hand, do not create amplitude and phase errors, as they operate under an optical isolation barrier approach to safely transmit digital data. Digital isolators can be placed immediately after the ADC or, more frequently, after the processing unit.

3.2.5 Analogue to Digital Converter

Accurate measurement of electrical quantities in the power grid is critical for monitoring the operating state of the grid and real-time decision making, because these measurements are the inputs for protection algorithms and control applications. The ADC, as part of the measurement chain in the analogue front-end, plays an important role on the accuracy of a measuring instrument. There are a number of ADCs on the market which differ in terms of the architecture, resolution, sampling rate, conversion time, and number of channels.

One important characteristic that has to be taken in consideration is the way the ADC samples the input signal, i.e. the architecture. Successive approximation register (SAR) ADCs (Fig. 3.3) perform conversions by taking a sample from the input signal and achieving the conversion. This architecture provides very low latency. The latency depends mainly on the SAR algorithm processing time which is required to determine all the bits of the input signal; this can be reduced by operating the ADC at higher speed.

For those applications requiring low latency and precise information, the SAR architecture is advantageous. SAR ADCs are also desirable features for measuring fast signal transients.

Sigma-delta, sometimes referred to as $\Sigma\Delta$ ADCs (figure 3.4), sample the signal continuously for a specified time interval and output the conversion result that corresponds to the average of samples over that period of time. An important feature of this architecture is the oversampling capability and the integration of signal conditioning blocks

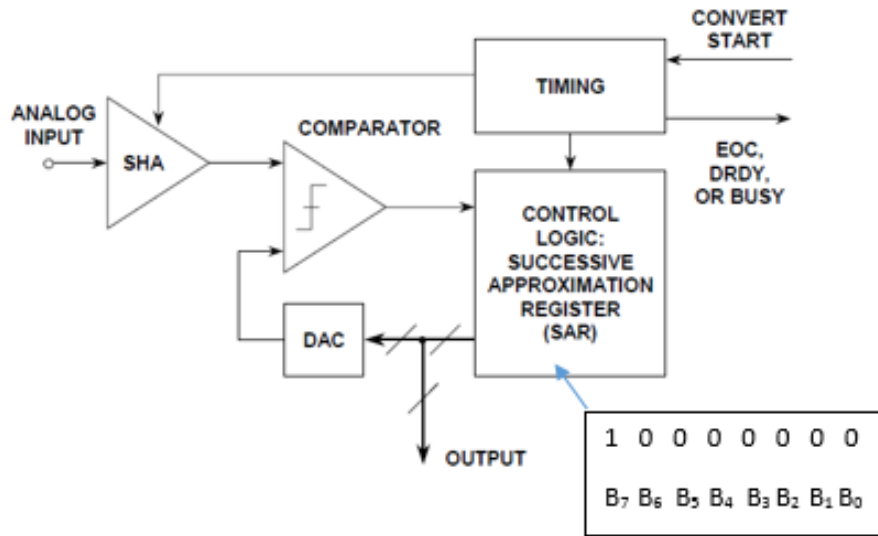


Figure 3.3: SAR ADC architecture (part of this figure is taken from [68])

such as PGA's, phase compensation registers and digital filters, which aim to reduce the quantization noise generated internally in the ADC and, consequently, improve the signal to noise ratio (SNR) and ENOB.

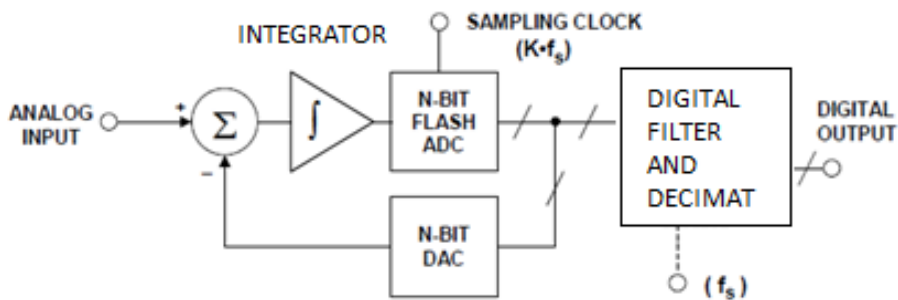


Figure 3.4: Sigma-delta ADC architecture [68]

Choosing the appropriate ADC therefore involves a tradeoff, but in most cases the application itself guides the selection. That is, in applications where a very large bandwidth is required, the high speed architectures such as 'flash converters' are an appropriate choice, but the overall resolution is relatively low from 8 [68] to 12 bits. In industrial measurement applications including power, energy, and phasor measurements, where the bandwidth of interest is few kHz, low speed architectures such as sigma-delta converters are advantageous because of the high resolution that this ar-

Chapter 3. Analysis of Static Electricity Meter Design and Reported Accuracy Errors

chitecture offers. For power quality monitoring applications where the electromagnetic phenomena vary from a few Hz to 5 MHz [69], medium speed architectures such as SAR converters are a better choice due to a good combination of speed and resolution.

Power system measurements require high-performance ADCs, with some desirable features such as: high resolution (typically 24-bit), differential inputs, simultaneous sampling and oversampling capabilities. The sigma-delta ADC architecture offers a better trade-off between resolution and sampling rate compared to a SAR ADC. Additionally, the delays introduced by delta-sigma ADCs can be calculated and therefore can be compensated in time-sensitive applications [66].

In Table 3.2, a comparison of representative simultaneous-sampling ADCs of different architectures, specifically designed for electrical power measurements, is presented. From this Table, the most advantageous features, highlighted in bold text for this kind of application, can be observed. It can be concluded that the MAX11046 IC which contains 8 independent SAR ADCs, has a larger bandwidth and a greater SNR, making it a better choice for measuring signals which can contain fast transients. The ADE7878A incorporates 7 independent 24-bit $\Sigma - \Delta$ ADCs, with a reduced bandwidth and differential inputs which contributes to reduce the common-mode noise. The ADE7878A has a better resolution and it is ideal for electrical power and energy measurements of signals without such fast transients.

Although $\Sigma\Delta$ ADCs are the most popular signal conversion technology employed in electricity meters and specialized integrated circuits, the reduced bandwidth, compared to SAR ADCs, restricts the accuracy of SEMs when exposed to fast signal transients, such as impulsive voltages and currents, due to internal digital filter's frequency response.

However, SAR ADCs need compensation for the phase delays introduced by voltage and current inductive sensors, which needs to be continuously compensated via software by an external processor [70]. SAR ADCs also need external components such as amplifiers to drive the ADC inputs. The input AA filter is also more complex for SAR ADCs, often requiring an external buffer or an amplifier with a sufficient bandwidth [71].

Additionally, the higher the resolution of ADC, the more data that is generated. A

Table 3.2: Simultaneous-sampling ADCs comparison.

| Parameter | MAX11046 | ADE7878A |
|------------------|-----------------|---------------------|
| Channels | 8 | 7 |
| Resolution | 16-bit | 24-bit |
| Sample Rate | 250 ksps | 1.024 Msps |
| Bandwidth | 4 MHz | 4 kHz |
| SNR | 85.2 dB | 74 dB |
| Architecture | SAR | $\Sigma - \Delta$ |
| Input type | Single-ended | Differential |

24-bit device generates three 8-bit words per sample increasing the real-time burden of the digital signal processor (DSP), particularly for higher sampling rate systems. The improved noise performance of high resolution devices can be usefully employed by disregarding data bits of low significance to keep the processing manageable.

Over-range flags, where applicable, should be used to indicate to the CPU that saturation has occurred so that the user display can indicate that the result is invalid.

The ADC on some multichannel instruments can be multiplexed. The effect of this on inter-channel phase needs careful consideration because each channel may not be sampled at the same instant.

3.3 Digital Signal Processing

The processing unit is typically a microprocessor (μP), DSP, or field-programmable gate array (FPGA), which is responsible for performing the mathematical computation of electrical quantities from the digitized inputs. The processing unit should be fast enough and computationally capable to meet the application requirements. For example, for a phasor measurement unit (PMU) device, a “hard” real-time processing platform may be desirable to ensure that data is processed and delivered with bounded latency.

The CPU must be fast enough to handle the data stream in real-time. Buffers can be used to hold data whilst the processor multitasks, but the processing speed must be sufficient to prevent the buffers overflowing and losing samples. The data can

Chapter 3. Analysis of Static Electricity Meter Design and Reported Accuracy Errors

be indexed in some way (such as using a counter) to check for missed data which, if undetected, can give rise to significant errors.

There are a number of hardware factors that influence the performance of the processing unit [72], including: clock frequency, processor latency, memory access time, and the protocol used by the processor to communicate with peripheral devices. Software factors include: algorithm complexity and the ability to parallelise the tasks in order to process the information simultaneously in the cores of a multicore system processor. All of these factors need a careful consideration when deciding which processor is best for a particular application.

3.3.1 Energy Metering Integrated Circuits

Energy metering integrated circuits are specialized mixed-signal circuits, which may incorporate AFE components, such as the PGA and ADC, as well as the processing unit. These circuits are convenient to ease the design of electricity meters and power quality monitoring instruments, as the embedded processor performs the necessary mathematical calculations. Nonetheless, it is important to verify the IC compliance with applicable standards (MID or ANSI, please see 2.3), and also to verify the formulas implemented to calculate electrical quantities.

The internal composition of the aforementioned ICs varies among vendors, and among different models offered by a single vendor. A simplified common architecture for a single-phase electricity meter is shown in Figure 3.5. The metering IC's representative block diagram is composed of analogue components such as programmable gain amplifiers (PGA) and $\Delta\Sigma$ ADCs. This kind of IC also incorporates digital blocks such as high-pass filters (HPF), an integrator for Rogowski coils, and digital blocks to calculate electrical quantities and compensate for gain or offset errors. ICs designed to be utilized in three-phase power systems implement three identical (and independent [19]) single-phase voltage and current signal paths to calculate the relevant electrical quantities.

Some desirable features, from the metrology perspective, are the capability of compensating (via software), parameters such as phase, gain, and offset, as well as the

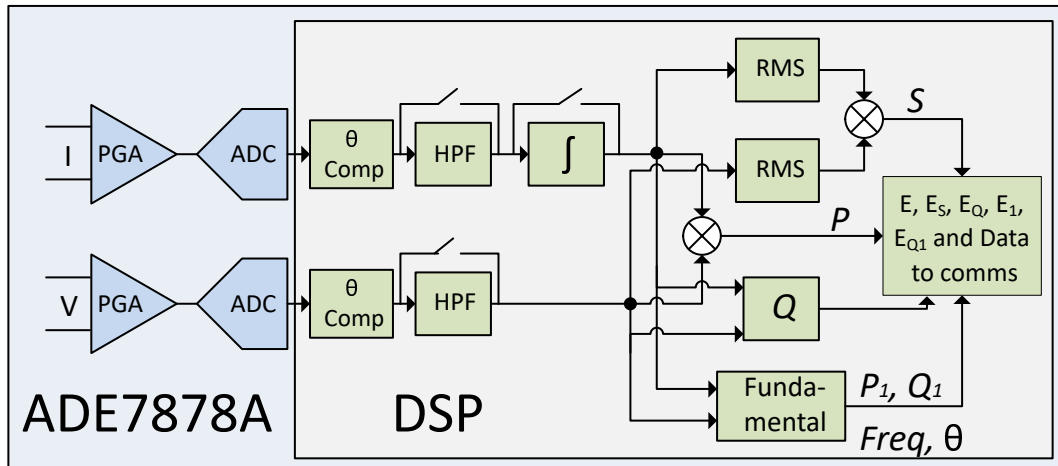


Figure 3.5: Single-phase energy metering integrated circuit block diagram

IC current sensor compatibility. In Table 3.3, a comparison of energy metering ICs features from different vendors is presented. It is worth noting that all IC models in Table 3.3 claim an accuracy of 0.1 %, despite the difference in their internal ADC resolution (e.g. 16, 21 or 24 bits), but only a few models meet the requirements of the most constraining standards and international recommendations for tests and test conditions such as the OIML R 46 (see 2.3.3.1). The IEC 62053-24 standard for reactive energy at fundamental frequency, and the implementation of rms measurements over half a cycle, as per described in IEC 61000-4-30 standard, are also performed by some of these commercial devices.

Another important consideration when choosing an energy metering IC is the possibility to obtain the calculations of parameters related to the fundamental frequency, such as fundamental active power (P_1), fundamental reactive power (Q_1), fundamental active energy and fundamental reactive energy. Such capabilities of distinguishing fundamental and nonfundamental powers and energies, as well as the possibility of updating (or upgrading) the IC firmware will provide the final design with some extra flexibility, as the standards and the test conditions are prone to change over the instrument's lifetime span.

Table 3.3: Energy Metering ICs comparison.

| Energy Metering IC | Type | ADC Resolution | Accuracy (Active Power) | Bandwidth | Supported Current Sensor | Supported Standards | Special Features/Comments |
|--------------------|---------|----------------|-------------------------|----------------------|--------------------------|---|--|
| ADE7878 | 3-Phase | 24-bit | 0.1 % | 4 kHz | CT, Rogowski | EN 50470-3; IEC 62053-21,22,23 EN50470-3; IEC 62053-21,22,23; OIML R 46; ANSI C12.20; IEC 62053-24 | Waveform Sampling Waveform Buffer rms $\frac{1}{2}$ cycle |
| ADE9000 | 3-Phase | 24-bit | 0.1 % | 7.2 kHz | CT, Rogowski | EN50470-3; IEC 62053-21,22,23; OIML R 46; ANSI C12.20; IEC 62053-24 | Autocalibration rms $\frac{1}{2}$ cycle |
| ADE9153 | 1-Phase | 24-bit | 0.1 % | 1.6 kHz | CT, Shunt | EN50470-3; IEC 62053-21,22,23; OIML R 46; ANSI C12.20; IEC 62053-24; | Multiplexed ADC |
| 71M6513 | 3-Phase | 21-bit | 0.1 % | Estimated at 1.2 kHz | CT, Rogowski, Shunt | IEC 62053; ANSIC 12.20 IEC62052-11; IEC62053-22; | Lowest temperature drift |
| ATM90E36A | 3-Phase | 16-bit | 0.1 % | 2 kHz | CT, Rogowski | IEC62053-23; ANSI C12.1 and ANSI C12.20 | Single-point calibration for active energy |
| ATM90E26 | 1-Phase | 16-bit | 0.1 % | 1.1 kHz | CT, Shunt | EN 50470-x; IEC 62053-2x; ANSI12.2x | Dual mode ap-parent energy calculation |
| STPM32 | 3-Phase | 24-bit | 0.1 % | 3.6 kHz | CT, Rogowski, Shunt | | |

3.3.2 Gain, Offset and Phase Adjustment

Modern energy metering ICs, such as those found in Table 3.3, have internal registers to compensate gain, offset and phase errors commonly introduced by transducers and analogue front-end components. There are registers to adjust independently any of the aforementioned parameters, for every available current and voltage channel. Additionally, some ICs implement further gain and offset correction after the power(s) calculation, in order to compensate errors introduced by digital blocks within the IC's DSP (e.g. digital filters).

3.3.3 Digital Filters

Digital filters are commonly implemented inside energy metering IC's for different purposes such as noise mitigation, d.c. component removal, estimation of fundamental-frequency electrical quantities, and calculation of line frequency based on zero-crossing techniques. While both IIR (Infinite Impulse Response) and FIR (Finite Impulse Response) filters can be implemented within an IC's DSP, FIR filters are preferred for power systems metrology applications due to their stability and because they do not introduce phase distortion error, compared to IIR filters with a non-linear phase response. Some advantages and disadvantages of FIR and IIR filters are provided in Table 3.4.

Table 3.4: Digital Filters: advantages and disadvantages.

| Filter type | Advantages | Disadvantages |
|-------------|-----------------------------------|---|
| IIR | Low implementation cost | Non-linear phase characteristics |
| | Low latency | Can be unstable |
| FIR | Linear phase | High computational and memory requirement |
| | Very stable | Higher latency (compared to IIR filter) |
| | Less prone to quantization errors | |

High-Pass Filter

In order to eliminate errors introduced by d.c. components, a digital high-pass filter (HPF) is placed after the ADC. ADC outputs can contain a d.c. offset which may introduce additional errors in power and rms calculations [73]. The HPF can be disabled and they are placed in both current and voltage channels.

3.3.4 Digital Integrator

The di/dt current sensor (i.e. Rogoswki coil) output is a voltage proportional to the magnetic field produced by an a.c. current flowing in a conductor. In order to translate this voltage to a current corresponding value, the signal needs to be filtered by means of an integrator. While the integrator could be implemented with analogue components, energy metering ICs that support signals from di/dt sensors often incorporate a digital integrator. The digital integrator can be disabled to allow different current sensing technologies.

Due the characteristics of the digital integrator, an appropriate AA filter should be implemented in the AFE if di/dt sensors are going to be used. For example, the digital integrator within the ADE7878A energy metering IC has a -20 dB/dec attenuation and approximately -90° phase shift, which requires an AA filter of at least the second order [73] to fully compensate the typical 20 dB/dec gain associated with the di/dt sensor.

3.3.5 Measurement of Electric Power Quantities

Once the data has been converted to a digital representation, it should be processed accordingly to accurately calculate the required electrical quantities. Different approaches and formulas may be used for this purpose.

To calculate electrical quantities such as energy, power (active and reactive), power factor, and frequency, different approaches may be used (e.g. Budeanu or Fryze definitions), which are equivalent in sinusoidal conditions, but lead to different and erroneous results when nonsinusoidal or unbalanced situations exist [25]. The disadvantages of implementing definitions which are non-physical-based, such as the Budeanu approach

has been widely discussed and criticized by many authors [23, 35, 74], yet is often implemented in commercial metering instruments, as standards and regulatory bodies presently permit this approach [25].

The IEEE 1459-2010 standard [20], on the other hand, includes suitable definitions to perform the calculations of electrical measurements under different power quality conditions, such as sinusoidal, nonsinusoidal, balanced or unbalanced conditions, which are frequently present in real-world scenarios. IEEE 1459-2010 standard is meant to be the reference for new electrical measuring instruments designs, particularly, for revenue purposes. The definitions of nonfundamental, nonactive power SN and its components, current distortion power (D_I) and voltage distortion power (D_V), “quantifies the overall amount of harmonic pollution delivered or absorbed by a load” and may be implemented by a new generation of electricity meters. Even though this standard was issued ten years ago, it is very hard (if not impossible) to find commercially available measuring instruments implementing such electrical definitions. However, modern digital metering technology is capable of implementing such definitions in a DSP or even in a commercial energy metering IC by means of a firmware upgrade, as has been done in [8]. Therefore, this thesis proposes the implementation of IEEE 1459-2010 definitions in a commercial energy metering IC model as described fully in chapter 4, section 4.4. The model developed in this thesis is useful to predict the response of the IC to nonsinusoidal, fast-changing or pulsed currents if such a firmware upgrade is possible.

3.3.6 Energy Accumulation

Energy Metering ICs need to work together with an external controller device (e.g. a microcontroller or a DSP) which is responsible for managing communications to output data and the IC’s configuration. Energy accumulation is often performed by this external digital processor. Once the DSP (or main digital processor) has calculated the energy flowing at the measuring point over a defined period of time (e.g. every cycle or once a second), the obtained energy value should be accumulated on a digital register to calculate the total amount of energy consumed or delivered by a consumer/prosumer. Care should be taken to consider the energy flows in both directions to properly dif-

ferentiate the energy imported from or exported to the grid. For this purpose, energy metering ICs offer the capability to monitor the sign of calculated energy values.

3.4 Reported Accuracy Errors in Static Electricity Meters

Applicable accuracy standards and regulations for SEMs indicate a maximum distortion factor (THD) of 3% of the sinusoidal waveform for voltage and current during the device calibration and testing, which is not representative of many modern or future dynamic power quality scenarios. New tests and recommendations, such as those provided in the OIML R 46 document [21] (see 2.3.3.1), have been issued by regulatory bodies, but they are still not mandatory for meters to be certified.

During the last few years, SEMs have been deployed in several countries all around the world, replacing the dependable electromechanical meter and even other electronic meters. Such deployed meters have been designed and calibrated using sinusoidal operational conditions, but some of them present measurement errors when the voltage or current signals are nonsinusoidal. Therefore, researchers of multiple institutions including several universities [11, 13, 15, 18, 23, 75–79] and national metrology institutes such as NPL in the UK [16, 80, 81] and VSL in the Netherlands [19, 59, 60] have been trying to address the problem of erroneous measurements on SEMs, by means of applying nonsinusoidal waveforms to electricity meters.

The important efforts which have been expended to quantify the effects of nonsinusoidal waveform conditions on the accuracy of electricity meters will be reviewed in the following subsections. Several laboratory-based tests with non-linear loads, programmable power supplies (with random or predefined harmonic content), as well as theoretical analysis and simulations, which can be found in the recent literature will be analyzed. They either try to quantify the error or make a comparison between different technologies of electricity meters, e.g. electromechanical versus static meter. Sections 3.4.1 to 3.4.4 present detailed analysis of some of the most representative accuracy errors in static meters reported in the literature as well as the tests and proposed

solutions to address these problems.

3.4.1 Conducted Electromagnetic Interference on Electricity Meters

Conducted electromagnetic interference has been rapidly increasing in power systems during the last decades due to the proliferation of non-linear loads, such as switching power electronic devices, causing errors in electricity meter readings and in some cases, damage to electrical equipment [82]. Introduction of new technologies, like motor speed drivers, energy saving lamps and power line telecommunications (PLT) could contribute to worsen conducted electromagnetic interference over the next years. In the next paragraphs, a couple of representative cases, where conducted electromagnetic interference causes error in electricity meter readings, are presented.

A good example that exposes how conducted electromagnetic interference could be responsible for accuracy errors in electricity meters is presented in [82], where two neighboring farmers, each with identical photovoltaic systems installed, experienced a difference of 60% in the energy production reported by the electricity meters installed at their facilities. It was found that in the farm with the lowest production (only 40% compared with the neighbour farm's energy production) a forced ventilation system, controlled by a power drive system (PDS), produces fast rise-time common mode voltage (7 Vpk) and common mode current when the fans were operating at full speed. This interference, caused by the power drive system, was found to be responsible for the measurement differences among meters. The problem was solved after replacing the PDS which was producing voltage waveforms with superimposed pulsed, fast-changing signals.

A consumer observed high energy meter readings [61] when using an off-the-shelf water pump (for fish pond applications) at his premises. It was found that the remote control used to adjust the pump capacity was generating small pulsed currents which produced large deviations in the installed electricity meter when compared to the readings of a reference meter. Thus, the water pump was tested in laboratory conditions and the readings of ten static meters (with different characteristics and sensor technologies) were compared to the calculations of a reference power analyzer at the

Chapter 3. Analysis of Static Electricity Meter Design and Reported Accuracy Errors

Dutch Metrology Institute (VSL). In addition to testing the pump for different power levels, tests with different power supply impedance values were performed as follows: a) VSL's mains power supply, and b) an ideal power supply with three impedance levels (i.e. standardized mains impedance, low impedance and high impedance network). Results from the performed experiments showed deviations between -19% and +483% when the standardized main impedance was used, whereas the low impedance network causes deviations between -17% and +2114%. The high impedance network produces the lowest deviations between -16% and +316%, and the mains power supply of the building reported the highest deviations between -56% and +2675%. The authors concluded that higher deviations occur when the current has a higher phase shift and that "in household situations, even higher deviations can occur than in controlled lab experiments". Again, the conducted interference produced by pulsed currents was responsible for reported EEMs misreadings and the error magnitude has been found to be proportional to the current phase shift.

3.4.2 Comparative Tests

The authors of [12] ran three different "distorted load" sets and one "linear load" set for three different electricity meters: one analogue (electromechanical), one digital (electronic) and one hybrid meter. The loads (connected in different configurations for each set) consisted of resistive loads controlled by dimmers, compact fluorescent lamps (CFL) and capacitors. The measurements of the tested meters were compared with the values obtained with a calibrated energy system analyser. In all the tests, the most accurate meter was the electromechanical and the worst performance corresponds to the electronic, with a maximum error of 6%, which is not negligible at all. These results may be surprising, as digital metering technology is supposed to be advantageous compared to its analogue counterpart, but more recent and better performed tests described later in 3.4.3, support the sensitivity of EEMs to nonsinusoidal waveforms whereas analogue meters response to harmonic signal components does not causes metering errors as high as in EEMs.

One of the most recent studies [26], where ten static meters were compared with the

Chapter 3. Analysis of Static Electricity Meter Design and Reported Accuracy Errors

measures of an electromechanical meter, have reported a significant deviation in the majority of static energy meters, compared with the performance of electromechanical devices. The tests include LED lamps, CFLs, dimmer at different angles and a line choke, connected in different configurations for each test. The highest deviation values of static meters are in the order of 560% to 582% with respect to the electromechanical. For such large errors, the resulting waveform produced by the combination of energy saving lamps and dimmers causes pulsed currents with high peak values and short duration. The EEMs error magnitude was also influenced by the dimmer, being larger at a higher phase shift value.

In contrast with [12] and [26], authors in [83] reported significant errors in analogue meters when compared to the measurements of electronic meters. The tests consisted of disturbances injected to the load such as harmonics, unbalance and frequency changes. Three static meters versus three electromechanical meters were tested in this study. The equipment used for this experiment was a reference meter, a single-phase power quality analyser, a programmable a.c. power source, pulse counters and a three-phase 75 Ohm (per phase) resistor in wye connection. This study shows how static meters are not particularly sensitive to disturbances such as unbalance or changes in the mains fundamental frequency.

3.4.3 Performance Tests

One of the earlier experiments for electricity meters exposed to harmonic content was reported in [84]. For this test, a set of unbalanced signals was injected to different meters. The percentage error is in the range from -10.09% to +0.52%, for three-phase digital meters.

In [11], eight electronic meters for electricity revenue (three single-phase and five three-phase) were tested according to the standard EN 50470-3, but extending the frequency range up to 3 kHz. For this test, an Omicron CMC 256+ generator was employed for the voltage and current signals for the meters and an NI 9239 card was used to monitor the pulsed output of the meters. The authors concluded that even when all tested meters meet the accuracy of standards requirements, all of them had a

Chapter 3. Analysis of Static Electricity Meter Design and Reported Accuracy Errors

different performance in the presence of harmonic active power. Furthermore, two of those meters exhibit significant deviations, in the range from -100% to +300% when the harmonic frequency increases.

Two single phase energy meters were exposed to nonsinusoidal tests in [14]. A Chauviun Arnux 8834 (calibrated power quality analyzer) is used as a reference, connected in parallel with the meters under test. Three tests were performed as follows. Test 1 consisted of six 100 W tungsten lamps injected with harmonic components of 30% from the 3th to the 19th. Test 2 consisted of 15 CFL (40 W) connected to a 50 Hz sinusoidal power source. In Test 3, the 15 CFL are connected in parallel with an inductive single-phase motor. The current waveforms resulting from the described conditions of the aforementioned tests are nonsinusoidal, but they do not exhibit the characteristics known to be the cause of errors in power measurements, such as pulsed currents of short-duration, high peak values and low rms. The authors concluded that meters can acceptably measure instantaneous active power under the described conditions and only one meter presented a relative error of -3.14% under Test 3 conditions.

Thirteen experiments were performed in [15] with six electronic meters (of four different models), using a programmable power source and a reference wattmeter. The tests include the different level of harmonic content up to the 50th, phase fired control load, as well as 8 PCs with LCD monitors. For some of those tests, the error of meters is as high as 6.78%, when the PC cluster was connected.

3.4.4 Testbed and Calibration Under Nonsinusoidal Conditions Proposals

The attempts to characterize the behaviour of electricity meters under nonsinusoidal waveform conditions and to find an appropriate set of test signals (for calibration) have been described in the literature, particularly during the last two decades. Three representative examples of these attempts will be presented in this section. The characterization of electricity meters under nonsinusoidal waveform conditions is not an easy task as there is not an accepted procedure to perform calibration in nonsinusoidal conditions and the metrological traceability is challenging to attain [17]. Two major

problems which make this characterization a complex task can be identified:

- 1) finding a “representative real-world” set of nonsinusoidal test signals (possibilities are virtually infinite)
- 2) depending on their internal design (i.e. sensors, metrics definitions, etc.), electricity meters respond differently to nonsinusoidal signals.

Due to the complexity and the high number of combinations that each influencing quantity could have in real world conditions, the authors in [23] proposed a statistical approach, called optimal design of experiments (OED), in order to reduce the number of tests electricity meters need to verify their accuracy under nonsinusoidal waveform conditions. One of the main outputs of this paper is the comparison between influence quantities and the effects of their interaction.

A study presented in [76] uses theoretically developed and “real-world ” captured signals to assess the response of electricity meters. Three test signals were selected as the most stringent for the meters, and the authors observed that measurement errors strongly depend on the current crest factor and phase shift of the signal.

The occurrence probability of a particular current or voltage harmonic amplitude level to exceed a specific value in real power systems is proposed in [16] as a suitable method to ‘build’ distorted test signals. The probability of occurrence is extracted from the statistical records of real measurements on power systems as well as theoretical waveforms found in the literature. The authors recognize the need to periodically update probability threshold values as a limitation of the proposed approach.

3.5 Chapter Summary

The design of a static electricity meter can be achieved in many different ways, adopting a particular set of components, signal processing techniques, and formulas. In this chapter, a review of the advantages of some of these components and techniques has been provided, with particular focus on elements relating to fast signal changes which support later chapters of this thesis.

Chapter 3. Analysis of Static Electricity Meter Design and Reported Accuracy Errors

The power quality of the electrical grid, due to the effect of diverse emerging technologies and devices, is constantly changing the waveform conditions of voltage and current. These changes are most significant in low-voltage electrical systems, and the resulting pulsed currents of short duration are producing the largest errors in EEMs.

Most of the tests and study cases where faulty readings of electricity meters are reported in the literature do not explain possible causes of such errors. The lack of uniformity in the conditions of which those tests have been implemented, as well as the wide difference in the laboratory equipment, load characteristics, and other similar aspects has led to discordant and sometimes contradictory results among authors. However, some authors have highlighted that conducted electromagnetic interference as the main reason of SEM malfunction.

Some static meters, exposed to unlikely (but still possible) extreme operating conditions, have presented large measurement errors in the presence of nonsinusoidal waveforms with characteristics such as high crest factor and high phase shift, whereas unbalanced signals or frequency deviations, have very little contribution to the meter error.

It has been observed from the reported SEM measuring errors that isolated elements, such as the influence of harmonic content on the a.c. signals or the presence of non-linear loads in the electrical grid, are not responsible for misreadings in electricity meters by themselves, but when the combination of such elements produces a waveform with pulsed peaks of short duration along with changes in the phase shift, the error in the SEMs can be significant. Therefore, this critical fact is the basis for the work in the remaining chapters of this thesis.

Chapter 4

Energy Metering Integrated Circuit Tests and Modelling

4.1 Introduction

As demonstrated in Chapter 3, the accuracy of static electricity meters under nonsinusoidal situations, which is an important topic for both academic study and public interest [63], is not yet properly covered by the standards [25] but has been analysed from different perspectives [10, 11, 15, 78, 85–87] during the last few years. However, addressing the problem of erroneous readings on SEMs when exposed to nonsinusoidal signals is a complex task [17], where a large number of variables could affect the final measurement reported by the meter. Some of these variables which have proved to be problematic for electricity meters will be assessed in this chapter to understand the practical impact on meter accuracy.

One of the most important factors that affects the accuracy of electricity meters is the voltage or current signal shape itself, as nonsinusoidal signals could have multiple different characteristics (i.e. amplitude, frequency, harmonic content, crest factor, etc.). Thus, the number of possible signals for evaluating the response of meters outside the standards requirements is virtually infinite [13]. In this regard, the present efforts in the literature to define methods and an appropriate set of test signals for nonsinusoidal

conditions, previously revised in Chapter 3, involves statistical/probabilistic harmonic predefined content [16], mathematically defined waveforms [76], or signals with random harmonic content [79,87]. Most of these studies try to provide more realistic scenarios compared to those defined in the standards by means of including harmonic content on the voltage and current signals. Nevertheless, it has been observed that high peak currents with short transition duration produces the largest errors on SEMs [26,59–61,75,78,88] compared to the error produced by nonsinusoidal signals without such fast transients.

The design of the meter itself (described in Chapter 3) could vary significantly among manufactures, employing different sensors or transducers, ADCs, filters, and algorithms to calculate the relevant electrical quantities [25,28]. This broad flexibility for SEM design has led to a variety of measuring devices that meet accuracy requirements of applicable standards. However, the accuracy of a device is not guaranteed by the manufacturer beyond the limits prescribed by the standards, i.e. when applying a sinusoidal or quasi-sinusoidal waveform only. Moreover, applying the same nonsinusoidal signal to different standard compliant SEMs, leads to inconsistent measurements among the meters [26,61], where devices under test (DUT) could report a positive error, a negative error or an almost negligible error.

This chapter analyzes a key component of an SEM, the energy metering IC, which typically implements the metrology engine in an embedded digital signal processor. Such ICs are considered to be the heart of the majority of static electricity meters, have proven to be accurate in the presence of harmonic content [33], but it is unknown how they perform under fast-changing currents conditions. In 2009, Analog Devices, one of the biggest companies which produces such energy metering components claimed “to have supplied more than 250 million ICs for use in energy meters worldwide” [89], and this number have significantly increased since then.

In this chapter, the focus is to evaluate the performance of one commercially available, but representative, metering IC when exposed to signals with characteristics that are known to cause errors in SEMs, i.e. high signal slope and low power factor. The main objective is to identify weaknesses or limitations in the IC design which are not

possible to find under standard test conditions and analyse the factors which cause errors in energy meters. Being a fundamental component of SEMs, detailed knowledge of metering IC technology and its behaviour under certain nonsinusoidal conditions will allow useful conclusions to be drawn in order to find the root cause of error in electricity meters. In turn, this chapter will inform suitable tests for other ICs and future standards.

4.2 Experimental Tests Description

In this section, the experimental tests and the test signals are described in detail. The first step to fully understand the root cause of misreadings (and variations in reading) in electricity meters is to split the measurement system into the different elements. For example, the system could be organized in three main groups: test signal, analogue front-end, and signal processing.

The voltage and current signals applied to the meter are intended to examine the behaviour of one commercial energy metering IC, which is representative of typical meter implementations, beyond the requirements established by standards for SEM. In this regard, the proposed tests include sinusoidal waveforms, standard nonsinusoidal signals, real-world captured nonsinusoidal waveforms and synthesized signals sharing characteristics of different levels of crest factor and phase angle, which are the main causes of significant errors in electricity meters, as has been described in Chapter 3.

4.2.1 Sinusoidal Tests

The sinusoidal tests are mainly used to calibrate the system and to verify the accuracy at different values of current and phase angle. In this thesis, the term phase angle will always makes reference to the phase difference, in degrees, of the current waveform with respect to the voltage.

After calibration (see C), the phase angle between the voltage and current signal should be varied from 0 to 360° in steps of 15°, at nominal values I_{ref} and U_n , in order to evaluate the accuracy of the measurements at different power factors.

4.2.2 Standard nonsinusoidal Tests

The standard nonsinusoidal tests with waveforms presented in Figure 4.1 includes the test prescribed in EN 50470-3-2006 standard [44] (and described in 2.3.2.3) for testing the accuracy of electric energy meters in the presence of harmonics (40% I_{5th} and 10% V_{5th} , in phase), a variation of this test called “Harm Q” described in [33] (I_{5th} and V_{5th} 90° shifted), and the “Quadriform” and “Peaked” tests described in the OIML R 46 document [21].

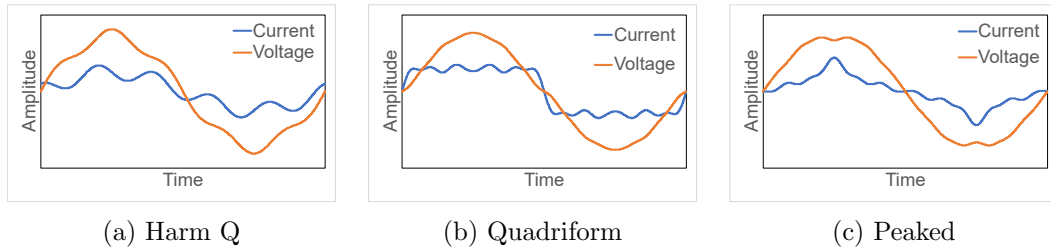


Figure 4.1: Standard nonsinusoidal tests waveforms.

Through the standard nonsinusoidal tests, the ability of the IC to accurately measure electrical quantities in the presence of different harmonic content and different harmonic power factor is evaluated.

4.2.3 Real-world Current Signal Tests

Three real-world nonsinusoidal current waveforms representing household commonly used electronic equipment have been selected for testing the IC. The signals corresponds to the current drawn by a compact fluorescent lamp, a modern entertainment system and a switched-mode power supply. The waveforms (Figure 4.2), obtained from the equipment hArmoNic Database (PANDA) [27], the EPRI library of harmonic spectra [90] and the NPL power quality waveform library [91], respectively, were selected due to their nonsinusoidal shape caused by internal nonlinear components such as power electronic switching devices.

The voltage signals where obtained by means of applying the nonsinusoidal waveform and a sine waveform to a simulated pure resistive impedance of 0.1 Ω , in order to include the effect of nonsinusoidal currents in the voltage waveform. Different resistive

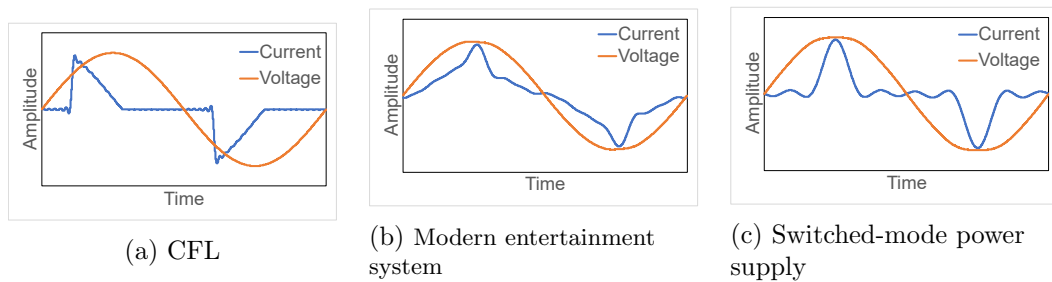


Figure 4.2: Real-world current signal tests waveforms.

values emulating the line impedance at the metering point have been tested with negligible effects in the accuracy of the IC, compared to using a perfect sinusoidal signal for the voltage channel.

4.2.4 Crest Factor Tests

The waveforms applied to electricity meters in recent studies where significant errors have been reported [26, 59–61, 88] share some similarities: distorted current signals with high peak values and short transition duration. In such studies, the waveforms were produced by dimmers or similar power electronics components used to control the power output of an electric appliance such as a water pump, a motor or a lamp. The crest factor is defined as the ratio of the signal peak value to the rms value and it is a useful metric to identify signals with high peak amplitude and low rms which are known to produce errors in SEMs. In this thesis, the term crest factor will always refer to the current crest factor as in (equation 2.28).

Depending on the power electronic design [92, 93], the line impedance [75] and the type of load [86], different current waveforms may be produced, including signals with high crest factor values. In an effort to replicate the characteristics of such signals, for the crest factor tests, a perfect sine waveform is “chopped”, leaving only portions of the waveform. This waveform “chopping” technique tries to replicate the resulting current signal produced by the effect of selecting different firing-angle values in a dimming device and was employed in one of the most recent studies related to the analysis of the error causes in electricity meters exposed to pulsed currents [94]. By this novel approach, the focus is moved from the harmonic (or subharmonic) signal content to

the I_{rms} , i_{peak} and transition duration values. The reason to take this approach is that metering ICs have been proven to be accurate in the presence of harmonic content [33], as will be seen later in the results section, but it is unknown how the metering ICs cope with fast-changing currents.

The proposed current waveforms retain only part of the original sinusoidal waveform, similar to the waveforms drawn by switching non-linear loads (e.g. motor power drive systems or energy saving lamps), while the “removed” portion is kept to zero value as can be seen in Figure 4.3. Two cases are considered: “leading” where the current is applied at the start of each half-cycle, and “falling” where the current is applied at the end of each half-cycle. Authors in [94] recently used a similar technique to evaluate the difference in measurement errors produced by equal rising and falling time of pulsed currents injected to meters under test. Figure 4.3 illustrates tests signals for 1/2, 1/4, 1/8 and 1/16 sub-cycle portions. This is designed to closely emulate the behavior of actual fast-changing current waveforms, but in a way that can be controlled and mathematically analysed.

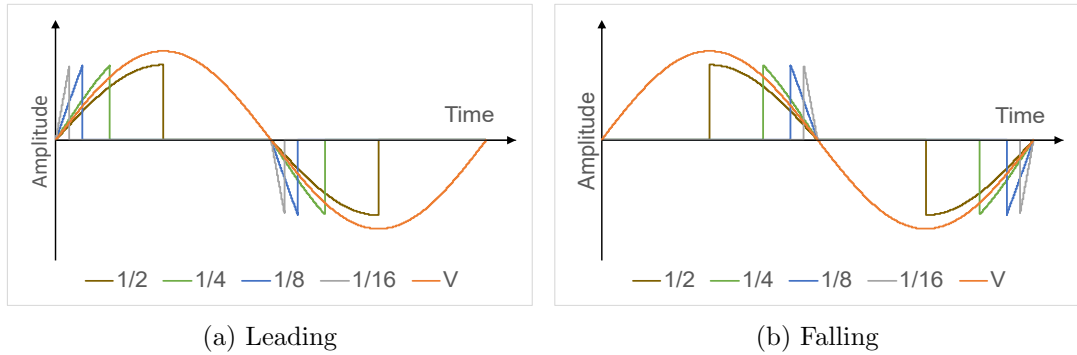


Figure 4.3: Crest factor tests waveforms.

Crest Factor “leading” and “falling” waveforms one-cycle generic equation are described in 4.1 and 4.2, respectively as:

$$y(t)_x = \begin{cases} A \sin(\omega t) & 0 \leq t < x\pi \\ 0 & x\pi \leq t < \pi \\ A \sin(\omega t) & \pi \leq t < (x+1)\pi \\ 0 & (x+1)\pi \leq t < 2\pi \end{cases} \quad (4.1)$$

and

$$y(t)_x = \begin{cases} 0 & 0 \leq t < (1-x)\pi \\ A \sin(\omega t) & (1-x)\pi \leq t < \pi \\ 0 & \pi \leq t < (2-x)\pi \\ A \sin(\omega t) & (2-x)\pi \leq t < 2\pi \end{cases} \quad (4.2)$$

where:

ω is the angular frequency $2\pi f$ (degrees)

f is the power system frequency (Hz)

t is the time (s)

x is the sub-cycle portion of non-zero value (i.e. 1/2, 1/4, 1/8 or 1/16)

The characteristics of the signals have been scaled to reach similar i_{peak} values, which can be seen in Table 4.1. Parameters from sinusoidal and real-world tests waveforms have been included for comparison. The transition duration, formerly known as “rising” or “falling” time, is defined as the time difference between the 10% to the 90% of the transition amplitude [95] and can be controlled by means of selecting different x values (equations 4.1 and 4.2), where the x magnitude is directly proportional to the transition duration. Appendix D provides illustrations and definitions of some terms from Table 4.1.

Although the proposed crest factor test waveforms may seem unrealistic, the recent literature [10, 12, 19, 59–61, 75, 94, 96, 97] has revealed nonsinusoidal signals recorded in real-world power systems which share similarities such as the step-like shape of high peak amplitude and short time duration. Moreover, such recorded signals present in many cases a shorter transition duration (rising time) compared to the values presented in Table 4.1. Despite the aforementioned studies not explicitly reporting the transition duration (rising time) of employed current signals, the authors in [75] found that current signals of rising slopes between 2 and 150 μs results in static meter errors. Appendix E provides a gallery of step-like current waveforms obtained in real-world measurements or mathematically defined [94, 96] which were used in accuracy SEMs testing.

4.3 Measurement System Description

This section describes the measurement system setup used for the calibration and the accuracy tests of the metering IC, performed under sinusoidal and nonsinusoidal conditions. The experimental setup (Figure 4.4) is composed of a Rigol DG952 [98] two-channel arbitrary waveform generator (AWG), EVAL-ADE7878AEBZ energy metering IC evaluation board, a Raspberry Pi (RPI) board and a personal computer (PC). The (AWG) specifications are provided in Table 4.2 and the EVAL-ADE7878AEBZ board characteristics are later described in the sub-section 4.3.2.

Table 4.2: Rigol DG952 AWG specifications.

| Model | DG952 |
|----------------|--------------|
| Channel | 2 |
| Max. frequency | 50 MHz |
| Sample rate | 250 MSa/s |
| Resolution | 16 bits |

In this study, the focus is to evaluate the performance and the accuracy of the energy metering IC itself. For this reason, voltage and current sensors are not included as they are known to be the most significant sources of uncertainty in digital measuring instruments [17]. Instead, ideal current transformer and voltage transformer output signals

Table 4.1: Test waveforms parameters.

| Signal | I_{rms} (A) | i_{peak} (A) | CF | Transition duration (ms) | Transition (A) | Slope (A/ms) | PF | THD _I |
|----------|------------------|-------------------|------|-----------------------------|-------------------|-----------------|-------|------------------|
| Sine | 20.00 | 28.28 | 1.41 | 3.32 | 22.63 | 6.98 | 1 | 0.00 |
| CFL | 10.07 | 28.28 | 2.81 | 0.26 | 25.00 | 96.16 | 0.609 | 0.94 |
| Modern | 12.55 | 28.20 | 2.25 | 3.99 | 25.12 | 6.29 | 0.936 | 0.36 |
| Switched | 10.56 | 28.31 | 2.68 | 1.31 | 25.60 | 19.47 | 0.667 | 1.07 |
| 1/2 | 14.14 | 28.28 | 2.00 | 3.24 | 22.63 | 6.98 | 0.688 | 0.62 |
| 1/4 | 8.44 | 28.00 | 3.32 | 1.97 | 22.40 | 11.37 | 0.281 | 1.26 |
| 1/8 | 5.80 | 28.11 | 4.84 | 0.99 | 22.51 | 22.57 | 0.097 | 2.02 |
| 1/16 | 4.00 | 27.55 | 6.91 | 0.49 | 22.03 | 44.13 | 0.029 | 3.02 |

are emulated by the AWG. The “phantom-loading” technique (i.e. using independent signals for voltage and current, rather than an actual load) has been implemented to avoid measuring errors introduced by transducers and to achieve a better control of the voltage and the current waveforms.

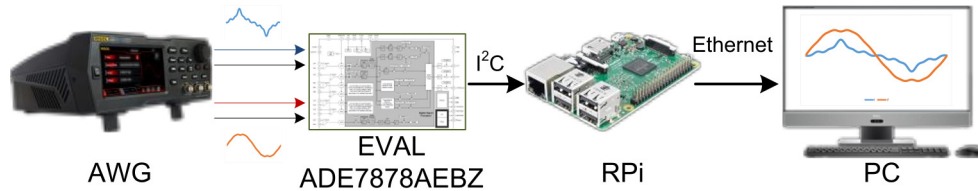


Figure 4.4: Experimental setup.

To inject the test system with data, the voltage and current signals are generated in a custom made LabVIEW application, where the theoretical electrical quantities are calculated. To generate the resulting waveforms, the LabVIEW application needs to manually input the individual harmonic components signal parameters, i.e. harmonic order, amplitude, phase and sampling rate (please see Figure 4.5). Once all the parameters are configured by the user and the ‘Run’ button is clicked, the theoretical electrical quantities are calculated and displayed along with the resulting waveform. The 16384¹ points per cycle signals are exported as comma-separated values (csv) files by the LabVIEW application and then uploaded to the AWG. The voltage and current signals are generated simultaneously and independently by the AWG with a sampling rate of 819.2 kSa/s and 16-bit of resolution.

A Raspberry Pi 3 Model B+ board, with specifications given in Table 4.3, is used as the interface between the metering IC mounted on the EVAL-ADE7878AEBZ evaluation board and a LabVIEW application running on a personal computer. The RPi was selected to be used as the external controller for the EVAL-ADE7878AEBZ board, because of its availability and compatibility with both the evaluation board and LabVIEW software. Through the RPi, it is possible to access any register inside the IC for read and write operations and its functionality was verified during the calibration procedure. This capability to read and write directly from the metering IC’s registers

¹16384 data points per cycle are needed to create a 50 Hz signal sampled at 819.2 kSa/s

allows analysis of how calculations are performed by the different internal blocks of the IC instead of relying only on the final result (e.g. total active energy). The LabVIEW application displays and collects the data obtained during the tests, performs additional calculations, and accumulates the energy measurements over a defined period of time.

Table 4.3: Raspberry 3 Model B+ specifications.

| | |
|-------------|--|
| Processor | Broadcom BCM2837B0, Cortex-A53 64-bit SoC @ 1.4GHz |
| Memory | 1GB LPDDR2 SDRAM |
| Conectivity | Gigabit Ethernet over USB 2.0 (maximum throughput 300Mbps) |
| Access | Extended 40-pin GPIO header |

The process to obtain the measurements from the evaluation board to the RPi and consequently, the PC, can be observed in the flow chart in Figure 4.6. This consists of first initializing the ADE7878A IC by means of writing to some configuration registers. During this stage, gain and offset compensation is performed for instantaneous and rms voltage and current measurements, and also for powers and energies measurements. Then, the internal ADE7878A measurement registers are read and a calibration factor is applied. After a hundred readings are performed in one second, the measurements are averaged, added to a .csv file and displayed in a graph. This process is running continuously until the STOP button is clicked.

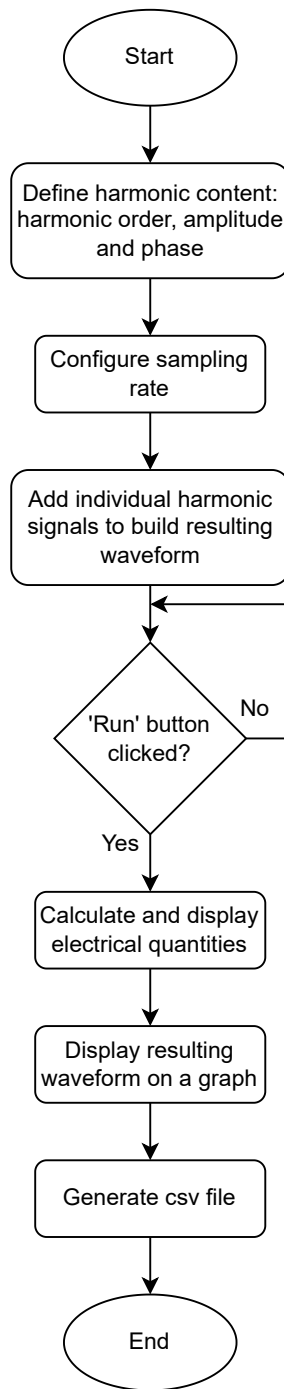


Figure 4.5: Signal generator LabVIEW application flow chart.

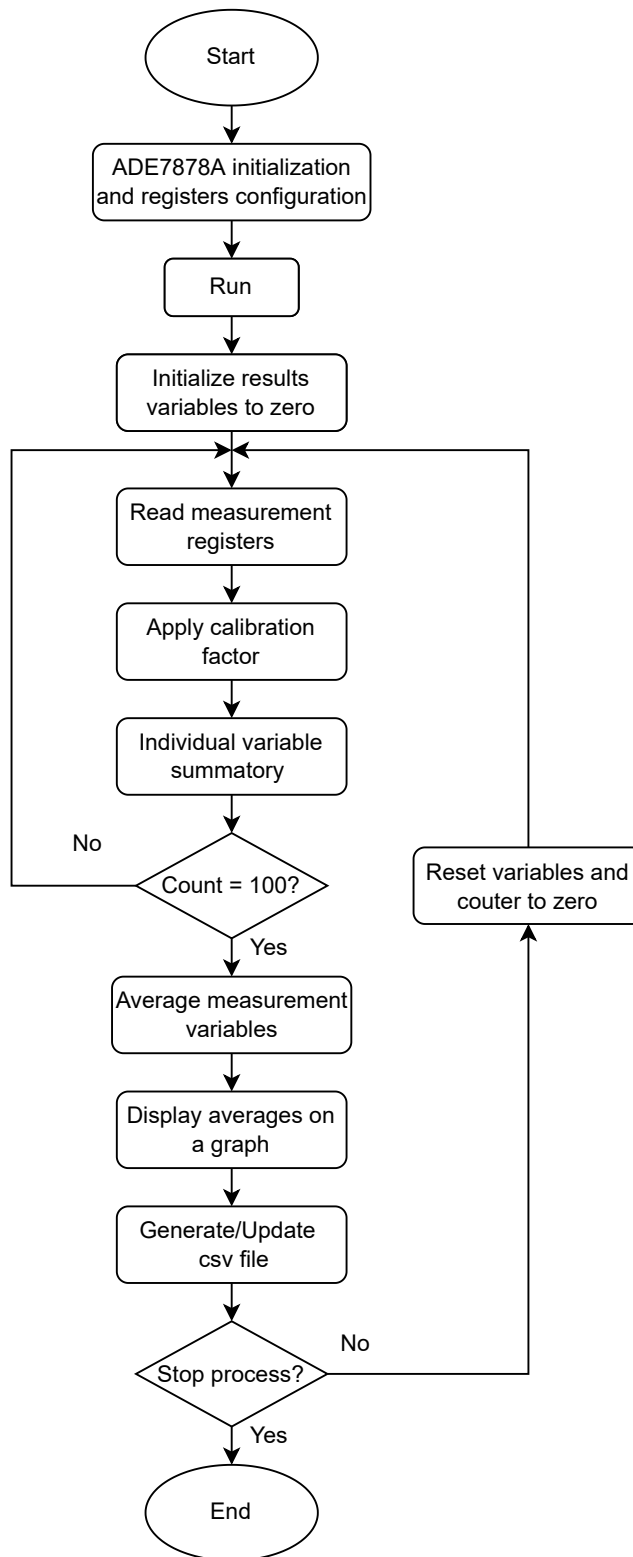


Figure 4.6: ADE7878AEBZ board and LabVIEW interface application flow chart.

4.3.1 Electrical Current and Voltage Level Definitions

According to the IEC 62052-11:2003 [2] and EN 50470-1:2006 [43] standards, the voltage and current reference values in Table 4.4 are defined. The voltage and current values defined in Table 4.4 are scaled to map to the range of the internal ADCs (i.e. ± 500 mV peak, which represents I_{max}).

Table 4.4: Definitions of meter quantities.

| Name | Symbol | Value | AWG output |
|----------------------|-----------|-------|------------|
| Starting current | I_{st} | 0.1 A | 1 mVpp |
| Minimum current | I_{min} | 1 A | 10 mVpp |
| Transitional current | I_{tr} | 2 A | 20 mVpp |
| Reference current | I_{ref} | 20 A | 200 mVpp |
| Maximum current | I_{max} | 100 A | 1000 mVpp |
| Reference Voltage | U_n | 230 V | 590 mVpp |
| Reference frequency | f | 50 Hz | -- |

4.3.2 Electricity Meter Design

The EVAL-ADE7878AEBZ board includes components required for a typical static electricity meter analogue front-end such as anti-aliasing filters, resistive voltage dividers, energy metering IC and digital isolators (Figure 4.7).

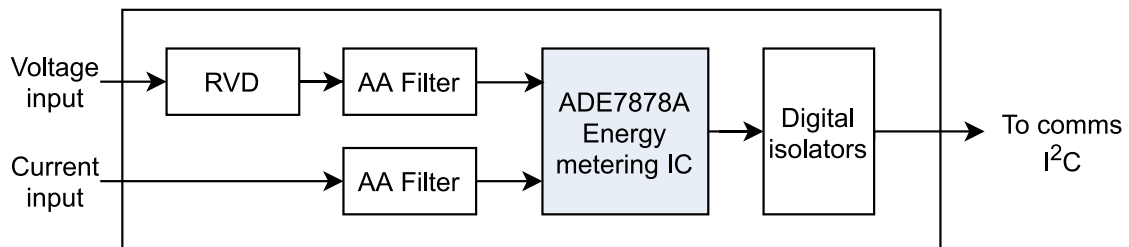


Figure 4.7: EVAL-ADE7878AEBZ evaluation board simplified diagram.

The EVAL-ADE7878AEBZ board is configured as follows:

- the resistive voltage divider (attenuation) has been removed from the voltage input path;
- AA filter corner frequency = 7.2 kHz;

- high-pass filters (HPF) enabled (to remove d.c. signal components, see Figure 3.5);
- Raspberry Pi board set as an external microcontroller managing the ADE7878A [64].

4.3.2.1 ADE7878A Energy Metering IC

The ADE7878A is a poly-phase energy metering IC with per-phase total and fundamental active and reactive power calculation capabilities. It was released in February 2010 as the flagship of a new generation of Analog Devices metering ICs [89]. Although it is a three-phase metering IC, all the tests carried out use only a single-phase for simplicity. This does not affect results for evaluating the accuracy, as a three-phase meter is composed by three identical single-phase circuits [19, 73]. The ADE7878A single-phase functional block diagram can be seen in Figure 3.5.

The ADE7878A has second-order sigma-delta ($\Sigma - \Delta$) ADCs with specifications given in Table 4.5.

Table 4.5: ADE7878A ADC's specifications.

| Parameter | Specification |
|----------------|--------------------|
| Bandwidth | 4 kHz |
| Sampling rate* | 1.024 MHz |
| SNR | 55 dB |
| Input range | ± 500 mV peak |
| Impedance (DC) | 400 k Ω min |
| Offset error | ± 25 mV max |
| Gain error | ± 4 % |

* Oversampling rate. The ADC outputs at 8 kSps.

For all the tests are carried out, the LabVIEW application accesses the IC internal registers through the RPi, using I²C communication protocol, to read the quantities listed on Table 4.6. Additionally, the IC includes waveform sample registers which can be accessed through the High Speed Data Capture (HSDC) communication protocol to acquire the waveforms directly as has been digitized by the ADC. Some quantities, crest factor and power factor, are not directly available from the IC registers, but they are calculated from the I_{rms} , i_{peak} , P and S registers.

Table 4.6: ADE7878A measurements.

| Symbol | Description | Unit |
|------------|-----------------------------|---------|
| V_{rms} | rms voltage | V |
| I_{rms} | rms current | A |
| f | line frequency | Hz |
| θ | phase angle | Degrees |
| i_{peak} | peak current | A |
| CF | crest factor * | |
| P | total active power | W |
| S | apparent power | VA |
| Q | total reactive power | var |
| PF | power factor * | |
| E | total active energy | Whr |
| E_S | apparent energy | VAhr |
| E_Q | total reactive energy | varhr |
| E_1 | fundamental active energy | Whr |
| E_{Q_1} | fundamental reactive energy | varhr |

* Calculated from ADE7878A registers

4.3.2.2 ADE7878A Metrics

The ADE7878A energy metering IC performs calculations for the electrical quantities listed on Table 4.6 from the voltage and current inputs (Figure 4.7) as follows:

rms values

Figure 4.8 shows how rms values are calculated by the ADE7878A IC. The same procedure is used for voltage and current signals. First, the instantaneous values of the signal are squared and then filtered by a low-pass filter (LPF). After being filtered, the root square of the signal is obtained and offset compensation (xIRMS block in Figure 4.8) may be applied.

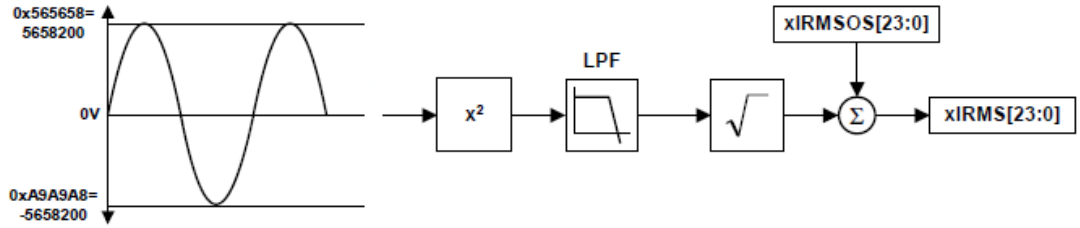


Figure 4.8: ADE7878A rms signal processing.

ADE7878A rms calculation involves squaring the time sampled signals, taking the average and then obtaining the square root:

$$I_{rms} = \sqrt{\frac{1}{N} \sum_{N=1}^N I^2[n]} \quad (4.3)$$

Equation 4.3 contains the contributions of all harmonics and not only the fundamental current (or voltage) and can be expressed as:

$$i(t) = \sum_{k=1}^{\infty} I_k^2 \sqrt{2} \sin(k\omega t + \gamma_k) \quad (4.4)$$

where

$i(t)$ is the instantaneous value of the current (or voltage) signal of k order,

I_k (or V_k) is the rms value of each current (or voltage) harmonic,

k is the harmonic order,

ω is the angular frequency and

γ_k is the phase angle of harmonic signal of k order.

The square of $i(t)$ is

$$\begin{aligned}
 i^2(t) = & \sum_{k=1}^{\infty} I_k^2 - \sum_{k=1}^{\infty} I_k^2 \cos(2k\omega t + 2\gamma_k) + 2\sqrt{2} \sin(k\omega t + \gamma_k) \\
 & + 2 \sum_{k,m=1}^{\infty} 2 \times F_k \times F_m \sin(k\omega t + \gamma_k) \times \sin(m\omega t + \gamma_m)
 \end{aligned} \tag{4.5}$$

After the signal has been filtered by the LPF and the execution of the square root, the formula implemented by the ADE7878A to calculate rms values, as reported in the data-sheet, can be expressed as follows:

$$I_{rms} = \sqrt{\sum_{k=1}^{\infty} I_k^2} \tag{4.6}$$

Current peak value

i_{peak} represents the absolute value of the highest peak amplitude detected by the IC over ten half cycles, from the current input signal. The ten half cycles is a fixed parameter in the ADE7878A which works well in real-world situations and can not be changed, but in controlled lab testing conditions it is possible to select a reduced number of half cycles to estimate the peak current value.

Phase angle

The ADE7878A measures the time delay between the low-pass filtered voltage and current signals, using as start and stop measuring points, the signals negative to positive transition identified by an internal zero-crossing detection circuit, as can be seen in Figure 4.9.

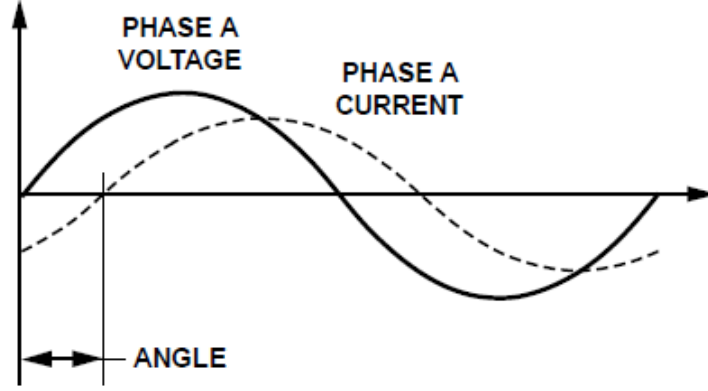


Figure 4.9: ADE7878A phase angle calculation: measured time delay between voltage and current signals [73].

Total active power

To calculate the total active power P , the ADE7878A considers both, fundamental and harmonic components of the voltage and current signals which can be expressed as

$$v(t) = \sum_{k=1}^{\infty} V_k \sqrt{2} \sin(k\omega t + \phi_k) \quad (4.7)$$

$$i(t) = \sum_{k=1}^{\infty} I_k \sqrt{2} \sin(k\omega t + \gamma_k) \quad (4.8)$$

where V_k and I_k are the rms values of each voltage and current harmonics; ϕ_k and γ_k are the phase delays of each harmonic.

Then, the instantaneous power is the product of instantaneous voltage and current signals as in 4.9

$$p(t) = v(t) \times i(t) = \sum_{k=1}^{\infty} V_k I_k \cos(\phi_k - \gamma_k) - \sum_{k=1}^{\infty} V_k I_k \cos(2k\omega t + \phi_k + \gamma_k) + \sum_{k,m=1}^{\infty} V_k I_k \cos[(k-m)\omega t + \phi_k - \gamma_m] - \cos[(k+m)\omega t + \phi_k + \gamma_m] \quad (4.9)$$

Finally, the average power over an integral number of line cycles (n) calculated by

the ADE7878A is given in formula (4.10)

$$P = \frac{1}{nT} \int_0^{nT} p(t) dt = \sum_{k=1}^{\infty} V_k I_k \cos(\phi_k - \gamma_k) \quad (4.10)$$

where:

T is the line cycle period and P is the total active power. Note that the total active power is equal to the dc component of the instantaneous power signal $p(t)$ in equation 4.9, that is $\sum_{k=1}^{\infty} V_k I_k \cos(\phi_k - \gamma_k)$ which is used by the ADE7878A to calculate the total active power for each phase [73].

Total reactive power

The ADE7878A implements the Budeanu definition to calculate the total reactive power Q . This definition integrates both fundamental and harmonic components of the voltage and current signals, i.e. the IC nets VARs (reactive Volt-Ampere) at different frequencies. Moreover, the datasheet of the ADE7878A states that “Reactive power is defined as the product of the voltage and current waveforms when all harmonic components of one of these signals are phase shifted by 90° ” [73].

The instantaneous reactive power can be expressed as

$$q(t) = v(t) \times i'(t) \quad (4.11)$$

where $i'(t)$ is the instantaneous current waveform with all harmonic components phase shifted by 90° as

$$i'(t) = \sum_{k=1}^{\infty} I_k \sqrt{2} \sin\left(k\omega t + \gamma_k + \frac{\pi}{2}\right) \quad (4.12)$$

$q(t)$ can be rewritten as

$$q(t) = \sum_{k=1}^{\infty} V_k I_k \left\{ \cos \left(\phi_k - \gamma_k - \frac{\pi}{2} \right) - \cos \left(2k\omega t + \phi_k + \gamma_k + \frac{\pi}{2} \right) \right\} + \sum_{k,m=1}^{\infty} V_k I_k \left\{ \cos \left[(k-m)\omega t + \phi_k - \gamma_k - \frac{\pi}{2} \right] - \cos \left[(k+m)\omega t + \phi_k + \gamma_k + \frac{\pi}{2} \right] \right\} \quad (4.13)$$

Finally, the average total reactive power over an integral number of line cycles (n) calculated by the ADE7878A is given in formula (4.14)

$$Q = \frac{1}{nT} \int_0^{nT} q(t) dt = \sum_{k=1}^{\infty} V_k I_k \cos \left(\phi_k - \gamma_k - \frac{\pi}{2} \right) \quad (4.14)$$

$$Q = \sum_{k=1}^{\infty} V_k I_k \sin(\phi_k - \gamma_k)$$

where:

T is the line cycle period and Q is the total reactive power. Note that the total reactive power is equal to the dc component of the instantaneous reactive power signal in equation 4.13, that is $\sum_{k=1}^{\infty} V_k I_k \sin(\phi_k - \gamma_k)$ which is used by the ADE7878A to calculate the total reactive power for each phase [73].

Total apparent power

The total apparent power S is calculated multiplying voltage and current rms values:

$$S = V_{rms} \times I_{rms} \quad (4.15)$$

Total active energy

The total active energy is defined as the integral of the active power, expressed as:

$$E = \int_t^{nT} p(t) dt = nT \sum_{k=1}^{\infty} V_k I_k \cos(\phi_k - \gamma_k) \quad (4.16)$$

where:

nT is the accumulation time equal to 100 half line cycles. The ADE7878A achieves the integration of the active power signal in two stages. First, the instantaneous total active power accumulates in an internal register named accumulator (see figure 4.10). Then, upon reaching a threshold introduced by the user, a pulse is generated at the processor port, and the threshold (WTHR in Figure 4.10) is subtracted from the internal register. A second stage occurs outside the DSP and consists of accumulating the pulses into internal 32-bit registers, which could be accessed to obtain the energy calculation (AWATTHR in Figure 4.10). The ADE7878A instantaneous total active power calculations are reported and accumulated into an internal register each $125\mu\text{s}$ (i.e. 8 kHz), according to the datasheet and can not be modified. The total error in the ADE7878A energy calculation is less than 0.1%, as per the datasheet [73], and thus, the error introduced by the fixed time interval of $125\mu\text{s}$ is neglected.

Fundamental active energy

The fundamental active energy is defined as the integral of the fundamental power, expressed as:

$$E_1 = \int_t^{nT} p_1(t)dt = nT \sum_{k=1}^{\infty} V_1 I_1 \cos(\phi_1) \quad (4.17)$$

To calculate the fundamental active energy, the ADE7878A uses the same two-step approach described in subsection 4.3.2.2, accumulating instantaneous fundamental active power measurements into an internal register.

Total apparent energy

The total apparent energy is defined as the integral of the apparent power, expressed as:

$$E_S = \int_t^{nT} S(t)dt = \lim_{T \rightarrow 0} \left\{ \sum_{n=0}^{\infty} s(nT) \times T \right\} \quad (4.18)$$

where:

nT is the accumulation time equal to 100 half line cycles.

To calculate the total apparent energy, the ADE7878A uses a very similar procedure to calculate the total active energy. The calculation block diagram could be consulted on Figure 4.11.

Total reactive energy

The total reactive energy is defined as the integral of the total reactive power, expressed as:

$$E_Q = \int_t^{nT} q(t)dt = \lim_{T \rightarrow 0} \left\{ \sum_{n=0}^{\infty} q(nT) \times T \right\} \quad (4.19)$$

where:

nT is the accumulation time equal to 100 half line cycles.

To calculate the total reactive energy, the ADE7878A uses the same two-step approach described in subsection 4.3.2.2, accumulating instantaneous total reactive power measurements into an internal register. The total reactive energy calculation block diagram could be consulted on Figure 4.12.

Fundamental reactive energy

The fundamental reactive energy is defined as the integral of the fundamental reactive power, expressed as:

$$E_{Q1} = \int_t^{nT} q_1(t)dt = nT \sum_{k=1}^{\infty} V_1 I_1 \sin(\phi_1) \quad (4.20)$$

To calculate the fundamental reactive energy, the ADE7878A uses the same two-step approach described in subsection 4.3.2.2, accumulating instantaneous fundamental reactive power measurements into an internal register.

Although the majority of theoretical equations presented in this section indicates a summation of infinite harmonic current or voltage components as per the data-sheet, in practice, the number of harmonics is limited by the ADE7878A bandwidth of 4 kHz.

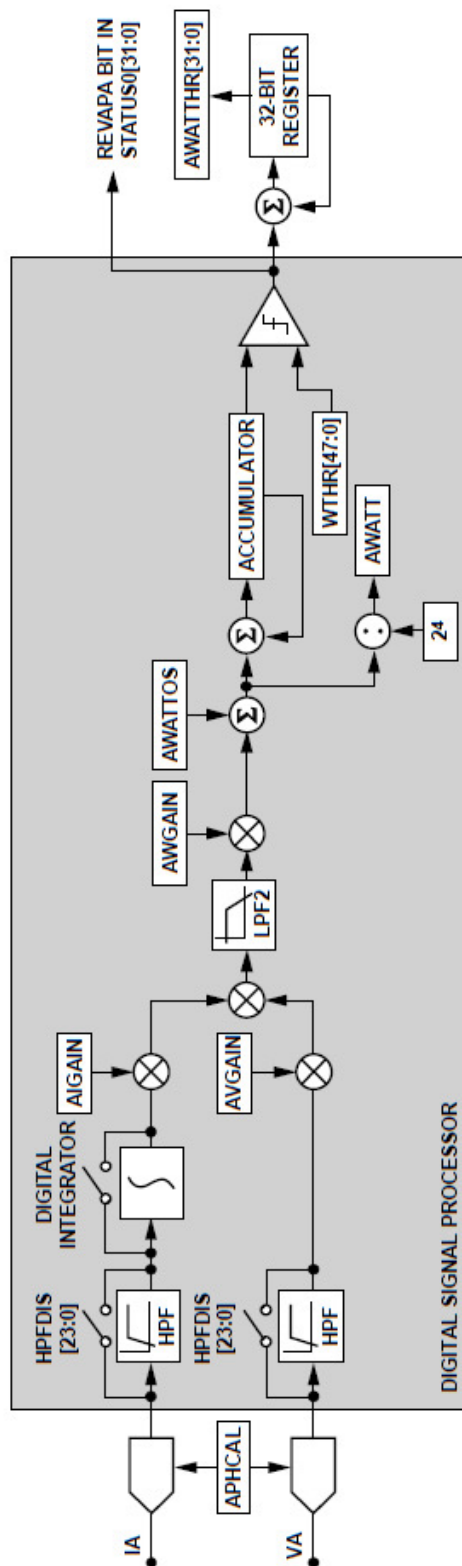


Figure 4.10: ADE7878A IC model total active energy calculation block diagram [73].

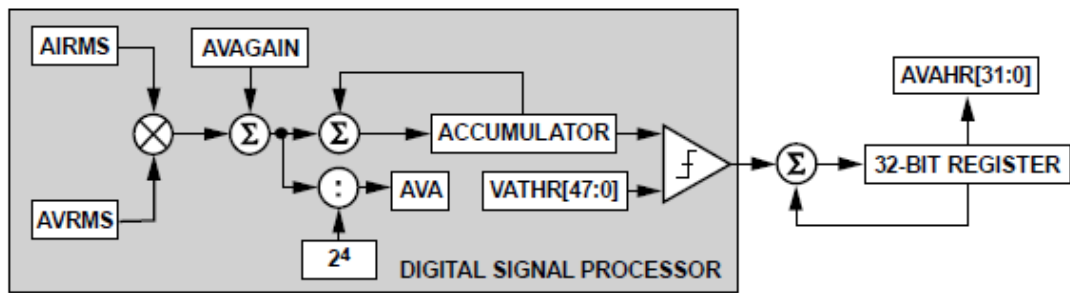


Figure 4.11: ADE7878A IC model total apparent energy calculation block diagram [73].

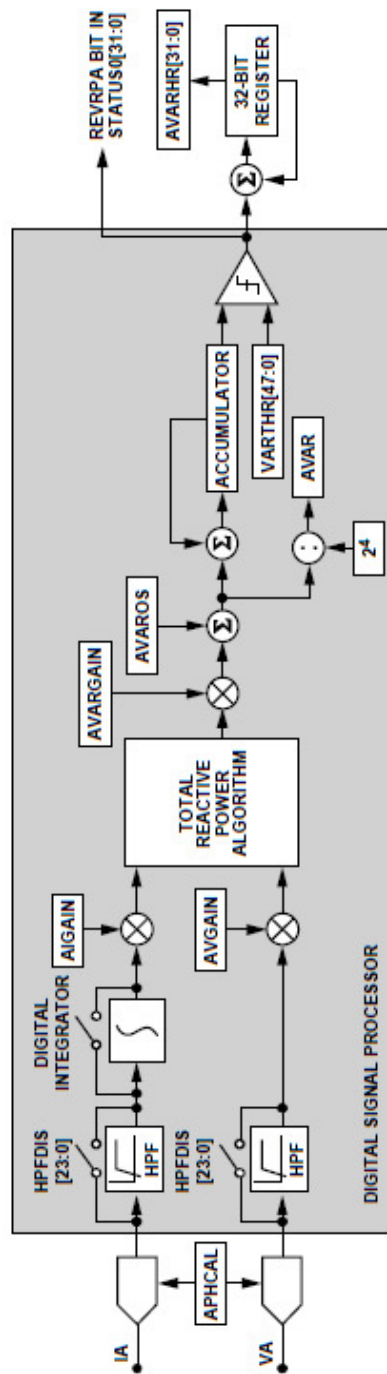


Figure 4.12: ADE7878A IC model total reactive energy calculation block diagram [73].

4.4 ADE7878A Model

To effectively identify signal parameters which cause error in metering ICs, it is important to evaluate the IC response to waveforms with different characteristics (e.g. perfect sine, fast amplitude changing signals, multiple zero-crossing points, etc.). For this purpose, the ADE7878A metering IC has been modelled for the first time in LabVIEW as a useful tool to help understanding the behaviour of the different IC's internal digital components when exposed to conditions beyond the standard requirements. This section describes the ADE7878A model features and its limitations.

4.4.1 ADE7878A Model Requirements

For this study, only the metrological section of the ADE7878A is required to be modelled and other features such as communications have been omitted. The following considerations should be taken to realistically model the metering IC:

- The ADE7878A is a three-phase metering IC composed by three identical and independent single-phase metering sub-systems. For the sake of simplicity and to meet the objectives of this study, the model should be elaborated as a single-phase metering system.
- Input waveforms for the voltage channel must be a representation of VT or RVD transducers voltage output in the range of ± 500 mV peak.
- Input waveforms for the current channel must be a representation of CT or shunt resistor transducers voltage output in the range of ± 500 mV peak.
- Input data for the voltage and current channels should contain at least five cycles to guarantee a stable response of digital filters implemented in this model.

4.4.2 ADE7878A Model Implementation

Following the requirements of the subsection 4.4.1, the ADE7878A functional block diagram from Figure 4.13 has been modelled implementing the formulas to calculate electrical parameters and the techniques to estimate phase angle and peak current

presented in Section 4.3.2.2 which are fully described in the IC's documentation [73]. Additional parameters θ_1 , V_{1RMS} , I_{1RMS} , P_1 and Q_1 , included in the model, have been calculated according to IEEE 1459-2010 [20]. The model has been implemented in LabVIEW software [99].

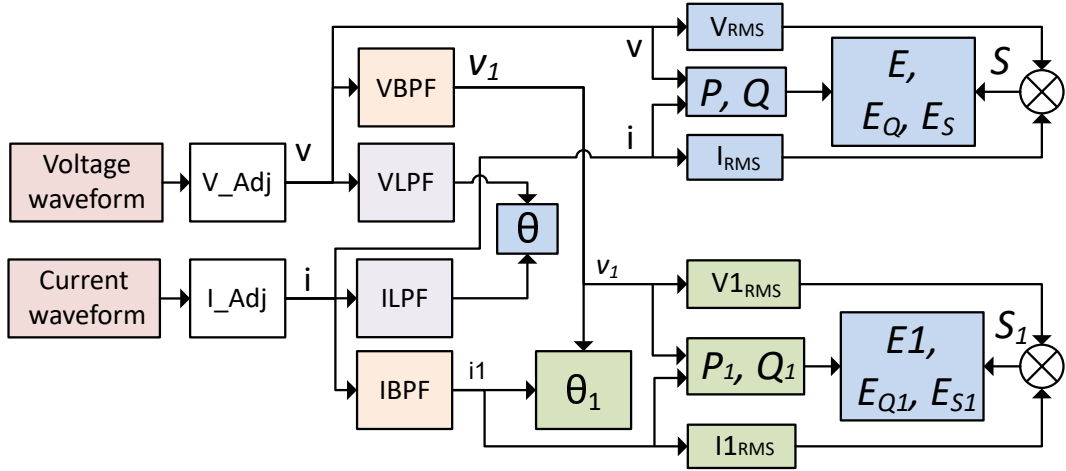


Figure 4.13: ADE7878A IC model functional block diagram (single-phase).

where:

V_Adj is the voltage waveform scaling factor

I_Adj is the current waveform scaling factor

VBPF is the band-pass filter for the voltage channel

VLPF is the low-pass filter for the voltage channel

IBPF is the band-pass filter for the current channel

ILPF is the low-pass filter for the current channel

θ is the phase angle of the current signal with respect to the voltage signal

V_{RMS} is the voltage signal rms value

I_{RMS} is the current signal rms value

P is the total active power

Q is the total reactive power

E is the total active energy

E_Q is the total reactive energy

E_S is the total apparent energy

The blue blocks from Figure 4.13 represent electrical parameters calculated and reported by the ADE7878A (see table 4.6) whereas green blocks represent electrical quantities from the fundamental frequency component which are not available from the IC registers. For example, θ_1 (green box) is the phase angle between the fundamental voltage and current components at 50 Hz, whereas θ (blue box) is the phase angle between the voltage and current signals which contains fundamental and harmonic components from any waveform. The white boxes V_Adj and I_Adj are included to scale waveform parameters to match real-world electrical typical values (e.g. 230 V, 10 A, 1000 W, etc.).

The orange boxes in Figure 4.13 represent band-pass filters used to extract the waveform fundamental components (50 Hz) for the voltage and current channels, as it is performed by the real IC.

4.4.3 ADE7878A Model Operation

To test the accuracy of the model calculations compared to the IC measurements, the sinusoidal and nonsinusoidal test waveforms described in 4.2 has been injected to the model as inputs. In Figure 4.14, the IC LabVIEW model front-panel is displaying the “Switched-mode power supply” test waveform as an operation example. The front panel is the graphical user interface (GUI) and it contains controls to input voltage and current data files as well as graphs and numerical indicators to display calculation results.

The full ADE7878A LabVIEW’s model block diagram is presented in Figure 4.15.

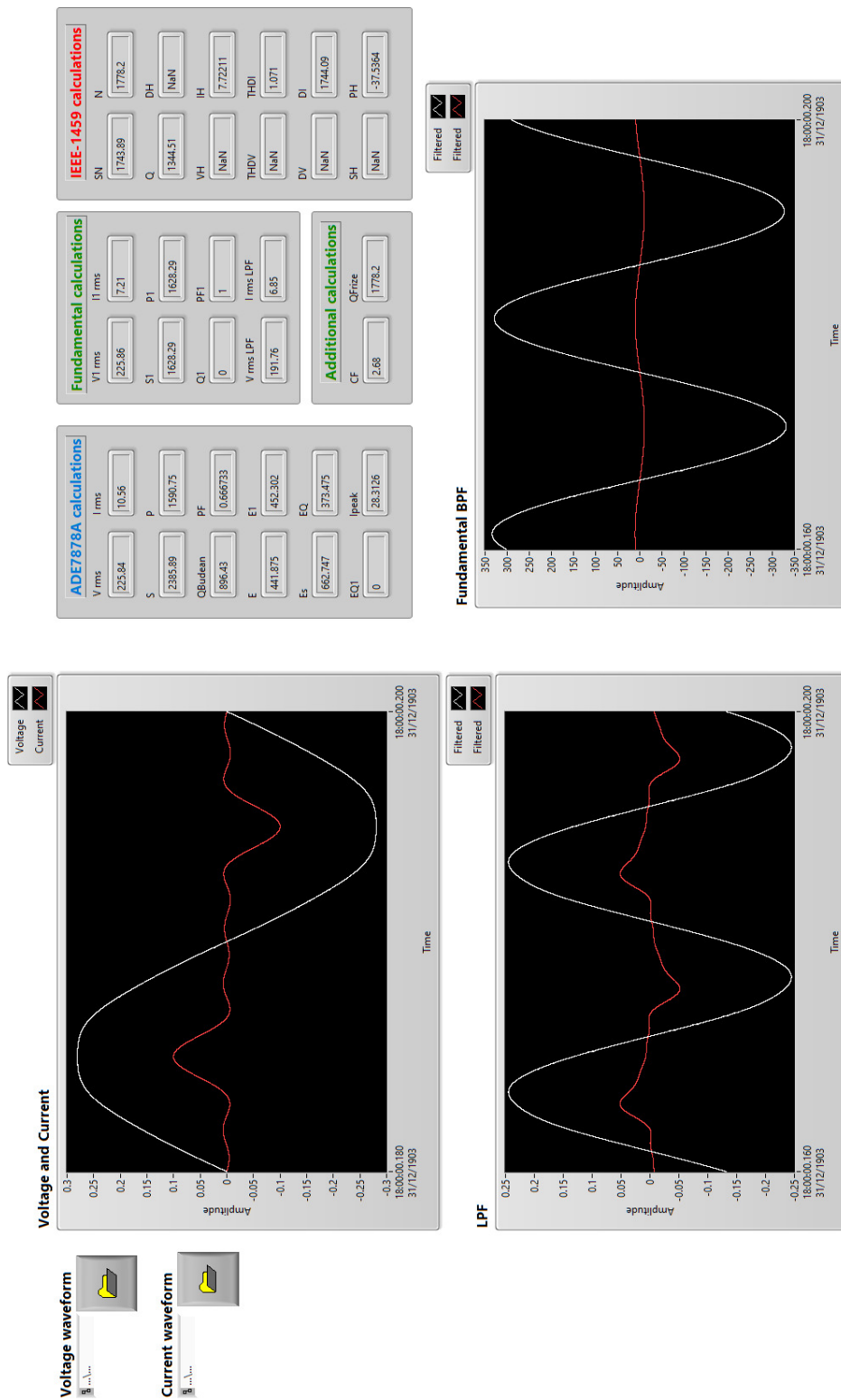


Figure 4.14: ADE7878A IC model graphical user interface.

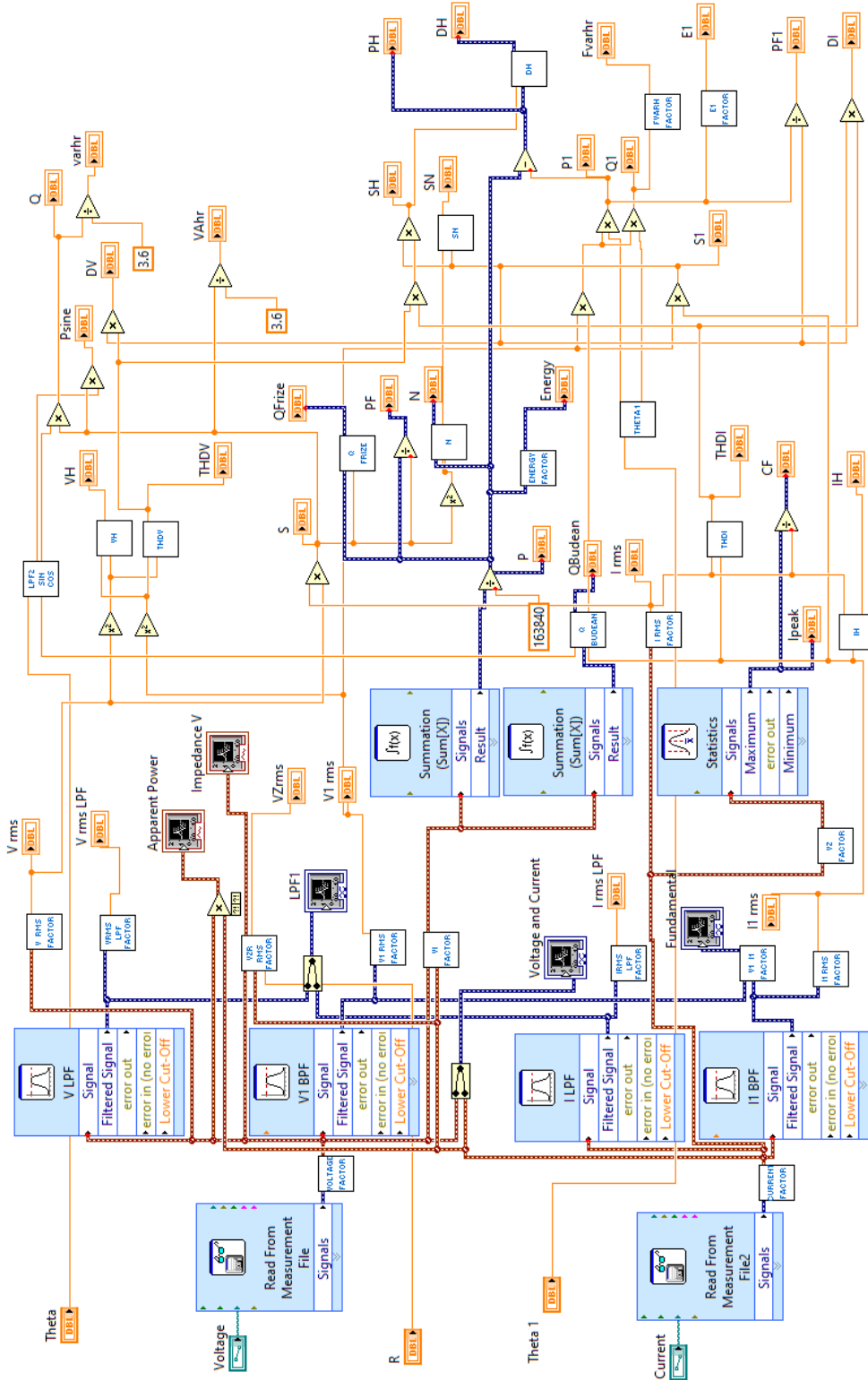


Figure 4.15: ADE7878A IC model full block diagram.

4.4.4 ADE7878A IC Model Accuracy

The ADE7878A IC implements the calculations described in subsection 4.3.2.2 whereas the IC's proposed model tries to closely replicate these calculations, as described in F, based on the limited information provided by Analog Devices in the IC's data-sheet [73]. Therefore, some differences are expected to exist among the IC's model results and the ADE7878A real measurements. In particular, there is very limited information provided by the manufacturer regarding the LPF and BPF implemented in the real device, and, consequently, these filters were designed based on the closest response to the model when compared to the real measurements results.

To validate the model, calculated results from the model are compared to the measurements performed by the ADE7878A IC. The results presented in Table 4.7 correspond to the IC model response to the *Sinusoidal*, *Standard nonsinusoidal* and *Real-world nonsinusoidal test* waveforms described in Section 4.2 at I_{ref} values, whereas the results from the IC's real measurements of the same waveforms at I_{ref} values, are presented in Table 4.8. All results are expressed as relative errors.

Table 4.7: ADE7878A IC model test results.

| Quant | Sin | HarmP | HarmQ | Quad | Peak | CFL | Ent-Sys | S-M PS |
|------------|------|--------------|--------------|--------------|-------------|-------------|--------------|-------------|
| θ | 0.17 | -4.02 | -1.46 | -7.25 | 2.85 | 1.63 | -2.56 | -0.51 |
| V_{rms} | 0.16 | 0.00 | 0.01 | 0.05 | 0.02 | 0.08 | 0.09 | 0.01 |
| I_{rms} | 0.05 | 0.25 | 0.36 | 0.23 | 0.24 | 0.24 | 0.29 | 0.43 |
| I_{peak} | 0.10 | 0.10 | 0.11 | 0.10 | -0.13 | 5.13 | 0.36 | -0.05 |
| S | 0.29 | 0.08 | 0.19 | 0.10 | 0.09 | -0.15 | -0.05 | -0.05 |
| P | 0.29 | 0.09 | 0.34 | 0.11 | 0.09 | 0.18 | -0.05 | -0.09 |
| E_S | 0.02 | 0.14 | 0.04 | 0.13 | 0.15 | -0.22 | -0.15 | -0.13 |
| E | 0.02 | 0.16 | 0.09 | 0.13 | 0.15 | 0.21 | -0.15 | -0.09 |
| E_1 | 0.02 | 0.15 | 0.04 | 0.15 | 0.12 | -0.90 | 0.61 | 0.62 |
| E_{Q1} | 0.02 | 0.01 | 0.01 | 0.01 | 0.01 | 0.28 | 2.75 | 2.10 |

Table 4.8: ADE7878A IC real measurements results.

| Quant | Sin | HarmP | HarmQ | Quad | Peak | CFL | Ent-Sys | S-M PS |
|------------|------|--------------|--------------|--------------|-------------|-------------|--------------|-------------|
| θ | 0.33 | -4.13 | -1.58 | -7.74 | 2.36 | 1.54 | -2.82 | -0.22 |
| V_{rms} | 0.01 | 0.05 | 0.06 | 0.06 | 0.05 | 0.10 | 0.11 | 0.08 |
| I_{rms} | 0.16 | 0.11 | 0.10 | 0.12 | 0.18 | 0.16 | 0.18 | 0.17 |
| I_{peak} | 0.18 | 0.17 | 0.17 | 0.16 | 0.15 | 5.56 | -0.40 | 0.01 |
| S | 0.17 | 0.10 | 0.16 | 0.14 | 0.13 | -0.29 | -0.12 | -0.01 |
| P | 0.17 | 0.11 | 0.42 | 0.10 | 0.12 | 0.16 | -0.11 | -0.06 |
| E_S | 0.08 | 0.15 | 0.13 | 0.13 | 0.17 | 0.18 | -0.13 | -0.16 |
| E | 0.08 | 0.15 | 0.13 | 0.13 | 0.17 | 0.18 | -0.13 | -0.16 |
| E_1 | 0.07 | 0.17 | 0.09 | 0.18 | 0.13 | -0.96 | 0.45 | 0.26 |
| E_{Q1} | 0.01 | 0.01 | 0.01 | 0.01 | 0.01 | 0.32 | 2.89 | 2.26 |

In Figure 4.16, the difference between relative errors from IC's model results and the relative errors from IC's real measurements for the different applied tests is presented.

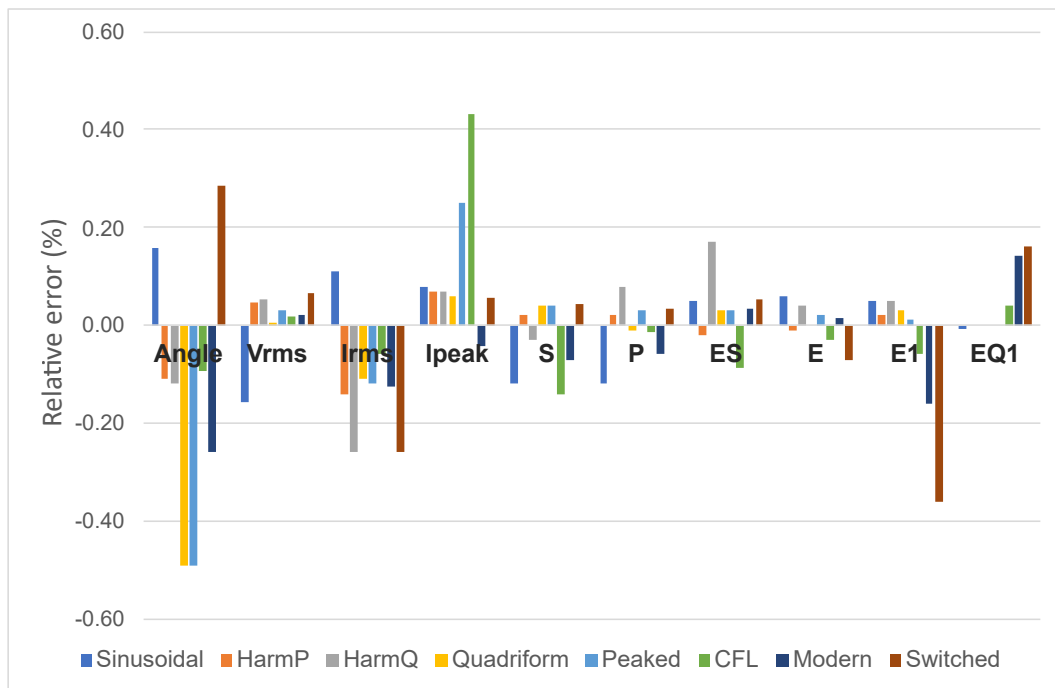


Figure 4.16: Error difference between IC's model and IC's real measurements

From the results in Table 4.7, it is worth noting that most of the quantities are estimated by the IC model with an error lower than $\pm 0.5\%$, which is lower than the targeted $\pm 1\%$ relative error for the purposes of this study. Highlighted values (in bold)

that exceed the $\pm 1\%$ relative error correspond to the phase angle calculation. These phase angle values, however, are not used by the ADE7878A IC (or the developed IC model) to perform further calculations and it is provided by the IC only as an additional value to estimate power factor.

I_{peak} calculations for the *CFL* test waveform present a very large relative error compared to the other tested signals. This large error, that is further analysed and discussed in the next chapter, is related to one specific waveform parameter: the signal slope.

Finally, the waveforms *Modern entertainment system* and *Switched-mode power supply* (last two columns of Table 4.7, respectively) present significant relative error for the fundamental reactive energy E_{Q1} .

4.5 Chapter Summary

Conventional approaches to evaluate electricity meters accuracy under nonsinusoidal waveform conditions focus on the harmonic content on the voltage and current signals. In this chapter, however, a novel approach has been proposed focusing on the shape of resulting waveforms with fast amplitude changes defined by the combination of three signal characteristics: the amplitude peak value, the signal rms, and the impulsive transition duration.

In order to investigate the influence of fast-changing signals in electricity meters, the response of a representative energy metering IC, one of the most important components typically found in static meters, has been evaluated applying different tests i.e. sinusoidal, standard nonsinusoidal tests, real-world nonsinusoidal signals and the newly proposed amplitude fast-changing signals tests.

An electricity metering system has been constructed based on the ADE7878A energy metering IC and fully described in this chapter. The transducers are omitted and data files representing signals coming from ideal inductive (e.g. CT or VT) or resistive (e.g. shunt or RVDT) transducers are used instead, employing the phantom-loading technique.

A Raspberry Pi board, running a developed LabVIEW code, is used to interface the ADE7878A with the host PC. Through the Raspberry Pi, it is possible to configure and calibrate the ADE7878A IC, as well as acquiring measurements results directly from the IC registers, allowing analysis of error propagation within ADE7878A digital blocks before final calculations.

For the first time, a novel energy metering IC model, based on the ADE7878A has been developed in LabVIEW as a useful tool to predict the response of this class of integrated circuits, and thus electricity meters, to any kind of sinusoidal or nonsinusoidal waveform.

The ADE7878A model characteristics have been described in this chapter, including a validation of the model revealing an accuracy lower than 0.5% relative error for most of the calculated electrical quantities, compared to the real measurements of the ADE7878A.

Chapter 5

Experimental Results and Analysis

In this chapter, the results from the tests described in Section 4.2 are presented and discussed. Most of the results are reported as relative error as per formula 2.29 whereas for measurements with a reference value equal to zero, the absolute error is calculated as:

$$\Delta x = x_0 - x \quad (5.1)$$

where x_0 is the measured value and x is the reference value.

All the tests applied to the ADE7878A IC have been performed in the same manner:

1. The AWG generates one cycle of the voltage and current signal waveforms, simultaneously and independently.
2. The one cycle waveform is continuously repeated by the AWG.
3. The LabVIEW's application reads the ADE7878A internal registers to obtain the IC's calculations 100 times per second.
4. The 100 readings are averaged and the results are displayed and saved in a .csv file once a second for 10 minutes.

5. The resulting measurements, i.e. the 600 values saved in the .csv file, are averaged. This is the final ADE7878A measurement result.
6. The final result (from step 4) is compared to the theoretical value and the relative error is obtained as per formula 2.29.

All the tests were repeated at least three times to verify the repeatability of the measurements.

Internally, the ADE7878A synchronizes all its measurements with the zero-crossing occurrence of the low-pass filtered voltage signal. Thus, it is expected that all obtained samples were always in the same relative positions on the waveform, minimizing the effect of systematic measurement errors.

The chapter is organized as follows: section 5.1 presents results from sinusoidal tests, intended for calibration verification and to confirm that no significant error has been produced under ideal sinusoidal situations. Sinusoidal tests includes a novel phase angle sweep which has been proposed to observe how the energy measurements error are related to different values of power factor. Later, in section 5.2, the ability of the ADE7878A metering IC to accurately estimate electrical parameters under standard nonsinusoidal test conditions is analyzed. In section 5.3, the results from applying real-world nonsinusoidal signals and the influence of harmonic content in measurement error is discussed. In section 5.4, the results from a novel proposed test, designed to investigate the effects of fast-changing currents with different characteristics, are reported and discussed, including the analysis of the waveforms as has been digitized by the IC's ADC.

5.1 Sinusoidal Tests Results

After calibration (fully described in C), different emulated power inputs were applied to the IC, by means of changing the current signal value, whereas the voltage input signal is kept at nominal value U_n . The accuracy of the IC has been evaluated, in sinusoidal conditions, over the IC's ADC full scale. For a more detailed appreciation, the results have been plotted in two graphs.

Figure 5.1 shows relative error for the measurements obtained when applying sinusoidal current signals from 0.2 A up to 1 A (i.e. below and up-to I_{min}), where more relaxed standard accuracy requirements applied. The reason to have a more relaxed error allowance for this current range is because the signal has an amplitude below 1% of the ADC's full scale input and, consequently, it is more prone to be affected by the noise.

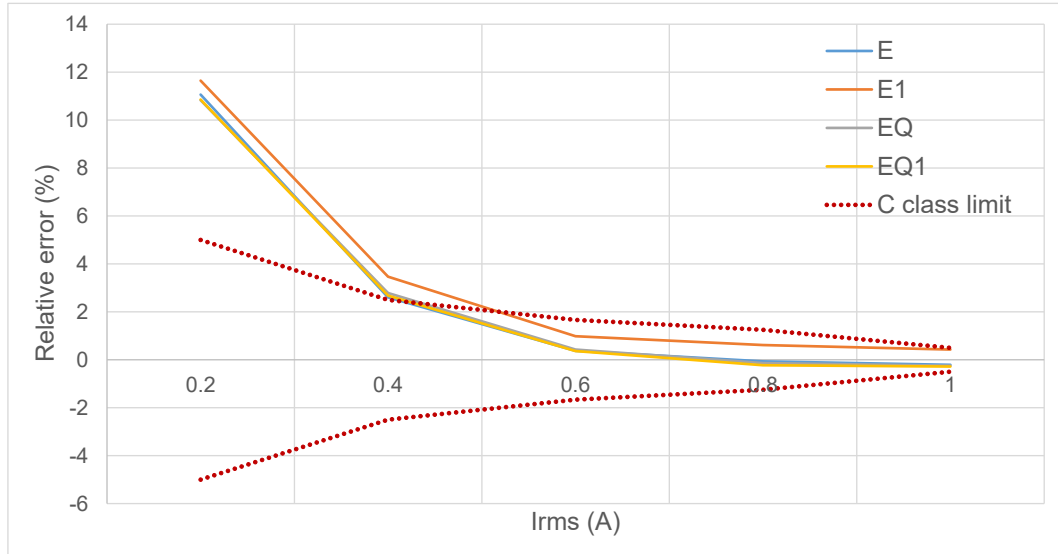


Figure 5.1: Sinusoidal tests results from 0.2 to 1% ADC full scale.

Figure 5.2 shows relative error energy for measurements in the range from 1A to 100A (I_{max}). The IC can measure total active energy E , in sinusoidal conditions, with a relative error lower than $\pm 0.5\%$, corresponding to a “C” class meter. The fundamental energy E_1 results present an offset which could be compensated after calculations.

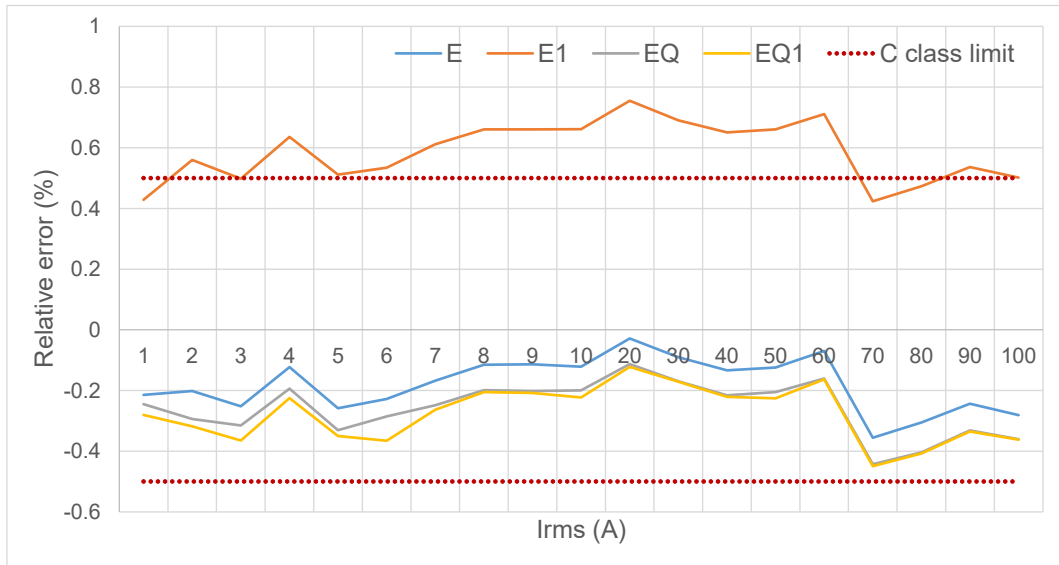


Figure 5.2: Sinusoidal tests results from 1 to 100% ADC full scale.

5.1.1 Phase Angle Error

The results from the sinusoidal test show a noticeable error with a significant dispersion in the phase angle estimation for the low range of the ADC full scale (Figure 5.3). To further analyze this error, a phase angle error test was performed, applying perfect sinusoidal signals for the voltage and current inputs in phase at zero crossing; thus, the expected angle measurement should be close (or equal) to $\theta = 0$. For this test, the current signal increases its amplitude in steps of 5A (i.e. increments of 5% ADC full range) up to 50% of the ADC full range, whereas the voltage signal is kept at nominal value U_n . The phase angle error and its large dispersion are “corrected” once the current signal surpass 10% of the ADC nominal input. i.e. 100 mVpp. After this 10% threshold, the performed calibration achieves an absolute phase angle error of approximately 0.1° ; lower than typical 0.3° absolute error claimed by the manufacturer.

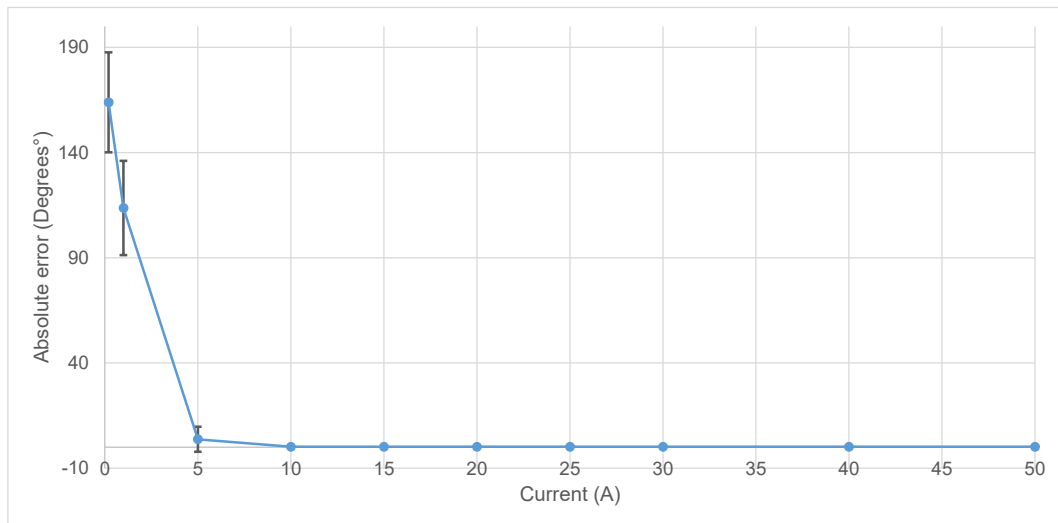


Figure 5.3: Phase angle error.

To calculate the phase angle, the ADE7878A (and consequently the IC model presented in Chapter 4) measures the time delay between the voltage and current signals, using as a start and stop points, the transition from negative to positive detected by the voltage and current zero-crossing (ZX) internal circuits (see 4.3.2.2). It seems that the phase angle error presented in this section, has been identified by the IC manufacturer as there is a relevant comment in the product datasheet [73] indicating that *“In order to provide further protection from noise, input signals to the voltage channel with amplitude lower than 10% of full scale do not generate zero crossing events at all”*. However, the zero-crossing detector on the current channel is always active, regardless of the signal amplitude.

Because of this phase angle error, it is not recommended to obtain power factor calculations by means of the cosine of the phase angle. Instead, power factor can be calculated from P and S values (2.31) as recommended in IEEE 1459:2010 standard [20].

5.1.2 Total active power at PF = 0 and Reactive Power at PF = 1

When applying the signals from the sinusoidal test for calibrating the meter for reactive power measurements, another error was detected for the phase angle value of 90° , corresponding to a Power Factor equal to zero (i.e. only fundamental reactive power

was produced). This error is a non-zero output, when no active power is applied to the meter inputs. To investigate this error, a validation test was performed, by changing the amplitude of the current sinusoidal input by increments of 5% of the ADC full range from 0 to $0.5I_{max}$, whereas the voltage input signal is kept at nominal value U_n . The signals were applied to the ADE7878A, but this time the current signal is delayed by 90° with respect to the voltage signal. The total active power measurements have a linear negative gain error (Figure 5.4), with a negligible impact on the final energy calculation for sinusoidal waveforms.

Due to the theoretical ideal value $P = 0$ W, the absolute error (5.1) is reviewed instead of the relative error. Thereby, the total active power absolute error at 11500 var, PF = 0, is approximately -50W, representing -0.43% of the total apparent power applied at the meter inputs. For the measurements where the theoretical value is different to zero, the relative error, expressed as a percentage (2.29), is preferred.

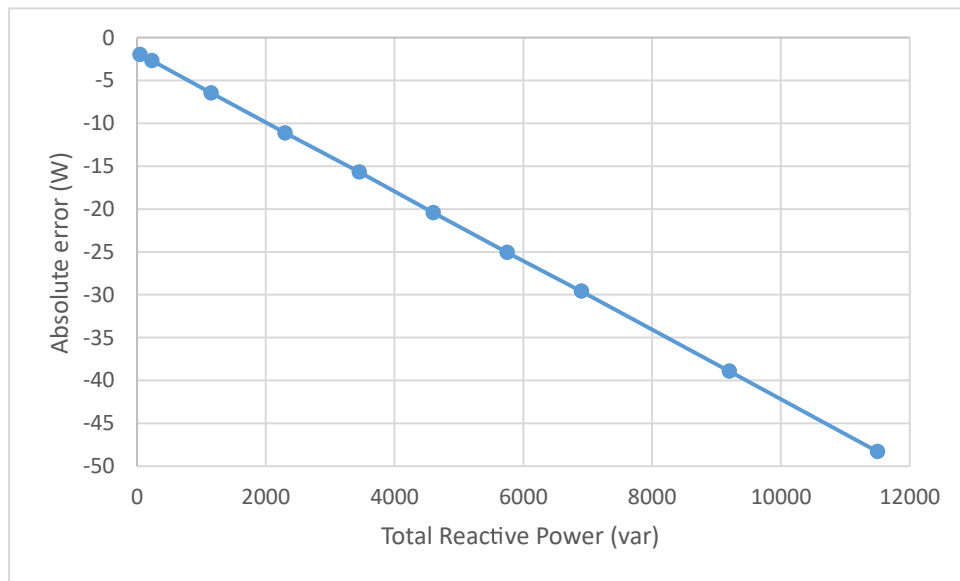


Figure 5.4: Total active power absolute error.

In general, the measurement accuracy degrades significantly below 10% of the ADC input range. This is caused by the low signal to noise ratio (SNR) dominating the region, thereby affecting the phase angle estimation. Similarly, in Figure 5.5, one can observe significant errors below the 10% ADC input threshold (i.e. 2300 VA) for

reactive and apparent power.

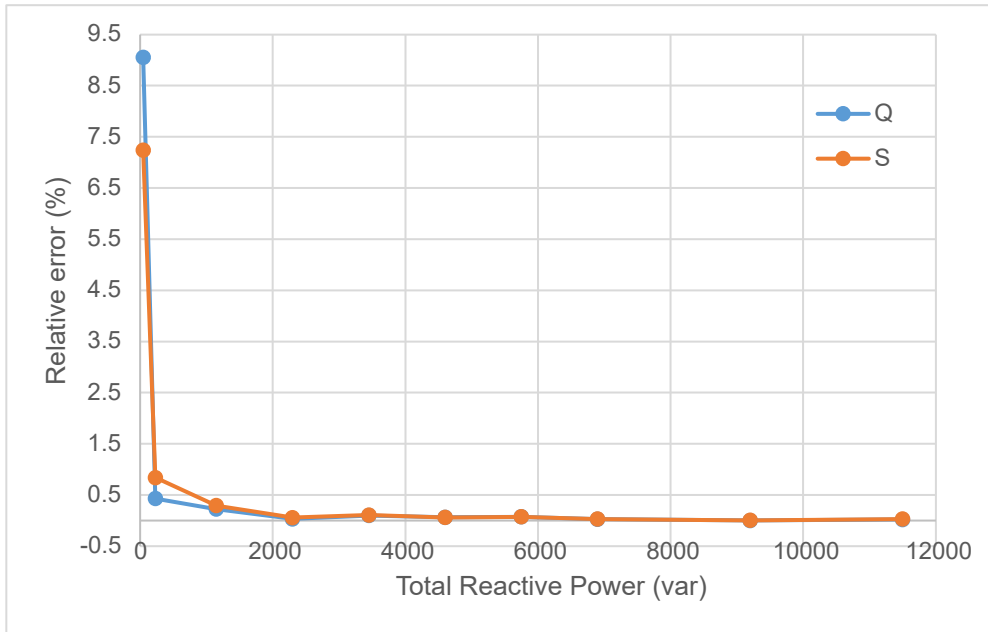


Figure 5.5: Total apparent power and total reactive power relative error.

Very similar results have been obtained for reactive power calculations at $PF = 1$, with a non-zero output for reactive power increasing linearly (Figure 5.6) and significant errors in total active power and apparent power measurements below 10% of the ADC input range threshold (Figure 5.7).

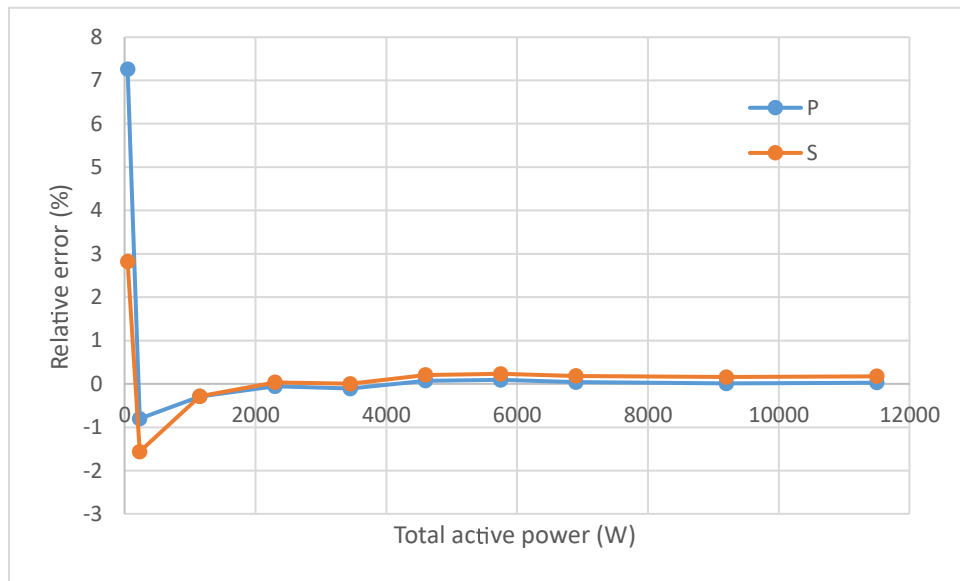


Figure 5.6: Total apparent power and total active power relative error.

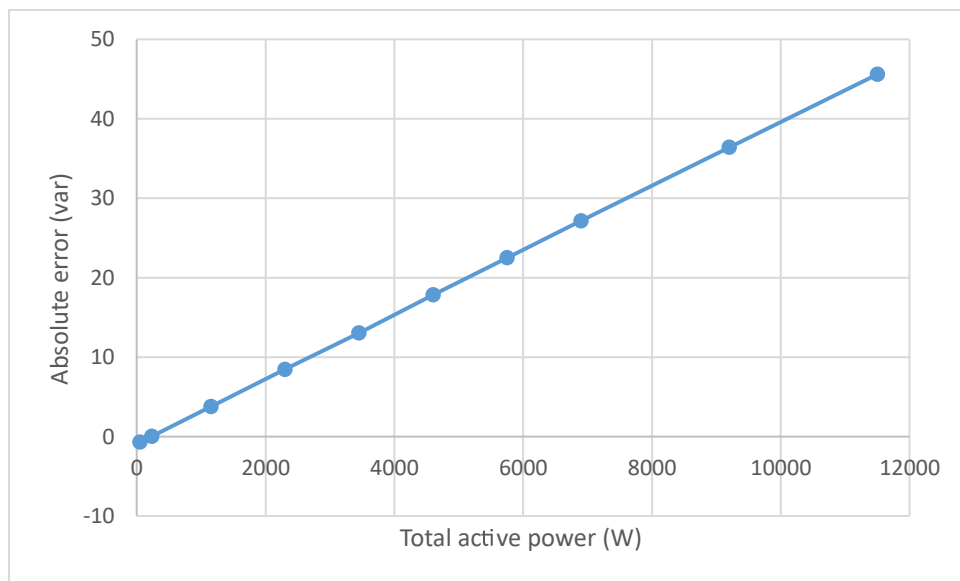


Figure 5.7: Total reactive power absolute error.

5.1.3 Sinusoidal Phase Swept Test Results

The phase angle has been highlighted as a possible parameter which significantly influences meter accuracy [16,76]. For this reason, a phase angle sweep has been performed in sinusoidal conditions, from 0 to 360° in steps of 15°, at nominal values I_{ref} and U_n .

Figure 5.8 illustrates that the total active power relative error varies depending on the phase angle between the voltage and current signals. Furthermore, Figure 5.8 exhibit for the first time that there are both negative and positive relative errors. This is an interesting finding, as positive errors have been previously related with an over-estimation of the input signals, whereas a negative error is believed to be caused by a low sampling rate [88]. In this test, however, the signal amplitudes and the ADC sampling frequency remain constant while only phase angle is changed.

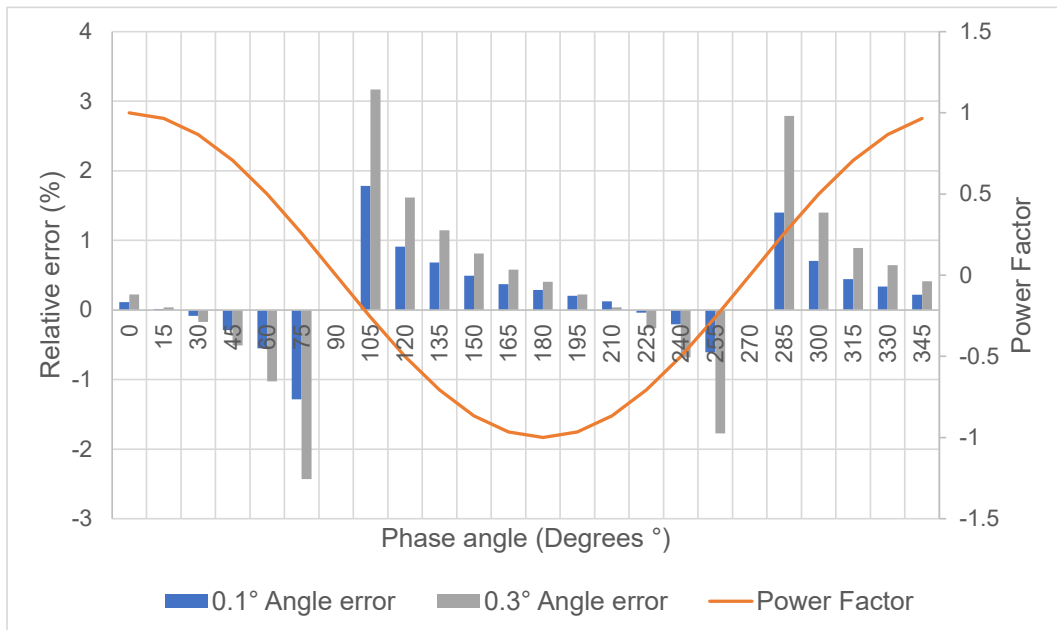


Figure 5.8: Total active power relative error versus phase shift.

A well performed calibration and phase delay compensation will impact on the final power (and energy) measurement, particularly at lower power factors [73]. The grey colour bars on Figures 5.8 and 5.9 corresponds to a typical 0.3° phase angle absolute error, whereas the blue bars correspond to a better performed calibration (by means of using a more accurate reference) achieving 0.1° absolute error. Careful phase delay compensation will prevent standard-compliant meters from presenting large errors at low power factors.

Figure 5.9 shows the relative errors in the total reactive power measurements, with similar results as in Figure 5.8 for the total active power.

It is clear that the phase angle is a key parameter influencing the active and reactive power measurement error and its sign. Nonetheless, it is important to keep in mind that relative errors are larger when the reference (or ideal) value is close to zero. In Figures 5.8 and 5.9 can be seen for the first time how relative error increases asymptotically near phase angle values where the reference quantity equals to zero. For this reason, the relative errors at 90° and 270° are omitted in Figure 5.8 and the relative errors at 0° and 180° are omitted in Figure 5.9.

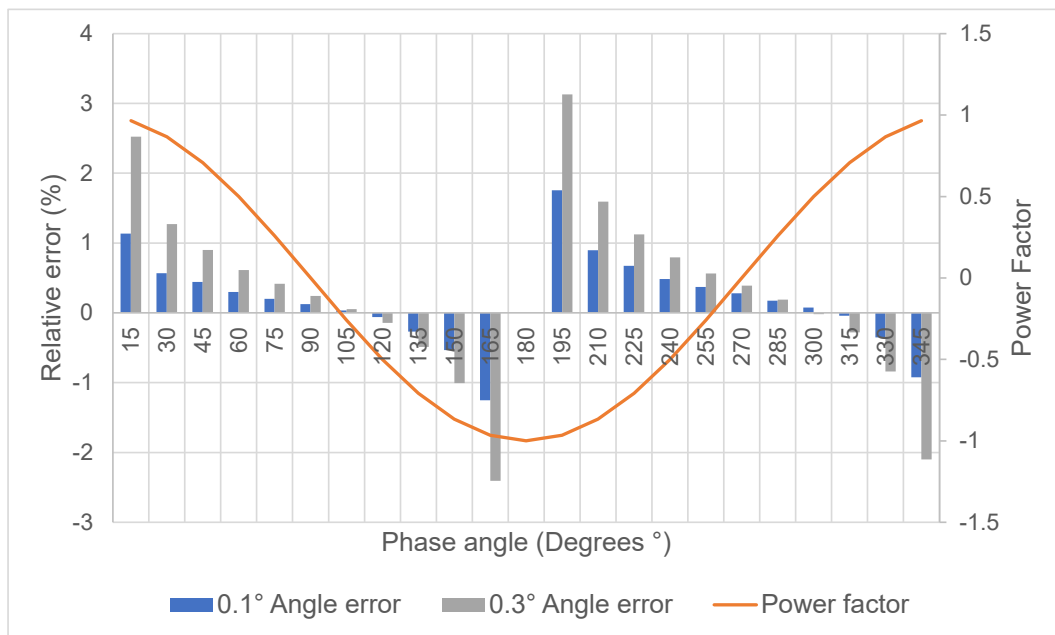


Figure 5.9: Total reactive power relative error versus phase shift.

5.2 Standard nonsinusoidal Test Results

All the standard nonsinusoidal test signals can be measured by the ADE7878A with a very good accuracy. Voltage and current rms relative errors are very small, particularly for the voltage signal (Figure 5.10).

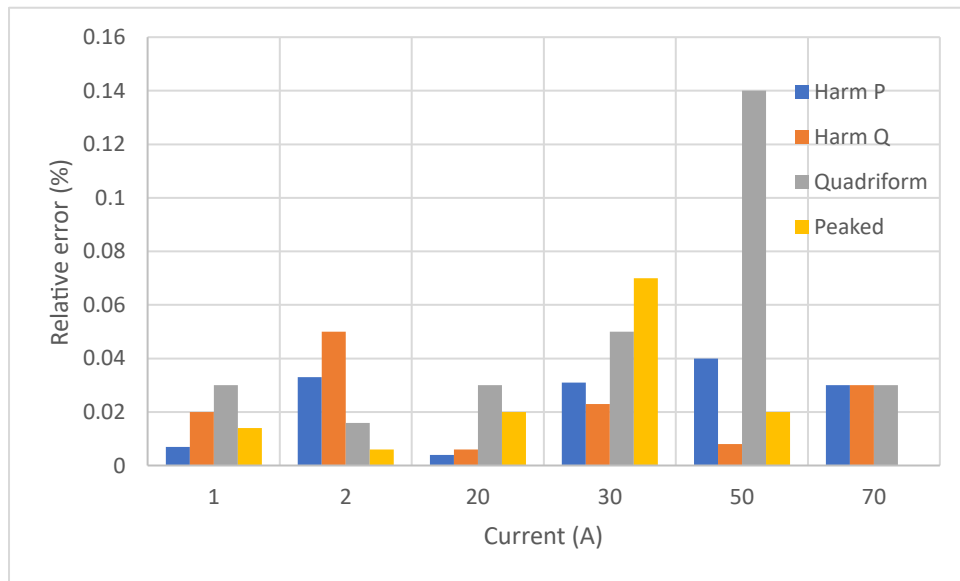


Figure 5.10: Voltage rms relative error.

The current rms (Figure 5.11) presents relative errors above 0.5% only for signals smaller than 10% of the ADC full scale, regardless of the harmonic content, supporting the fact that energy metering technology can effectively measure signals with harmonic content.

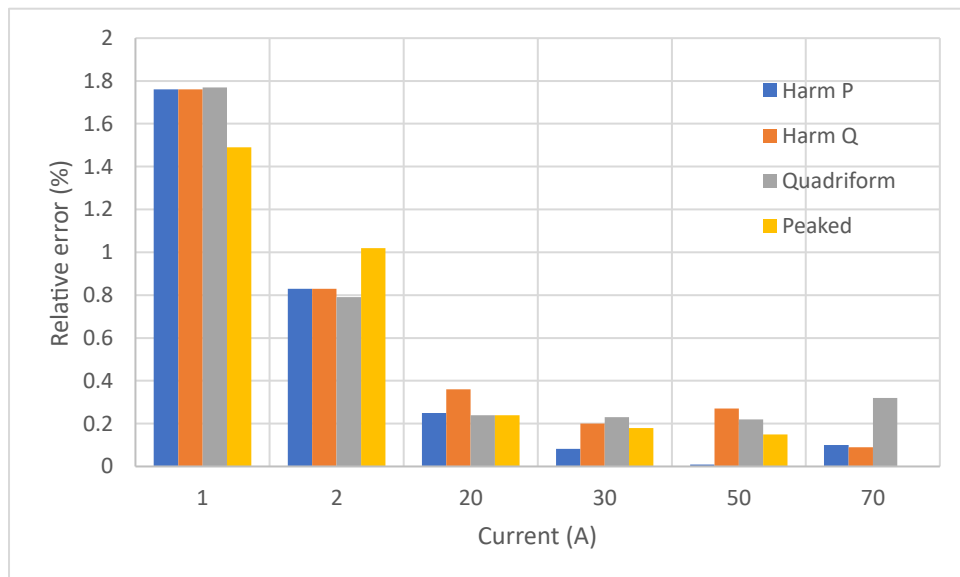


Figure 5.11: Current rms relative error.

Chapter 5. Experimental Results and Analysis

Total active power and total apparent power relative errors are presented in Figures 5.12 and 5.13, respectively.

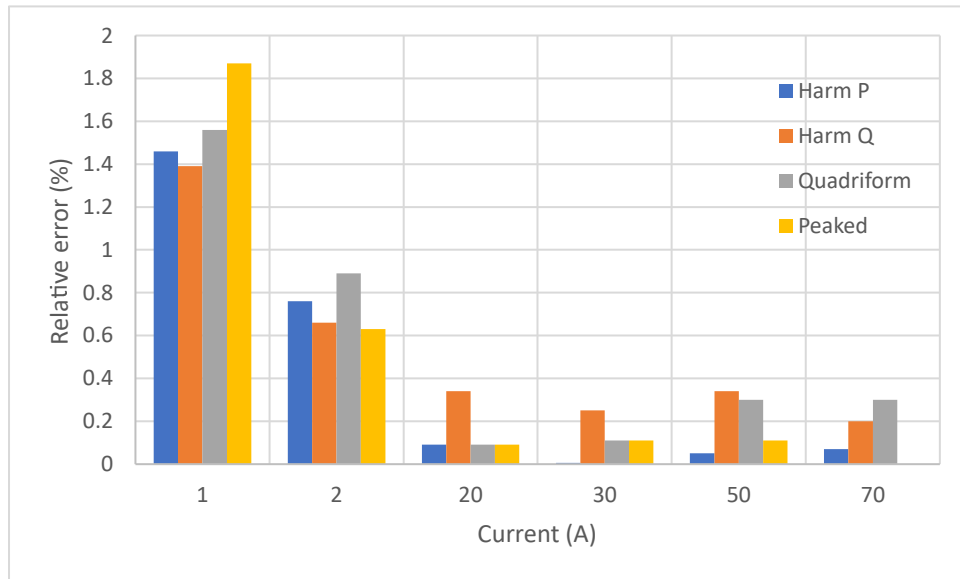


Figure 5.12: Total active power relative error.

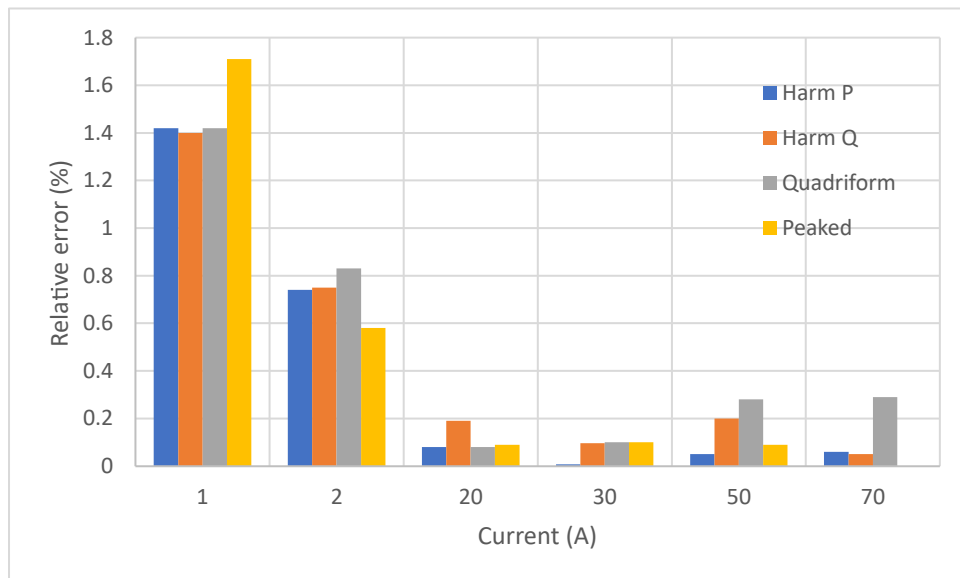


Figure 5.13: Total apparent power relative error.

The results in Figures 5.14 and 5.15 show total and fundamental active energy relative errors of up to +2%, only below the 10% ADC input range, proving that metering

IC technology can effectively estimate electrical quantities in certain nonsinusoidal situations.

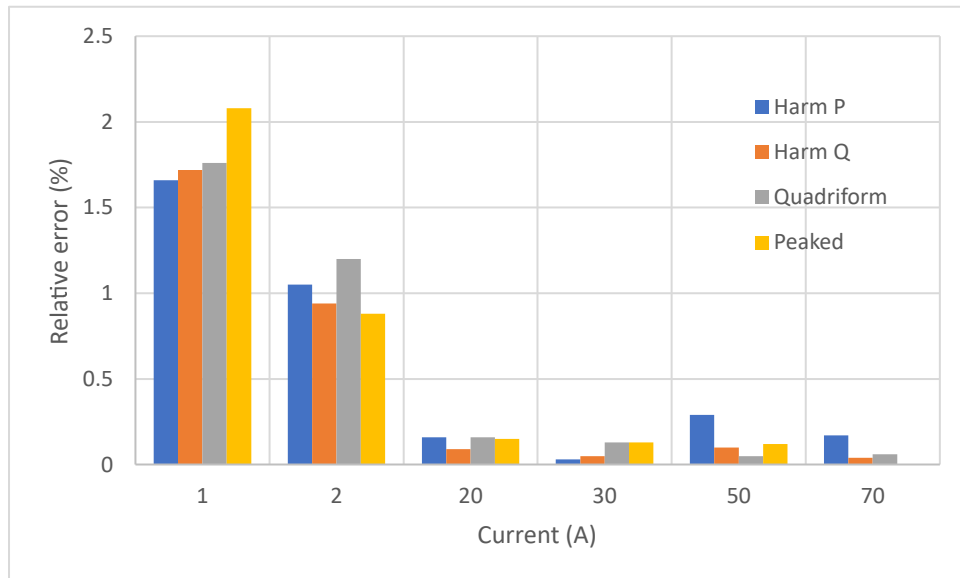


Figure 5.14: Total active energy relative error.

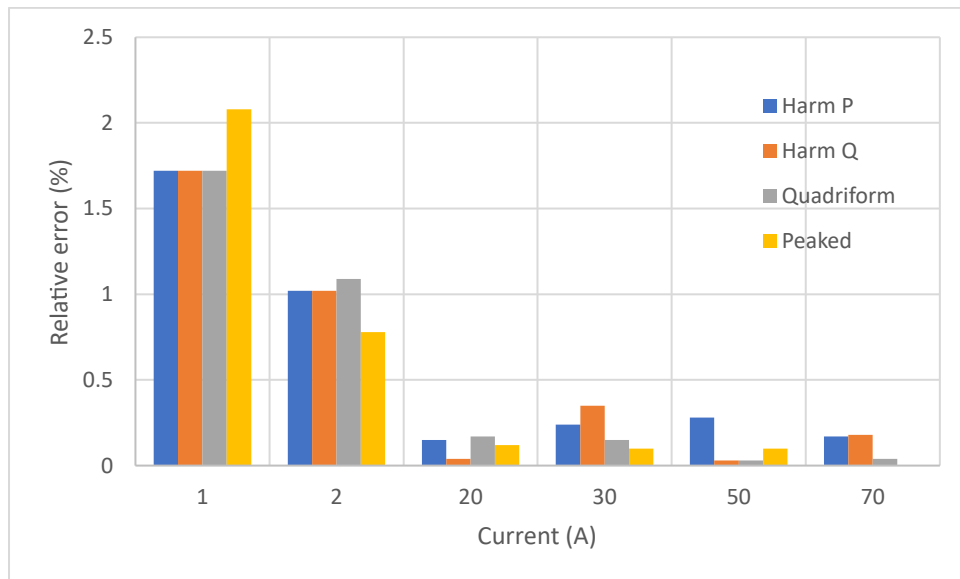


Figure 5.15: Fundamental active energy relative error.

Figure 5.16 presents relative errors for total apparent energy.

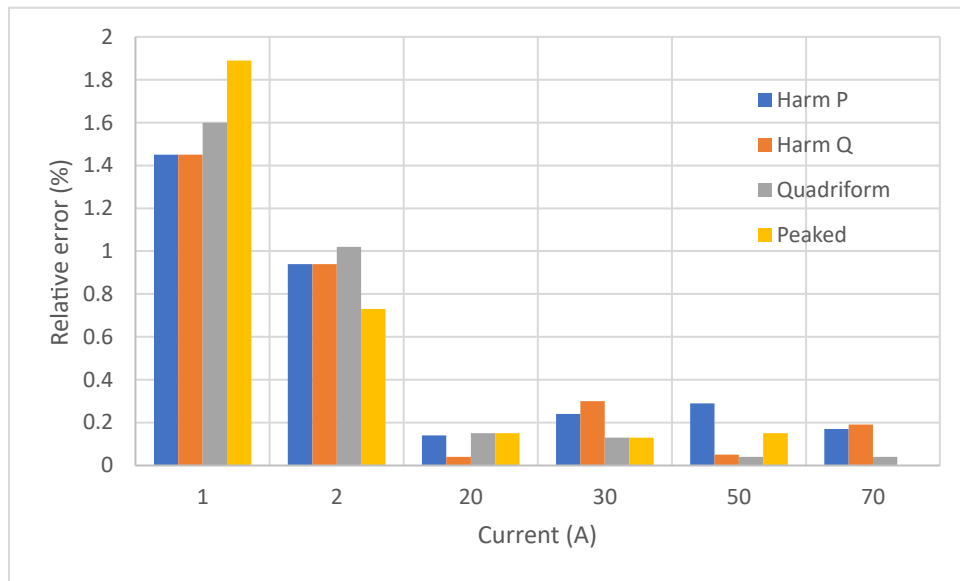


Figure 5.16: Total apparent energy relative error.

The total reactive energy is not given for nonsinusoidal current signals, as there is no formal definition for total reactive power in nonsinusoidal conditions. Thus, only the fundamental reactive energy is evaluated (Figure 5.17).

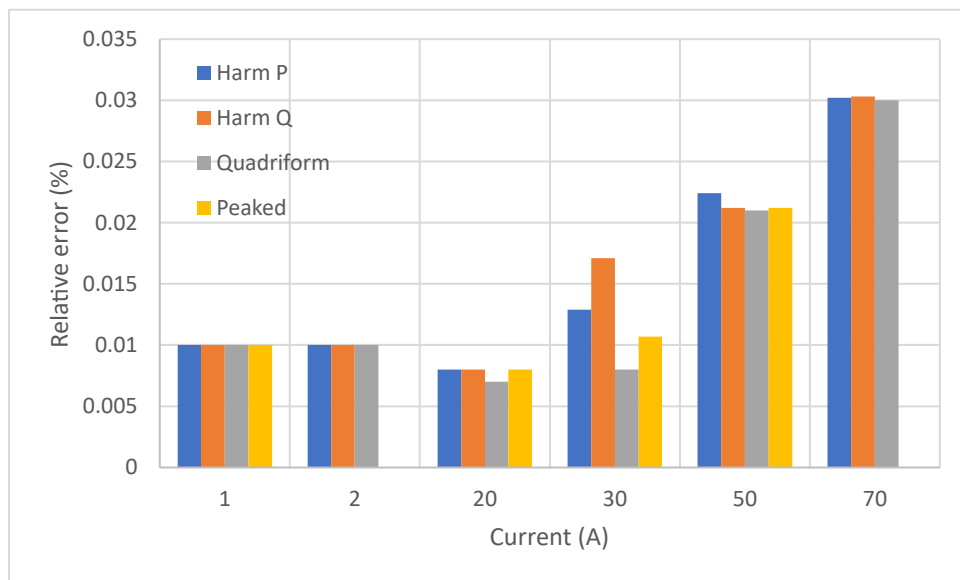


Figure 5.17: Fundamental reactive energy relative error.

5.3 Real-world Current Signal Tests Results

The current signals used for the real-world captured nonsinusoidal current tests are presented in this section. The most relevant quantities have been measured with a good accuracy (i.e. below 0.5% relative error) by the ADE7878A metering IC, except for the fundamental quantities E_1 with relative errors below 1% and E_{Q1} with a maximum relative error of 2.5% for the modern entertainment system waveform.

Figure 5.18 shows very small relative error for voltage and current rms measurements, including for the modern entertainment system waveform which produces the highest error among the real-world test signals.

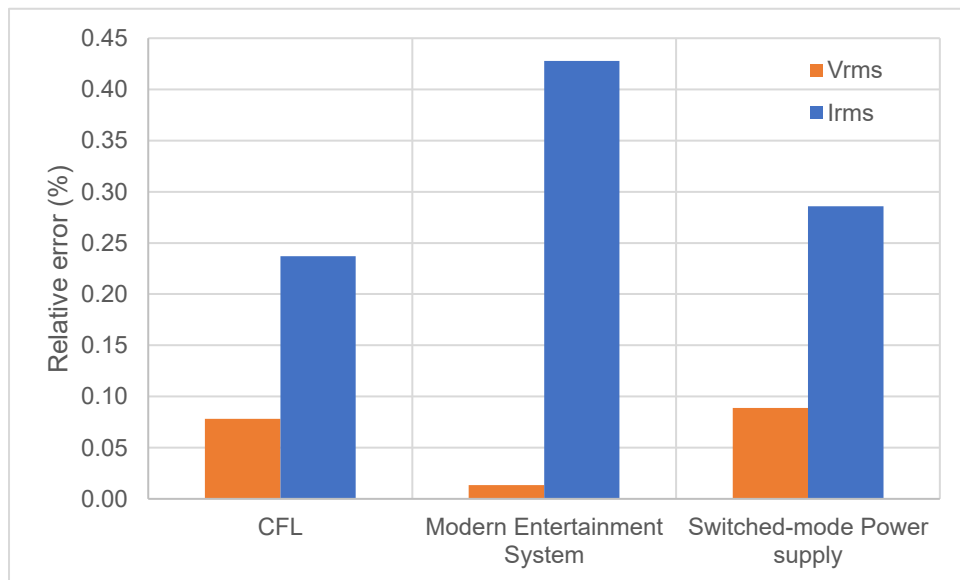


Figure 5.18: Voltage and current rms relative error.

Current peak measurements in Figure 5.19 show a significant relative error for the CFL signal, above 5%. The modern entertainment system signal and the switched-mode power supply show very small relative error for i_{peak} calculations. It is worth observing that the CFL signal presents the higher values of crest factor and slope (see Table 4.1). In this case, the slope is the parameter which causes the greatest degradation of the i_{peak} accuracy.

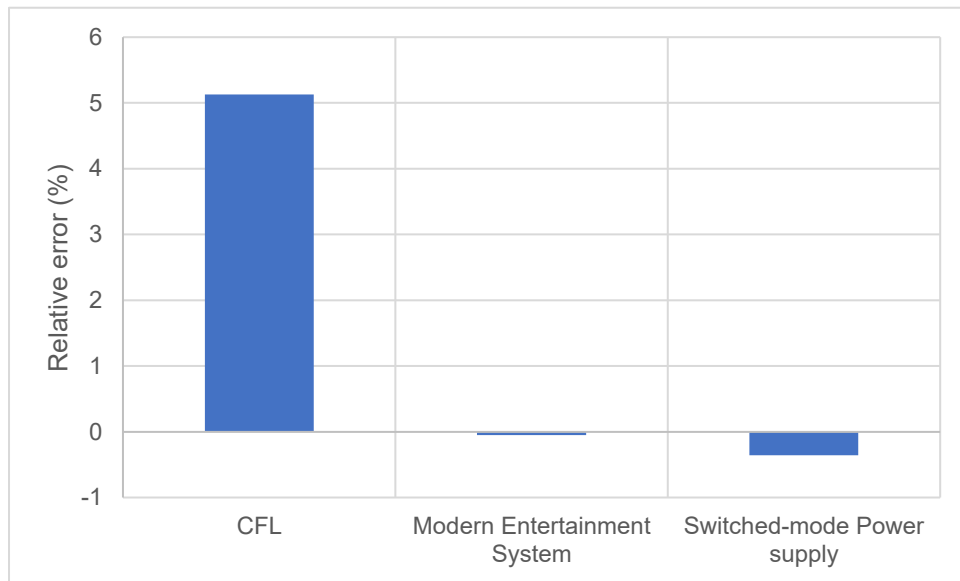


Figure 5.19: Peak current relative error.

In Figure 5.20 the relative errors for the total active power P and total apparent power S have been plotted. One can observe both positive and negative relative errors, although these errors are very small. CFL power measurements present the higher error, although lower than $\pm 0.2\%$. The modern entertainment system and the switched mode power supply signals produce relative errors lower than -0.05% and -0.1% , respectively.

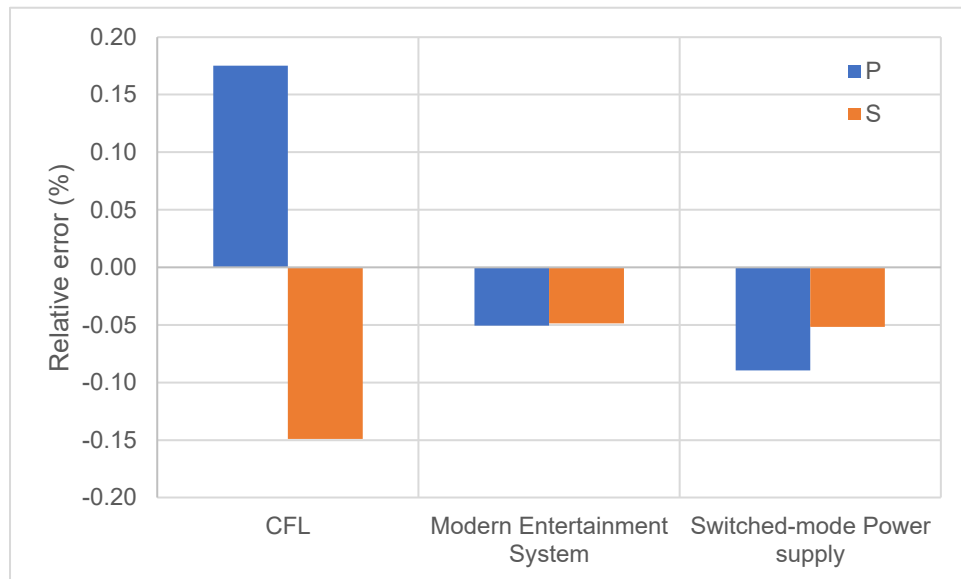


Figure 5.20: Total active power P and total apparent power S relative error.

Figure 5.21 shows the relative error for the total active energy E and total apparent energy E_S . The ADE7878A calculates E by integrating the instantaneous active power p values, which are the result of multiplying instantaneous samples of the voltage and current signals as $p = vi$. Thus, erroneous measurements produced during instantaneous current signal sampling will be reflected on the power and energy calculations. However, the averaging effect produced during E calculations due to the integral of p attenuates the error magnitude of such instantaneous current measurement. It can be observed from Figure 5.19 that the relative error on i_{peak} measurements shares the same sign and proportional error magnitude compared to the results plotted in Figure 5.21 for the different real-world current signals.

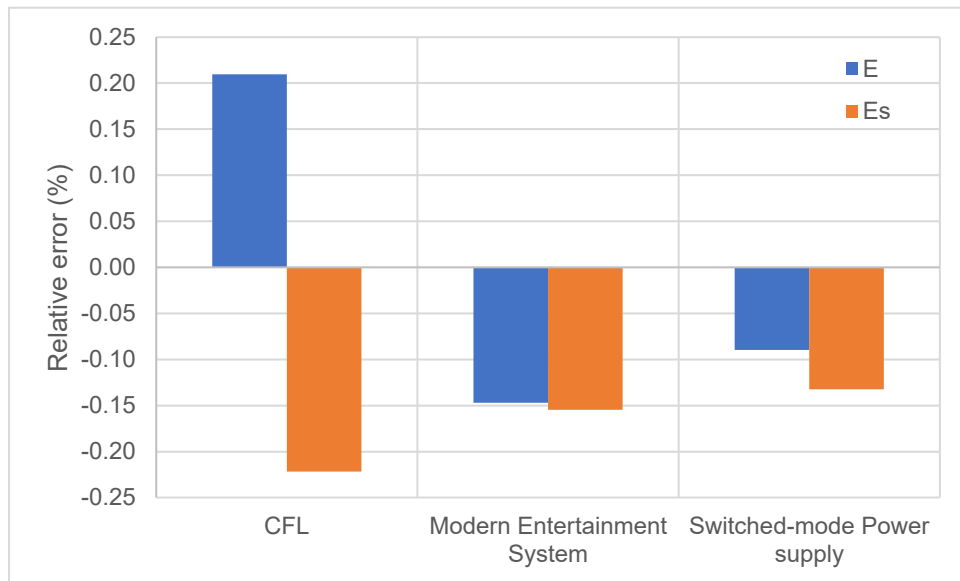


Figure 5.21: Total active energy E and total apparent energy E_S relative error.

The relative error of fundamental active energy E_1 and fundamental reactive energy E_{Q_1} are presented in Figure 5.22. For the fundamental quantities, the CFL signal presents the lowest error among the waveforms for the real-world nonsinusoidal current test. Modern entertainment system and switched-mode power supply signals produces the higher relative error for fundamental reactive energy.

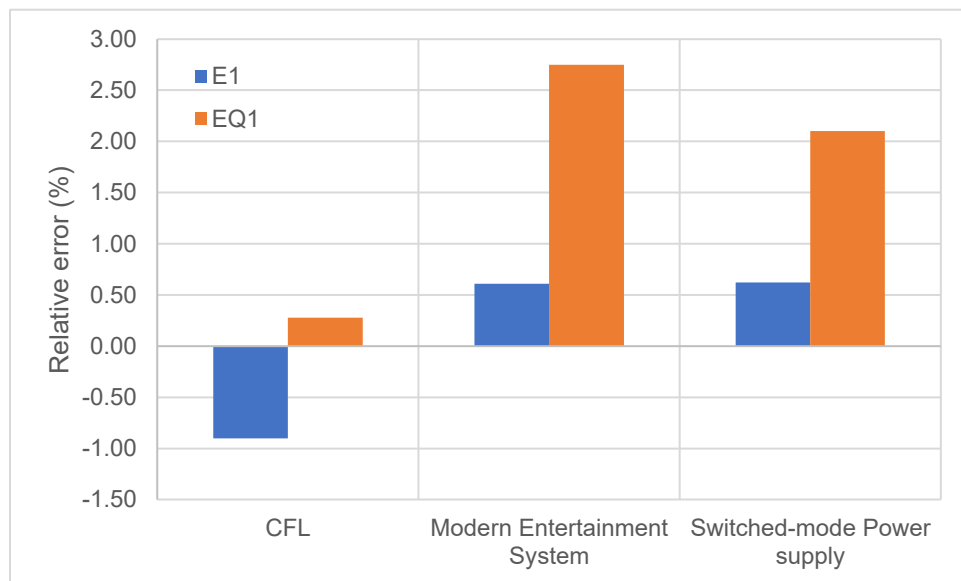


Figure 5.22: Fundamental active energy E_1 and fundamental reactive energy E_{Q_1} relative error.

Real-world current signal tests results prove that energy metering technology is capable to correctly estimate electrical quantities of nonsinusoidal waveforms produced by some appliances typically found in household situations, such as those employed for these tests. The results also reveal how the error is propagated inside the ADE7878A, with the error on i_{peak} measurements being the most noticeable, as the relative magnitude and sign are translated to the total active power and consequently the total active energy for the three tested signals. It is also worth noting that the largest error for total and fundamental active energy correspond to the CFL signal, with the highest slope value compared to the modern entertainment system and the switched power supply signals.

5.4 Crest Factor Tests Results

For all the crest factor tests, the voltage signal is a sinusoidal waveform, thus, the voltage rms measurements report a maximum relative error of 0.1%, regardless of the current crest factor. The current signals, however, become more rapidly-changing as the signal slope increases with the crest factor (see Table 4.1), making the measurements

more challenging for sampled-based measuring instruments.

In Figure 5.23, the I_{rms} relative error is shown. I_{rms} relative error is approximately the same for the “leading” and “falling” cases, increasing as the crest factor increases.

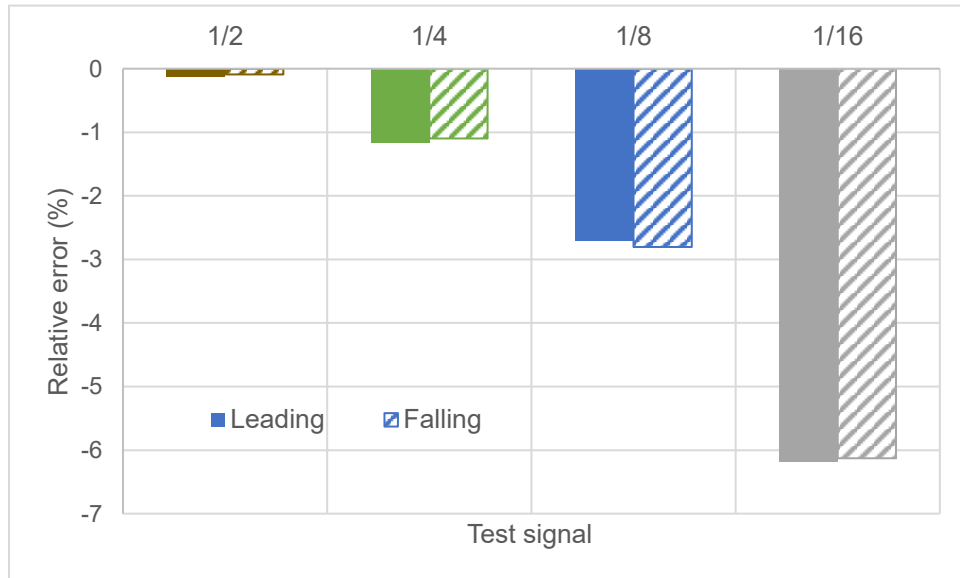


Figure 5.23: “Leading” and “Falling” I_{rms} relative error vs crest factor.

It can be seen from Figure 5.24 how the error in I_{rms} (Figure 5.23) is translated to the total apparent energy error. The magnitude of the error and its negative increase with respect to the crest factor are very similar in both graphs. This is expected, as the total apparent power calculation is based on rms measurements as per formula (2.32).

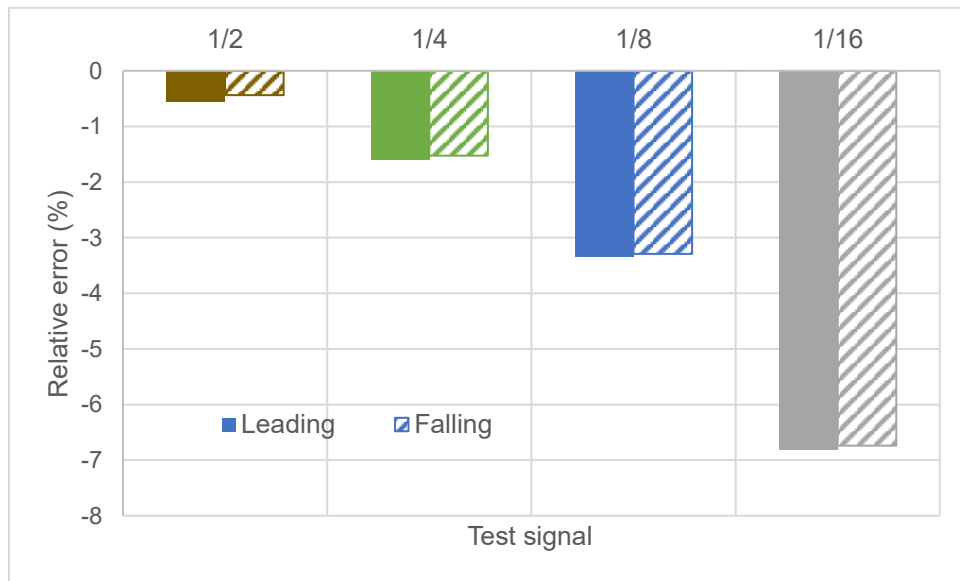


Figure 5.24: “Leading” and “Falling” total apparent energy E_S relative error vs crest factor.

The i_{peak} measurement accuracy behaviour, however, differs significantly and inconsistently depending on the crest factor. Large relative errors are present that can either significantly overestimate or underestimate the peak value of the signal (Figure 5.25).

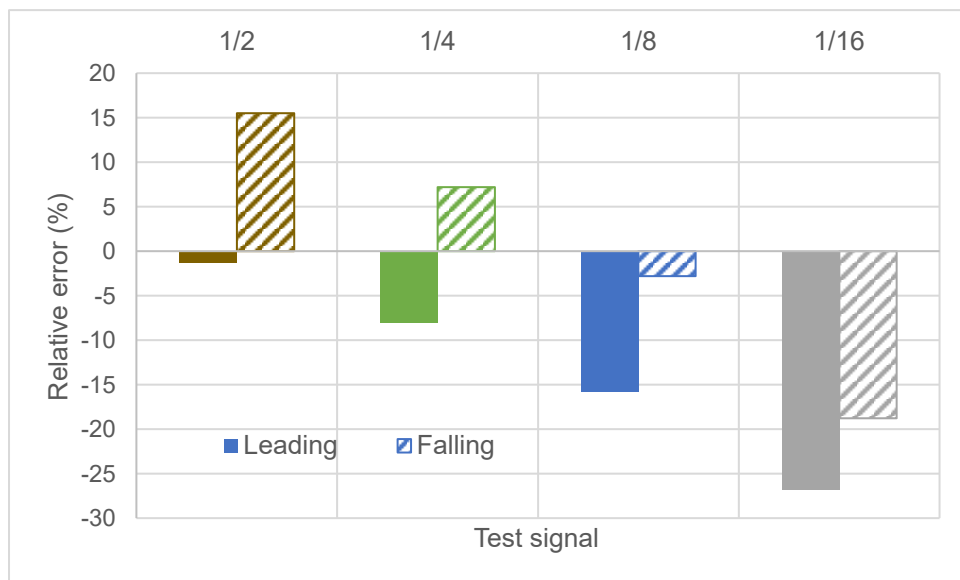


Figure 5.25: “Leading” and “Falling” i_{peak} relative error vs crest factor.

The cause of the i_{peak} measurement error and the difference among leading and falling signals relative error magnitude and sign are produced during the analogue to digital conversion, which will be analyzed later in this chapter, in Section 5.4.1.

The graph in Figure 5.26 shows significant larger error in the total active energy measurements for the “leading” test, compared to the “falling” test results. Since total active energy is the measurand used for billing purposes, particular attention has been paid to the “leading” tests.

Due to the symmetry among the “leading” and “falling” set of waveforms, and the fact that the signal power magnitudes are the same for both, it would be expected to produce a very similar relative error in the total active energy measurements. However a noticeable difference can be observed in the results presented in this section. Such difference or asymmetry in the relative error magnitude and its sign is partially explained by the time occurrence (i.e. the phase firing angle) of the rising and falling edges of proposed crest factor waveforms and the power factor. Moreover, a recent study performed by the MeterEMI project [80] which includes participation of universities and National Metrology Institutes of five European countries, reported in [94] similar results as those presented in this section, where fast falling edges (like those from the “leading” test signals) produce positive relative errors, i.e. overestimating the “real” value, whereas fast rising edges (like those from the “falling” test signals) produce negative relative errors, i.e. underestimating the “real” value.

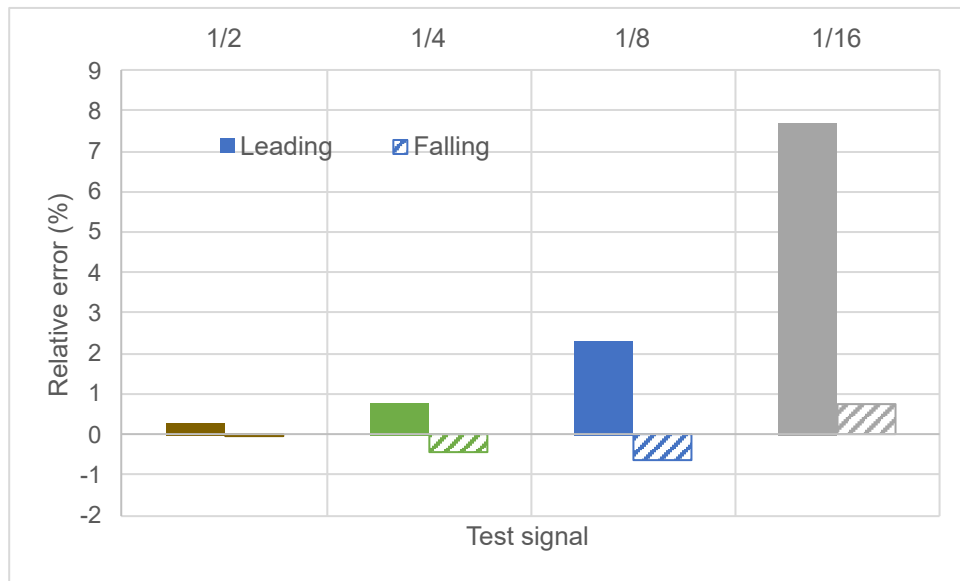


Figure 5.26: “Leading” and “Falling” total active energy E relative error vs crest factor.

Fundamental active energy E_1 relative error (Figures 5.27 and 5.28) shows a behaviour clearly related to the i_{peak} error displayed in Figure 5.25. The graphs in Figures 5.27 and 5.28 are very similar in shape to the corresponding results in Figure 5.25, although the magnitudes are smaller for the E_1 calculations. Again, the “leading” tests present the larger relative errors.

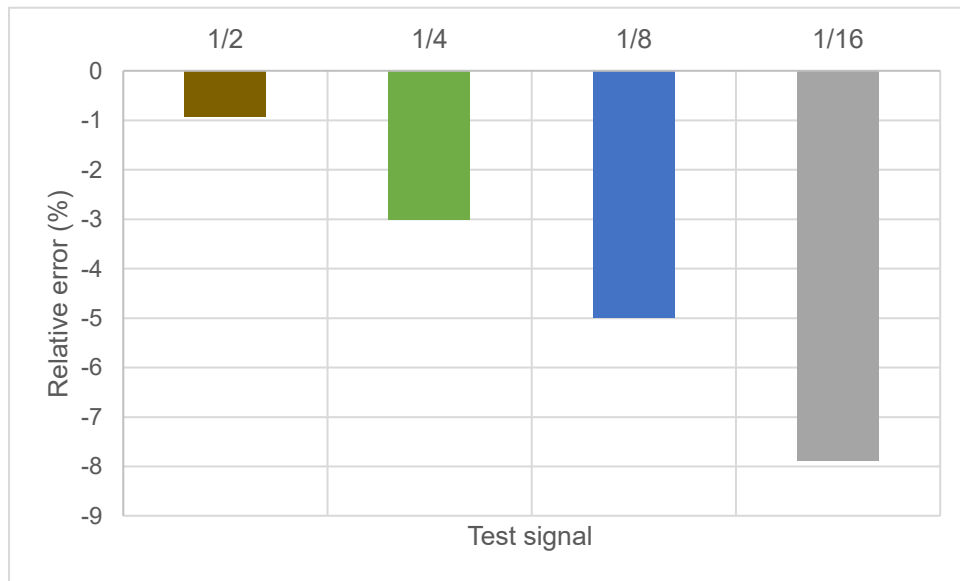


Figure 5.27: “Leading” fundamental active energy E_1 relative error vs crest factor.

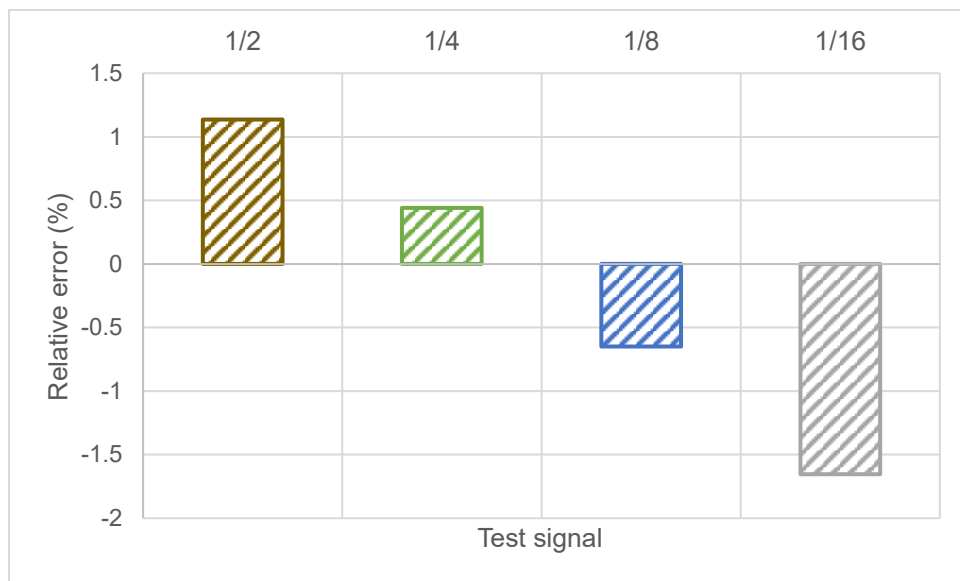


Figure 5.28: “Falling” fundamental active energy E_1 relative error vs crest factor.

5.4.1 ADE7878A Waveform Sampling

To further investigate the measurements error produced by the crest factor waveforms, the IC waveform sampling capabilities have been used. Figures 5.29 and 5.31 show how the crest factor current test signals have been distorted during the analogue to digital

conversion process. This distortion is only present for the crest factor test signals and do not occur for any other test signal presented in this thesis.



Figure 5.29: ADC “leading” sampled waveforms.

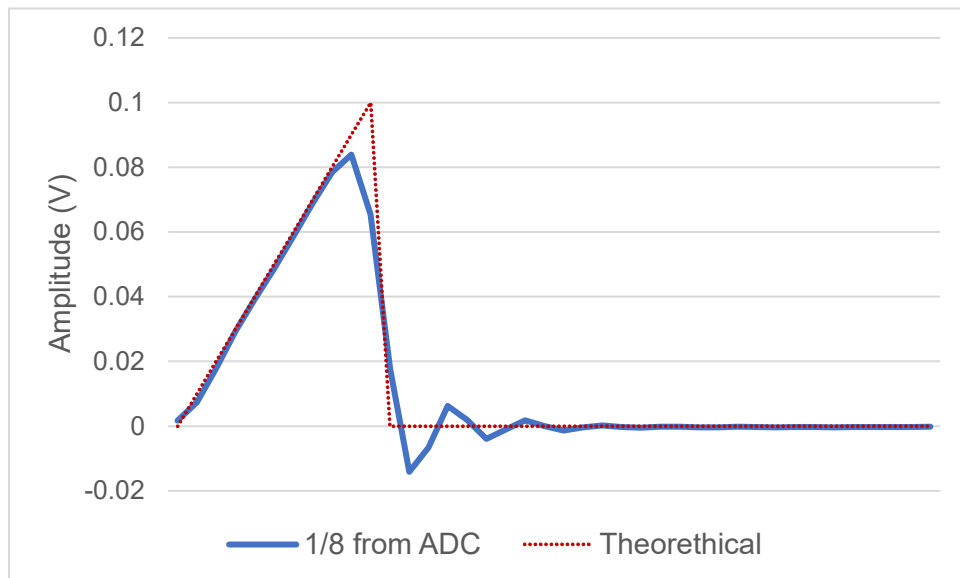


Figure 5.30: ADC “1/8 leading” sampled waveform zoom-in.

There is also an undershoot effect during the transition from i_{peak} to zero (Figures 5.29 and 5.30). This is related to the typical transient (or step) response of a FIR (finite

impulse response) filter implemented inside the $\Sigma - \Delta$ ADC for the decimation process. The undershooting (and/or overshooting) effect is known as the Gibbs phenomenon which is typical for the Fourier series, orthogonal polynomials, splines, wavelets, and other approximation functions [100], and it is sometimes produced by applying specific window functions (e.g. Keiser-Bessel) to a digital filter in order to truncate the theoretically infinite number of Fourier series to a finite number of terms [101].

The “Falling” test signals in Figure 5.31 exhibit a similar distortion and an overshooting effect following the transition from zero to i_{peak} (Figure 5.32), producing, as a result, sampled values above the reference (red dotted line) for the signals 1/2 and 1/4. Test signals 1/8 and 1/16 experience attenuation instead, despite the overshooting. This waveform distortion is reflected in the error plotted on Figures 5.25, 5.27 and 5.28.

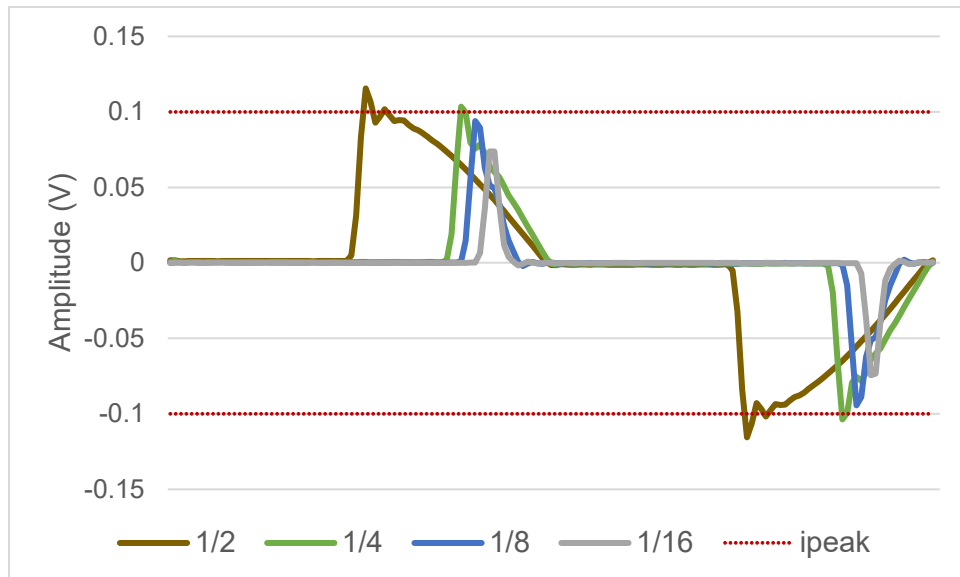


Figure 5.31: ADC “falling” sampled waveforms.

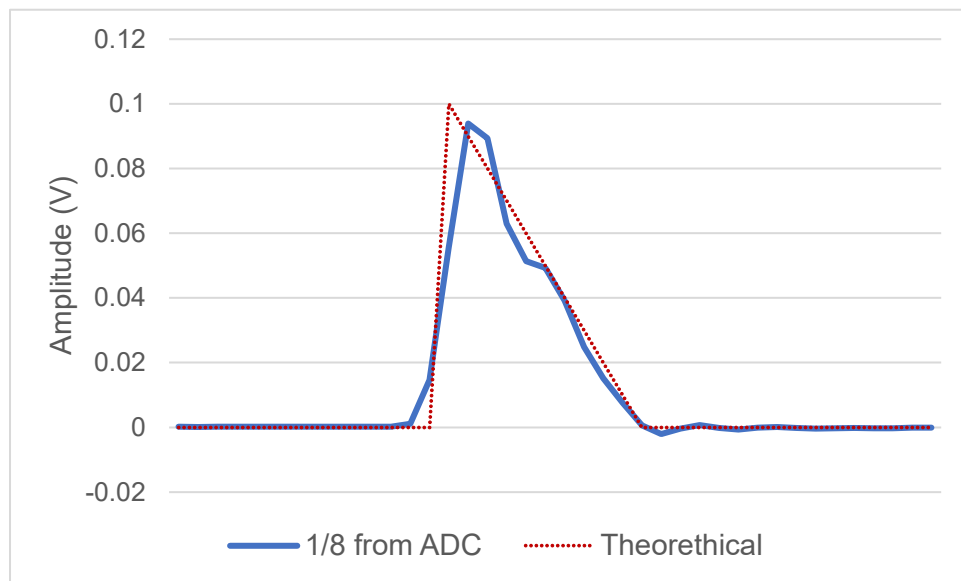


Figure 5.32: ADC “1/8 falling” sampled waveform zoom-in.

The Gibbs phenomenon is the limit reached by the FIR filter implemented in the $\Sigma - \Delta$ ADC due to test signals approximating to a transient and thus, is unavoidable. This effect is more noticeable for signals with transitions from peak value to zero (Figure 5.30) compared to signals with transitions from zero to a peak value (Figure 5.32).

Attenuation, on the other hand, is different for the leading and falling signals, but it consistently increases for signals with faster transitions (i.e. higher crest factor). The attenuation, produced during the analogue to digital conversion may be caused by the averaging performed inside the ADC’s $\Sigma - \Delta$ modulator or, more likely, due to the decimation (down-sampling) process.

Although $\Sigma - \Delta$ is the most common ADC architecture embedded in commercially available energy metering ICs due to the advantageous characteristics of the high resolution, differential inputs and a better common-mode noise rejection, compared to SAR ADCs, the restricted bandwidth of $\Sigma - \Delta$ converters produces measurement errors for fast-changing current signals which may contain harmonic components beyond the ADC’s input bandwidth (see Section 3.2.5). Thus, a new generation of metering IC’s should consider implementing high-performance SAR converters such as the device presented in Table 3.2 which would be capable of accurately measuring current signals

with fast transients.

5.5 Chapter Summary

In this chapter, the results from performed tests described in chapter 4 have been presented and discussed. It has been demonstrated that metering IC technology such as the revised ADE7878A can accurately estimate electrical parameters of sinusoidal signals and of nonsinusoidal signals with different harmonic content and phase angle values. The major cause of error for electricity measurements under sinusoidal conditions is produced by the power factor magnitude, related to the phase angle calculation. It has been demonstrated how a careful phase angle calibration could impact on the measurement error, particularly for the lower power factor signals.

Energy measurements of sinusoidal, standard nonsinusoidal and real-world current signal tests are within prescribed error limits of a “C” class accuracy meter, supporting the fact that deployed metering IC technology can effectively measure current signals with superimposed harmonic content.

The newly proposed crest factor tests results, however, exhibit a limitation in the ADE7878A IC to correctly calculate electrical quantities of signals with high crest factor values. This limitation is due to the digital filter response of ADE7878A ADC to fast-changing current signals which has been verified through the ADC waveform sampling IC capabilities. Moreover, erroneous calculations of the total active energy performed by the ADE7878A are caused by instantaneous measurements of high amplitude and low rms current signals, which contain high-order harmonics beyond the restricted bandwidth of the IC’s embedded $\Sigma - \Delta$ ADCs. The error produced during the current signal instantaneous measurement causes an overestimation of the total active energy for waveforms with a CF greater than 3 and a pronounced falling edge, such as those employed in the “leading” tests. This situation may be reflected in an increase of the electricity bill for customers with similar waveforms occurring at their premises. The following chapter provides further analysis and develops a new method to compensate for this critical aspect.

Chapter 6

Energy Measurements Error Compensation for Current Signals with High Crest Factor

Results from sinusoidal, standard nonsinusoidal and real-world nonsinusoidal tests reveal the generally high performance of the ADE7878A, under stated conditions, with relative errors lower than targeted 0.5% at I_{ref} and above. However, the Crest Factor tests produce larger relative errors that need to be compensated. Since the relative error and its increase or decrease (relative to the CF magnitude) differ among the leading and falling tests, they need to be separately analyzed. Furthermore, leading CF test signals have been found to produce larger relative errors compared to falling CF test signals and such errors cause an overestimation of the total active energy, i.e. an unfair increase in the customer's electricity bill.

In this chapter, an energy measurement error compensation method is described, based on the results presented in chapter 5 for the crest factor “leading” tests as an example of how electrical measurements of current signals with similar crest factor values can be compensated. Following a similar procedure, the IC model described in 4.4 has been modified in a way that the IC's measurement error can be predicted for a given CF magnitude and thus, compensated.

6.1 CF Measurement Error Compensation

From the results of “leading” crest factor tests, it can be noticed that an increase in the signal CF value is related to an increase in the ADE7878A’s measurement errors for revised electrical quantities i_{peak} , I_{rms} , E , E_S and E_1 . Furthermore, from the ADE7878A i_{peak} and I_{rms} measurements, CF can be calculated as per formula 2.28. The calculated CF_{meas} values are depicted in Table 6.1 and plotted against the real CF value in Figure 6.1.

Table 6.1: Crest factor measurements and its relative error for the “leading” CF tests.

| Signal | CF true value | CF_{meas} | CF_{meas} %error |
|--------------|---------------|-------------|--------------------|
| Leading 1/2 | 2 | 1.976 | -1.181 |
| Leading 1/4 | 3.319 | 3.088 | -6.972 |
| Leading 1/8 | 4.843 | 4.197 | -13.353 |
| Leading 1/16 | 6.91 | 5.384 | -22.082 |

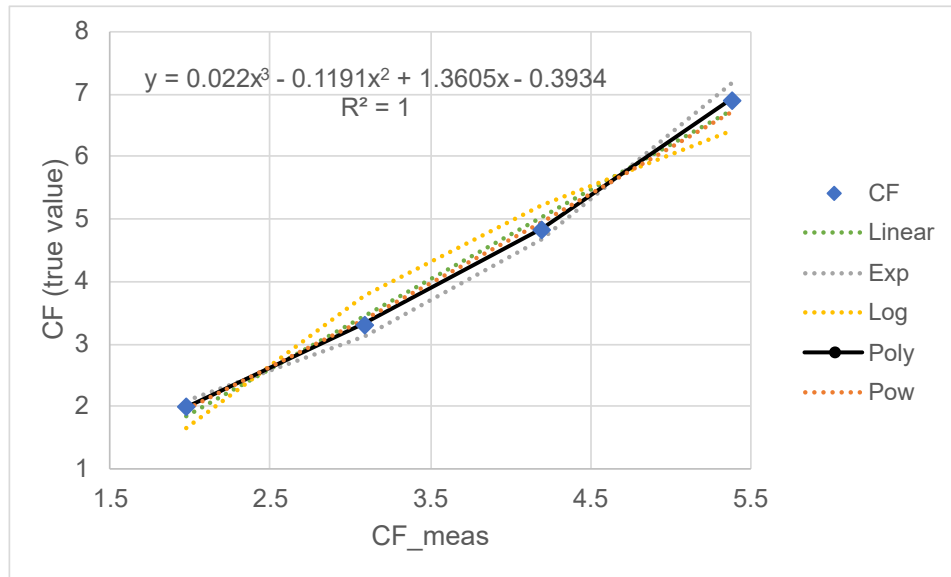


Figure 6.1: Calculated CF_{meas} values versus true CF values.

The graph displayed in Figure 6.1 shows the CF_{meas} values plotted versus the true CF values and different approximation curves intended to fit the data. The best fit for the data was obtained through a least squares polynomial regression and reveal a

Chapter 6. Energy Measurements Error Compensation for Current Signals with High Crest Factor

third-order polynomial relationship between CF calculations (i.e. CF_{meas}) and CF true value, which can be described as

$$CF = aCF_{meas}^3 + bCF_{meas}^2 + cCF_{meas} + d \quad (6.1)$$

where

CF is the crest factor true value

CF_{meas} is the CF measured value

a is a constant equal to 0.022

b is a constant equal to -0.1191

c is a constant equal to 1.3605

d is a constant equal to -0.3934

It is therefore possible to apply Equation 6.1 to the CF measured values (CF_{meas}) to obtain corrected CF values (CF_c) as follows:

$$CF_c = 0.022CF_{meas}^3 - 0.1191CF_{meas}^2 + 1.3605CF_{meas} - 0.3934$$

Results are presented in Table 6.2, including the CF_c relative error.

Table 6.2: Crest factor measurements compensation and its relative error.

| Signal | CF true value | CF_{meas} | CF_c | CF_c %error |
|---------------|----------------------|-------------|--------|---------------|
| Leading 1/2 | 2 | 1.976 | 2.000 | 0.004 |
| Leading 1/4 | 3.319 | 3.088 | 3.320 | 0.014 |
| Leading 1/8 | 4.843 | 4.197 | 4.845 | 0.026 |
| Leading 1/16 | 6.91 | 5.384 | 6.913 | 0.042 |

The relative error of CF_c is significantly reduced, compared with the CF_{meas} relative error, for leading signals, as can be seen in Figure 6.2.

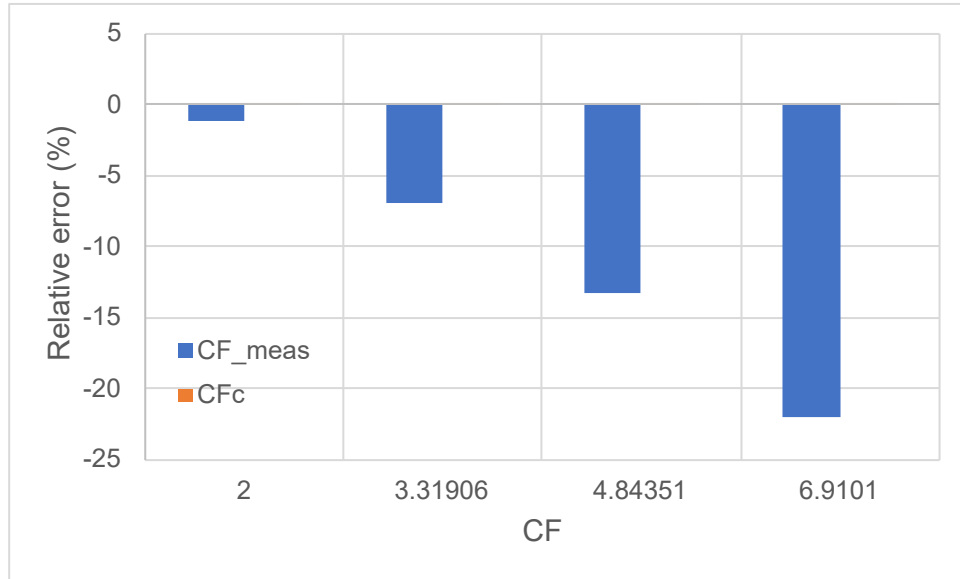


Figure 6.2: CF_{meas} and CF_c relative error.

6.2 Total Active Energy Measurement Error compensation

After correcting the CF measured values, a similar procedure can be followed to compensate the error in the total active energy E measurements. First, the required values for CF_c and the E relative error for the different CF value signals are given in Table 6.3.

Table 6.3: Total active energy measurement error.

| Signal | CF_c | $E_{truevalue}$ | E_{meas} | E_{meas} %error |
|--------------|--------|-----------------|------------|-------------------|
| Leading 1/2 | 2.000 | 606.308 | 608.003 | 0.279 |
| Leading 1/4 | 3.320 | 150.754 | 151.924 | 0.776 |
| Leading 1/8 | 4.845 | 35.875 | 36.709 | 2.325 |
| Leading 1/16 | 6.913 | 7.548 | 8.13 | 7.09 |

After applying a least squares polynomial regression, a third-order polynomial relationship between the CF_c and the E_{meas} relative error was found as the best fit to the data, which can be observed in Figure 6.3 along with different curve approximations to compare. The third-order polynomial relationship can be expressed as

Chapter 6. Energy Measurements Error Compensation for Current Signals with High Crest Factor

$$E_{re} = aCF_c^3 + bCF_c^2 + cCF_c + d \quad (6.2)$$

where

E_{re} is the predicted total active energy E measurement relative error

CF_c is the corrected CF value

a is a constant equal to 0.0443

b is a constant equal to -0.2257

c is a constant equal to 0.6179

d is a constant equal to -0.4079

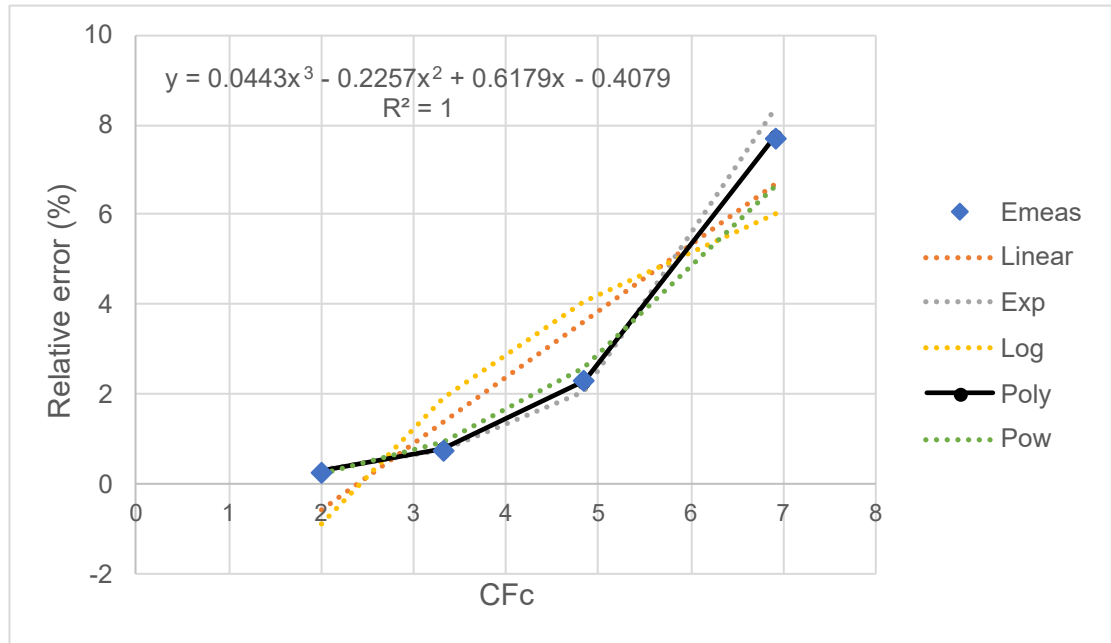


Figure 6.3: CF_c versus E relative error.

E_{re} becomes a predicted E measured (E_{meas}) relative error for a given CF_c value, which can be used to estimate a corrected E_{meas} values by means of re-arranging Equation 2.29 as follows:

$$E_c = \frac{E_{meas}}{\frac{E_{re}}{100} + 1} \quad (6.3)$$

Chapter 6. Energy Measurements Error Compensation for Current Signals with High Crest Factor

where

E_c is the total active energy E corrected value

E_{meas} is the total active energy E measured value

E_{re} is the predicted total active energy E relative error

The results from applying Equation 6.3 are presented in Table 6.4, including E_c relative error.

Table 6.4: Total active energy compensated measurement error.

| Signal | E | E_{meas} | E_c | E_{meas} %error | E_c %error |
|--------------|---------|------------|---------|-------------------|--------------|
| Leading 1/2 | 606.308 | 608.003 | 606.329 | 0.279 | 0.004 |
| Leading 1/4 | 150.754 | 151.924 | 150.732 | 0.776 | -0.015 |
| Leading 1/8 | 35.875 | 36.709 | 35.891 | 2.325 | 0.045 |
| Leading 1/16 | 7.548 | 8.13 | 7.546 | 7.09 | 0.028 |

The relative error in total active energy measurements has been significantly reduced as can be seen in Figure 6.4.

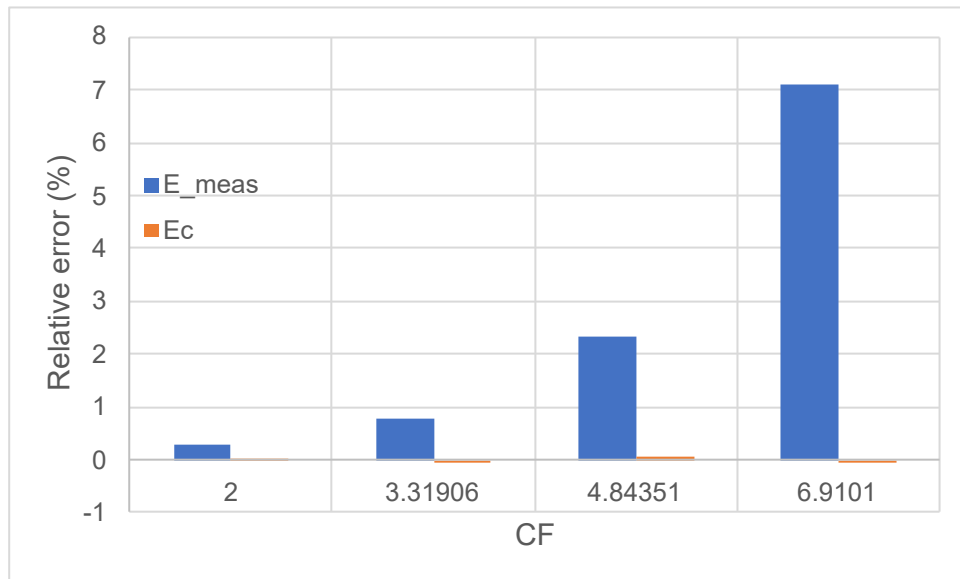


Figure 6.4: E_{meas} and E_c relative error.

6.3 Total Apparent Energy Measurement Error Compensation

Following the same methodology, it is possible to compensate the error for total apparent energy E_S measurements. In Table 6.5, the values of $E_{S_{meas}}$ (i.e. measured E_S values), E_S (true value) and $E_{S_{meas}}$ relative error are presented.

Table 6.5: Total apparent energy measurement error.

| Signal | CF_C | E_S true value | $E_{S_{meas}}$ | E_{meas} % error |
|--------------|--------|------------------|----------------|--------------------|
| Leading 1/2 | 2.000 | 880.901 | 876.013 | -0.555 |
| Leading 1/4 | 3.320 | 535.639 | 527.093 | -1.595 |
| Leading 1/8 | 4.845 | 370.279 | 357.873 | -3.35 |
| Leading 1/16 | 6.913 | 254.619 | 237.29 | -6.806 |

The graph plotted in Figure 6.5 reveals a second-order polynomial relationship between the $E_{S_{meas}}$ relative error and the CF_C value, which was obtained through a polynomial least squares regression. In Figure 6.5, the linear and logarithmic approximation curves are plotted as a way of comparison to the polynomial data fitting.

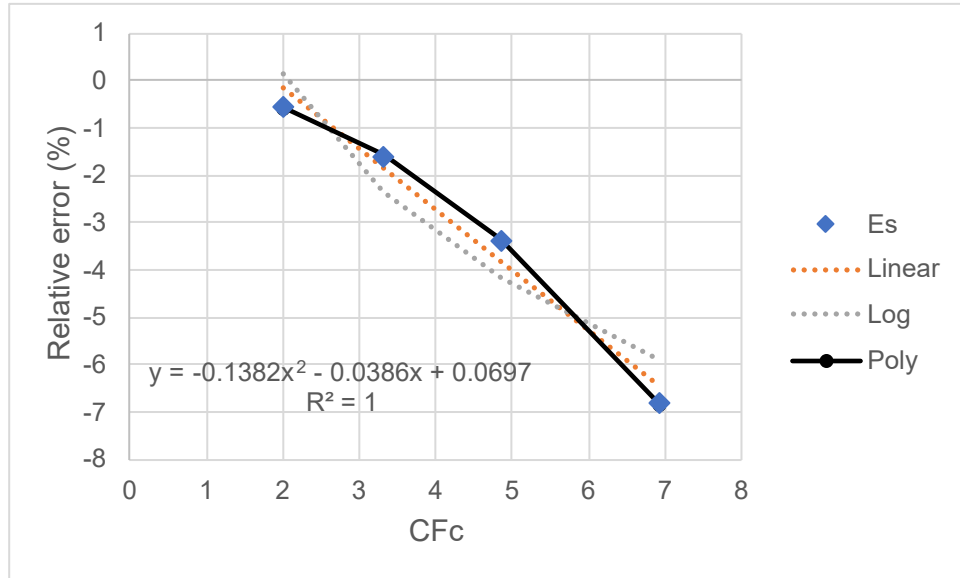


Figure 6.5: CF_C versus $E_{S_{meas}}$ relative error.

The relationship between CF_C and $E_{S_{meas}}$ relative error can be expressed as

Chapter 6. Energy Measurements Error Compensation for Current Signals with High Crest Factor

$$E_{Sre} = aCF_C^2 + bCF_C + c \quad (6.4)$$

where

E_{Sre} is the predicted E_S relative error for a given CF_C value

CF_C is the corrected crest factor value

a is a constant equal to -0.1382

b is a constant equal to -0.0386

c is a constant equal to 0.0697

Re-arranging Equation 2.29, the E_S measured value can be compensated as follows

$$E_{Sc} = \frac{E_{Smeas}}{\frac{E_{Sre}}{100} + 1} \quad (6.5)$$

where

E_{Sc} is the total apparent energy E_S corrected value

E_{Smeas} is the total apparent energy E_S measured value

E_{Sre} is the predicted total apparent energy E_S relative error

The results from applying Equation 6.5 to measured E_S values are presented in Table 6.6.

Table 6.6: Total active energy compensated measurement error.

| Signal | E_S | E_{Smeas} | E_{Sc} | E_{Smeas} %error | E_{Sc} %error |
|---------------|---------|-------------|----------|--------------------|-----------------|
| Leading 1/2 | 880.901 | 876.013 | 881.029 | -0.555 | 0.015 |
| Leading 1/4 | 535.639 | 527.093 | 535.523 | -1.595 | -0.022 |
| Leading 1/8 | 370.279 | 357.873 | 370.285 | -3.35 | 0.002 |
| Leading 1/16 | 254.619 | 237.29 | 254.652 | -6.806 | 0.013 |

The graph in Figure 6.6 shows how the total apparent energy measurement relative error has been significantly reduced.

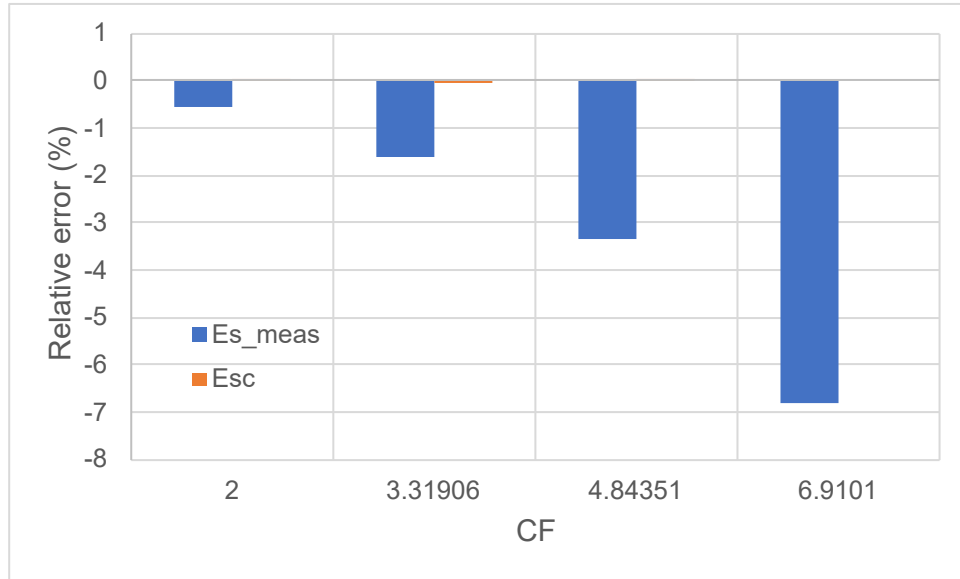


Figure 6.6: $E_{S_{meas}}$ and E_{Sc} relative error.

6.4 Fundamental Active Energy Measurement Error Compensation

The fundamental energy measurements E_1 can be compensated following the same procedure as has been done for E and E_S . In Table 6.7, the fundamental energy E_1 true values, the fundamental energy measured (E_{1meas}) values, and the E_{1meas} relative error are presented.

Table 6.7: Fundamental active energy measurement error.

| Signal | CF_C | E_1 true value | E_{1meas} | E_{1meas} % error |
|--------------|--------|------------------|-------------|---------------------|
| Leading 1/2 | 2.000 | 627.912 | 622.166 | -0.915 |
| Leading 1/4 | 3.320 | 164.73 | 159.79 | -2.999 |
| Leading 1/8 | 4.845 | 43.155 | 41.004 | -4.984 |
| Leading 1/16 | 6.913 | 11.054 | 10.183 | -7.876 |

The graph plotted in Figure 6.7 reveals a third-order polynomial relationship between the E_{1meas} relative error and the CF_C value, obtained through a least squares polynomial regression, as the best fit for the data. The linear and logarithmic approximation curves are included in Figure 6.7 for comparison to the polynomial data fit.

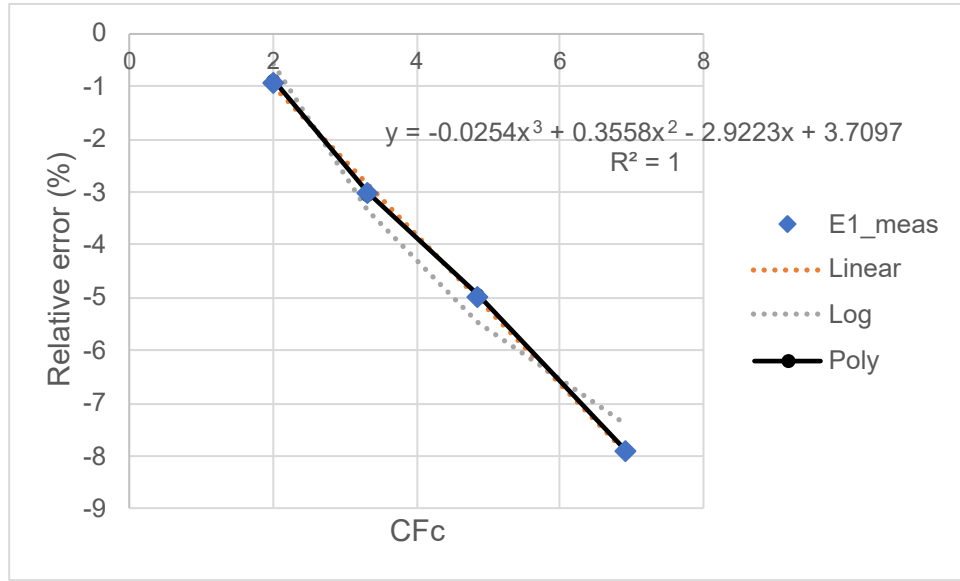


Figure 6.7: E_{1meas} relative error versus CF_C .

The relationship between CF_C and E_{1meas} relative error can be expressed as

$$E_{1re} = aCF_C^3 + bCF_C^2 + cCF_C + d \quad (6.6)$$

where

E_{1re} is the predicted E_1 relative error for a given CF_C value

CF_C is the corrected crest factor value

a is a constant equal to -0.0254

b is a constant equal to 0.3558

c is a constant equal to -2.9223

d is a constant equal to 3.7097

E_{1re} becomes a predicted E_{1meas} relative error for a given CF_C value, which can be used to estimate compensated E_{1c} values by means of re-arranging equation 2.29 as follows:

$$E_{1c} = \frac{E_{1meas}}{\frac{E_{1re}}{100} + 1} \quad (6.7)$$

Chapter 6. Energy Measurements Error Compensation for Current Signals with High Crest Factor

where

E_{1c} is the fundamental active energy E_1 corrected value

E_{1meas} is the fundamental active energy E_1 measured value

E_{1re} is the predicted fundamental active energy E_1 relative error

The results from applying the formula are presented in Table 6.8, including E_{1c} relative error.

Table 6.8: Fundamental active energy compensated measurement error.

| Signal | E_1 | E_{1meas} | E_{1c} | E_{1meas} %error | E_{1c} %error |
|--------------|---------|-------------|----------|--------------------|-----------------|
| Leading 1/2 | 627.912 | 622.166 | 627.790 | -0.915 | -0.019 |
| Leading 1/4 | 164.73 | 159.79 | 164.797 | -2.999 | 0.041 |
| Leading 1/8 | 43.155 | 41.004 | 43.138 | -4.984 | -0.039 |
| Leading 1/16 | 11.054 | 10.183 | 11.055 | -7.876 | 0.008 |

The relative error in total active energy measurements has been significantly reduced as can be seen in Figure 6.8.

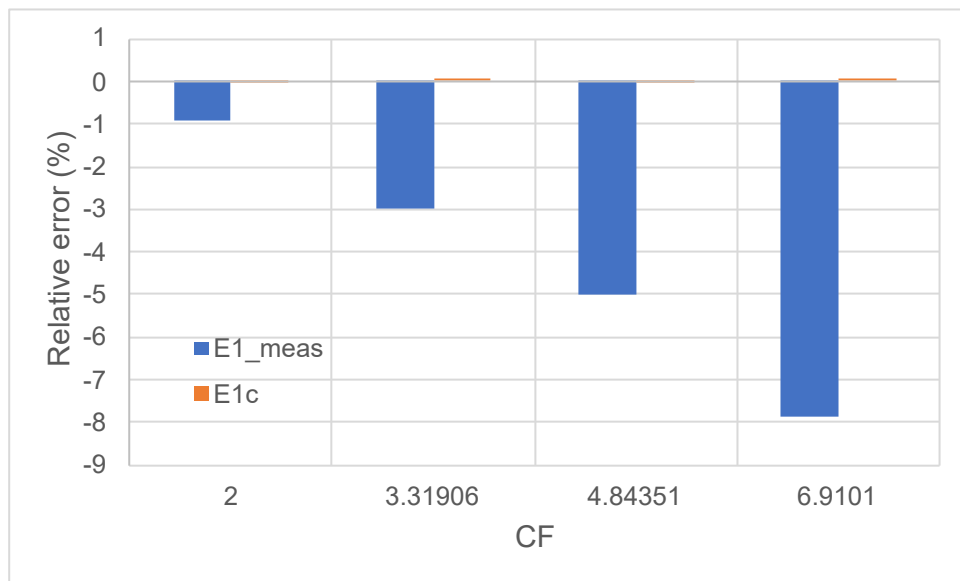


Figure 6.8: E_{1meas} and E_{1c} relative error.

6.5 ADE7878A IC model measurement error estimation for high crest factor current signals

The IC model described in Section 4.4 has been modified to include implementation of formulas 6.1 to 6.7, described in previous sections from this chapter, to predict measurement values of CF_{meas} , E_{meas} , E_{Smeas} and E_{1meas} quantities for CF current signals, which are expected to be similar to the real ADE7878A measurements. These predicted measurement values are useful to estimate relative errors produced by current signals with a given CF value. Figure 6.9 shows the updated IC model block diagram.

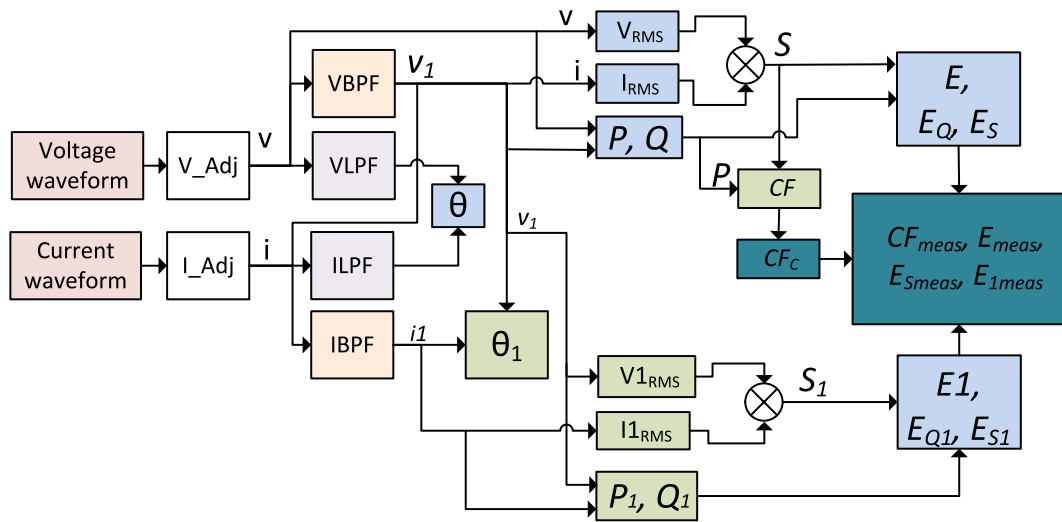


Figure 6.9: Modified ADE7878A IC model functional block diagram (single-phase).

The teal colored blocks in Figure 6.9 perform calculations to obtain compensated measurement values of CF (CF_C), and estimated measured values of total active energy (E_{meas}), total apparent energy (E_{Smeas}) and fundamental active energy (E_{1meas}) as has been described in the previous sections.

6.6 Applying Error Compensation to ADE7878A IC Measurements of High Crest Factor Current Signals

Equations 6.1 to 6.7 have been implemented in the LabVIEW code used to communicate and collect data from the ADE7878A IC, in order to compensate measurement errors for current signals with CF values greater than 3. The reason to take a $CF > 3$ as a threshold to apply measurement compensation is because it has been observed from the results of chapter 5 and from the literature [75], that signals with lower values of CF do not cause significant error to measured electrical quantities. This threshold, however, could be changed to meet any other criteria based on further crest factor testing results. In Figure 6.10 the simplified error compensation flow diagram is presented.

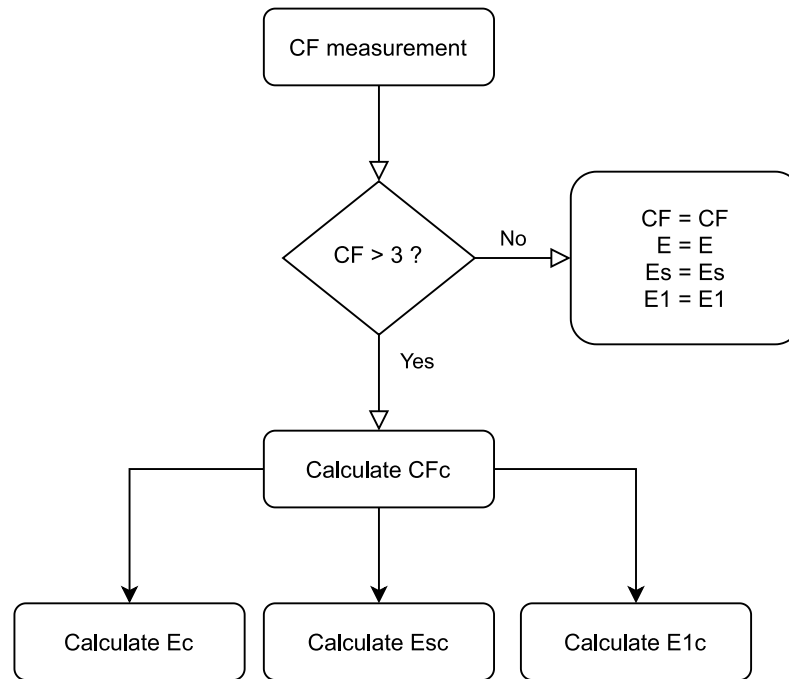


Figure 6.10: Measurement error compensation flow diagram.

6.7 Recommendations for Electricity Meter Designers

The current signal CF is the waveform parameter identified as the largest contributor to electricity meter error, as has been demonstrated in chapter 5. Inside the meter, the

Chapter 6. Energy Measurements Error Compensation for Current Signals with High Crest Factor

response to fast-changing current signals is limited by metering IC digital components such as digital filters which can not be avoided, unless deployed ICs could be replaced by improved metering IC technology. However, by means of characterizing the metering IC response to such signals, the measurement error of signals with a large CF could be mitigated following the procedure described in Sections 6.1 to 6.4. This measurement error compensation is not computationally expensive and therefore represents a solution to prevent large energy metering errors from existing deployed static meters exposed to high CF current signals.

Furthermore, the tests to characterize electricity meter response to fast-changing signals such as the proposed crest factor tests (see 4.2.4) may include voltage and current transducers to fully compensated errors introduced by a particular sensing technology due to the CF magnitude.

6.8 Chapter Summary

In this chapter, a novel procedure to compensate metering errors caused by current signals with CF values higher than 3 has been proposed. To effectively mitigate the effects of fast-changing signals performed by electricity meters it is important to characterize the metering IC response to different magnitudes of CF values.

Because electricity meters can measure some nonsinusoidal signals within specified accuracy class limits, it is desirable to find a CF threshold value to apply error compensation to measurements, depending on the meter response evaluated during crest factor testing.

Error compensation can be applied to already deployed meters by means of a software/firmware upgrade without the need of replacing any physical components. This work therefore enables a convenient and low cost solution to upgrade new and existing meters to deliver comprehensive resilience to even extreme levels of fast-changing and nonsinusoidal distortion.

The metering IC model, updated with error compensation is a useful tool to predict measuring errors of deployed static meters for a given CF signal magnitude.

Chapter 7

Conclusions and Future Work

7.1 Conclusions

The accuracy of electricity meters under nonsinusoidal conditions is an important topic for academia, industry and electricity consumers. Being a fundamental component of the upcoming smart grid, thought to provide electrical energy consumption information as well as other electrical quantities, an accurate response of SEMs to present and future power network conditions must be assured. In this regard, numerous studies have been conducted in order to identify the causes of erroneous measurements reported by SEM when exposed to nonsinusoidal voltage and current signals, but there is a gap in these studies relating to nonsinusoidal signals.

This thesis addresses this gap by providing a clear understanding of SEM response to nonsinusoidal fast-changing current signals from typical power electronic equipment in modern grids. The thesis has proposed a methodology, including a set of waveforms with fast-changing waveform phenomena, which exposes limitations in energy metering IC technology when calculating the total active energy and other electrical quantities.

Chapter 1 presented challenges for electricity meters due to the dynamic power quality scenario of modern power grids. A large number of non-linear loads which could highly distort the current and voltage waveforms are already present in home and industry premises and this number is expected to grow in the near future with the adoption of energy saving devices and the proliferation of electrical chargers for vehicles.

Some of these non-linear loads produce fast-changing current waveforms which causes error in the total active energy calculations performed by SEMs.

Chapter 2 gives an overview and analysis of accuracy requirements for SEM prescribed by the standards and metrology organizations. The methodology to calculate error in electricity meters, according to the normative has been reviewed and suitable definitions of electrical quantities for energy meters under nonsinusoidal conditions have been provided.

A typical SEM design has been analyzed in detail in Chapter 3, including comments and recommendations for the selection of appropriate analogue front-end components and signal processing techniques. The internal design of commercially available energy metering IC technology, commonly used as the metrology engine for SEMs, is also investigated and a comparison of energy metering ICs from different vendors is given.

In Chapter 3, a review of electricity meter errors reported in the literature is presented. The most significant results and the methodologies employed by these studies are highlighted. Proposals to calibrate SEMs under nonsinusoidal waveform conditions are analysed and two major issues to perform such calibration in a standardized way have been identified: 1) finding a truly representative “real-world” set of nonsinusoidal test signals and 2) SEM respond differently to nonsinusoidal signals, depending on the meter design and components.

Having established that SEM are prone to large errors when some nonsinusoidal signals exist and that this error depends on SEM components, in Chapter 4 a set of tests for sinusoidal and nonsinusoidal conditions is proposed to evaluate the response of commercially available energy metering ICs exposed to different power network scenarios. A novel model of a metering IC has been implemented in LabVIEW software as a tool to predict the IC response to signals of different characteristics. The measurement system and the IC model are described and a generic methodology to evaluate IC response to nonsinusoidal signals has been presented. Particular attention has been given to signals with high slope and crest factor values which are known to cause significant error in SEMs. The proposed “crest factor tests” signals have been designed to evaluate the response of the IC to such signals.

The results from the proposed tests are reported and discussed in Chapter 5, showing that present metering IC technology can measure nonsinusoidal signals with good accuracy, i.e. with relative errors within standards requirements. The limitations found in the results from the performed tests are mostly related to the restricted bandwidth of $\Sigma - \Delta$ ADCs within energy metering ICs and to the Gibbs phenomenon which produces overshooting and undershooting effects in the vicinity of a signal with fast amplitude changes such as the proposed crest factor test waveforms. It has been demonstrated that it is possible to find both positive and negative relative errors for any particular measured quantity, depending on a combination of factors like the signal slope, the sign of power factor and the crest factor magnitude. This seemingly inconsistent result is caused by the waveform profile and has a strong relationship to the phase angle between the voltage and current signals.

From the crest factor test results, the following conclusions can be made:

- For any particular transient occurring in a waveform, a negative-going transition produces larger relative error in the $\Sigma - \Delta$ ADC compared to positive-going transitions.
- The accuracy of the I_{rms} measurements degrades as the signal slope increases, causing a similar magnitude of error in the apparent energy E_S .
- Relative errors in total active energy E and fundamental active energy E_1 calculations are produced during the instantaneous current measurements.
- The phase angle between the voltage and current signal strongly affects the accuracy of the IC measurements, becoming, in general, less accurate at lower power factors.

In Chapter 6, a novel methodology to compensate metering errors caused by current signals with high crest factor values has been proposed, which significantly reduces errors in reported measurements. This methodology is based on the results from the crest factor tests and can be applied to already deployed static meters.

An important contribution of this thesis is the detailed investigation of the impact of crest factor and signal slope. The proposed crest factor tests push the metering IC capabilities to the limit and could be used as a starting point to define standard tests for evaluating the accuracy of SEMs and current transducers exposed to fast-changing currents.

7.2 Future Work

The work presented in this thesis analyses the response of one particular and representative commercial metering IC to various nonsinusoidal signals and proposed a measurement error compensation method for signals with a CF greater than 3. This error compensation method, however, is proposed based only on the results reported in Chapter 5 for the tests described in Chapter 4. Due to many variables which could be found in deployed SEMs such as different transducers, measurement algorithms, and a virtually infinite number of waveforms with a CF greater than 3, the following limitations have been recognized for the proposed error compensation method:

1. The transducer's response to current signals of high crest factor values has not been evaluated and thus, it is not considered by the error compensation method.
2. A selection of waveforms with CF values equal to or greater than 3 has been tested in the metering IC and in the model described in Chapter 4, but there is value in testing a wider range of highly distorted waveforms.
3. Only one metering IC from a single vendor has been tested and modelled in this work.
4. The correction method is based on waveforms with a negative-going transition which causes the most significant errors and are the most commonly found in real power networks due to dimming devices [94].

To overcome the aforementioned limitations, further testing and analysis is required as described in the following subsections.

7.2.1 Analysis of the Effect of Signal Parameters in Voltage and Current Transducers Accuracy

In this thesis, the error introduced by the voltage and current transducers has been neglected in order to evaluate only the error produced inside the energy metering IC. However, voltage and current transducers of different operational principles are used by deployed SEMs, so their response to nonsinusoidal signals should be assessed. It is important to know and understand the effects of signals with fast amplitude changes in the accuracy of transducers of different nature, such as resistives (RVD, shunt resistor), inductives (VTs and CTs) or current derivatives (Rogowski coil, Hall-effect). All these types of sensors/transducers are used in certified SEMs (for sinusoidal conditions), but all of them could behave differently when the waveform is nonsinusoidal, due to their different operational principles.

7.2.2 Analysis of the Effect of Signal Parameters in Metering IC Digital Integrators

Current derivative sensors such as Rogowski coils output a voltage proportional to the rate of change of current ($\frac{dI(t)}{dt}$) in a conductor, so an integrator is needed to obtain a voltage proportional to the current $I(t)$. Although commercially available Rogowski coils could incorporate an analogue integrator in the same package, energy metering ICs often include a digital integrator for a direct connection to Rogowski coils. While a digital integrator could have benefits than its analogue version (i.e. more accurate and stable output [102]), digital integrators could exhibit the Gibbs phenomenon for signals with a high crest factor and short transition duration. It is also important to evaluate if the phase angle of nonsinusoidal signals significantly add to the metering IC error when Rogoski coils are employed and, if that is the case, to analyse why this behavior occurs.

7.2.3 Further Evaluation of the Effect of Different Values of Signal Slope in Metering IC Accuracy

In Chapter 4, a set of waveforms called “crest factor test” was proposed to evaluate the response of a metering IC to fast-changing currents, by means of adjusting parameters like I_{peak} and CF . These waveforms have proved to be useful to assess the IC’s metering errors, but it would be ideal to include more test signals with different values of waveform slope (i.e. higher CF value) in order to select optimal slope test point values. The same signals could be also injected to the IC at different current values other than I_{ref} for a more detailed investigation.

7.2.4 Refinement of Metering IC Model

Chapter 5 presented results of IC measurements in terms of relative error, which has been compared to theoretically calculated values. These results have been also validated in a metering IC model built in LabVIEW software as a useful tool to predict the IC output. However, the model requires manual input of some parameters which could be automatically calculated by the same model and then fed back to the parameter inputs. Future work in this model should include full and convenient control of IC parameters, and offer adjustment to cater for other IC vendors.

7.2.5 Determine a suitable crest factor threshold for measurement error compensation

In Chapter 6, a crest factor value of $CF > 3$ was defined as a threshold to apply the proposed measurement error compensation technique. This threshold was selected based on the results from performed crest factor tests, under stated conditions. However, further testing is needed to determine an optimal CF threshold for error compensation. This can be achieved by means of including current signals of different CF magnitudes. Furthermore, this threshold value is likely to differ for various metering IC models from a single vendor and also among ICs from different vendors. Thus, the characterization of metering IC response to high CF values is desirable to be performed during SEM

Chapter 7. Conclusions and Future Work

calibration, and the development of a future standard is required to enforce this.

Appendix A

Total Apparent Power S Decomposition

Traditional Power Triangle

The power triangle on figure A.1 is well known among the electrical scientific community and have been widely used in the literature to illustrate traditional apparent power S decomposition. From this perspective, the total apparent power S is composed by two powers: total active power P and reactive power Q . This decomposition and its representation only holds for pure sinusoidal signals.

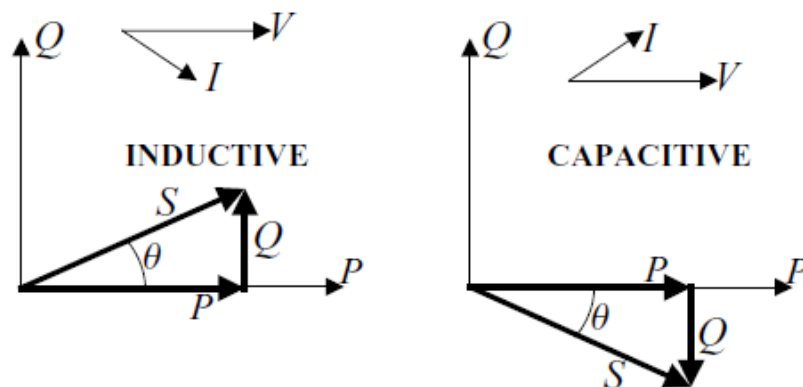


Figure A.1: Traditional power triangle.

IEEE 1459 Total Apparent Power decomposition

IEEE 1459 standard establishes the total apparent power decomposition (Figure A.2) originally proposed by Alexander Eigeles Emanuel [32].

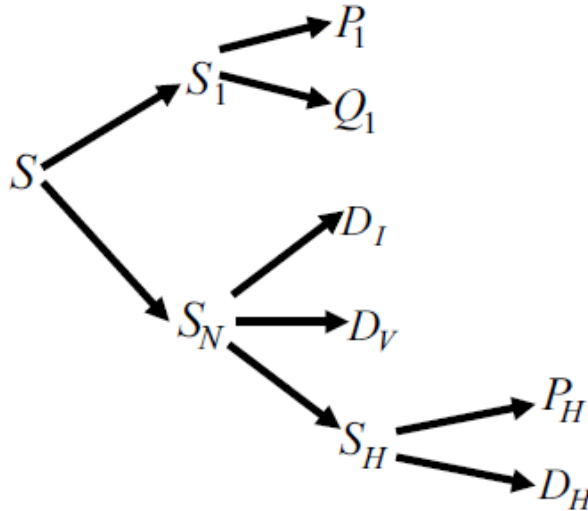


Figure A.2: IEEE 1459 total apparent power S decomposition.

According to IEEE 1459 [20], the total apparent power S is firstly composed by fundamental apparent power S_1 and the fundamental nonactive power S_N . Then, S_1 and S_N are composed by different power quantities that could be observed in figure A.2.

Geometrical representations of IEEE 1459 Total Apparent Power decomposition are depicted in figures A.3, A.4 and A.5. These geometrical representations has been replicated from [35].

Figure A.3 shows a representation of S decomposition which holds for typical real-world power system conditions like sinusoidal, nonsinusoidal, balanced and unbalanced.

Appendix A. Total Apparent Power S Decomposition

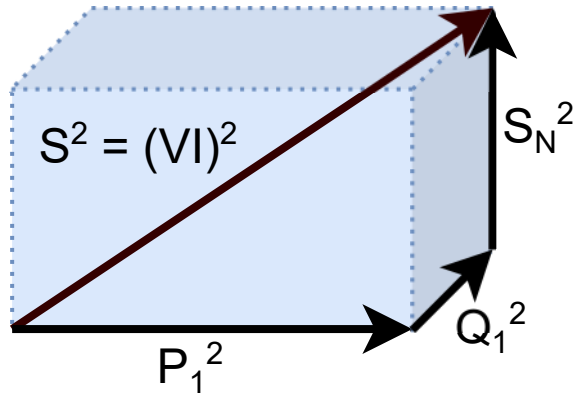


Figure A.3: IEEE 1459 total apparent power S decomposition: geometrical representation.

Figure A.4 represent the ideal case of a perfect sinusoidal and balanced power grid situation, when distortion does not exist and the nonactive apparent power S_N is equal to zero. Thus, only fundamental quantities P_1 and Q_1 shape S .

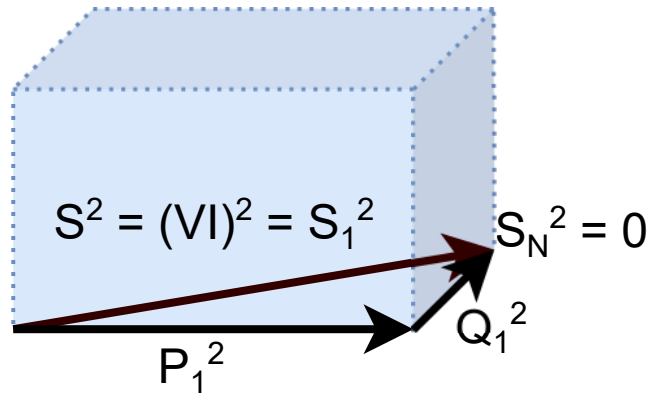


Figure A.4: IEEE 1459 total apparent power S decomposition: geometrical representation of a sinusoidal case.

In figure A.5, a geometrical representation of the nonactive apparent power S_N components is presented. The quantities D_I , D_V and S_H have been defined and could be revised in chapter 2, subsection 2.2.2.

Appendix A. Total Apparent Power S Decomposition

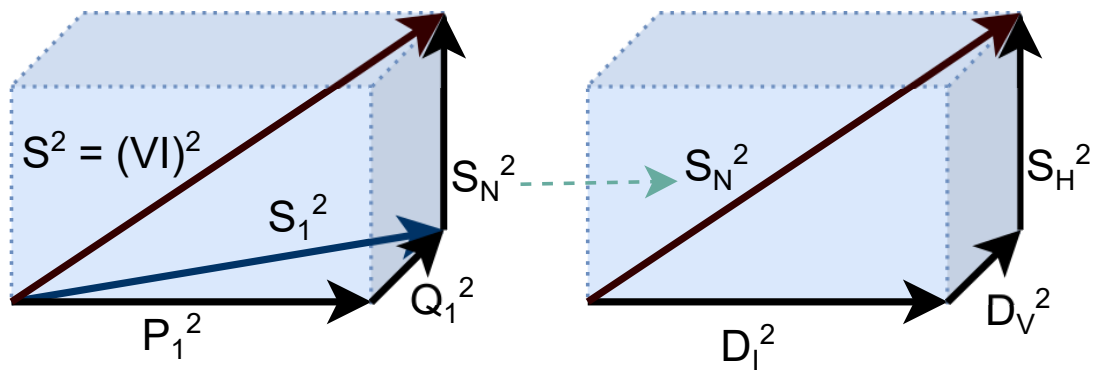


Figure A.5: IEEE 1459 nonactive apparent power S_N decomposition: geometrical representation.

Appendix B

Rated Operating Accuracy Test Conditions

To test the accuracy requirements, the following conditions shall be maintained:

- a) the meter shall be tested in its case with the cover in position; all parts intended to be earthed shall be earthed;
- b) before any test is made, the circuits shall have been energized for a time sufficient to reach thermal stability;
- c) in addition, for polyphase meters:
 - the phase sequence shall be as marked on the diagram of connections;
 - the voltages and currents shall be substantially balanced (see Table B.1).
- d) the reference conditions are given in table B.2;
- e) for requirements regarding test stations, see IEC 60736.

Appendix B. Rated Operating Accuracy Test Conditions

Table B.1: Voltage and current balance.

| Polyphase meters | Accuracy class | | | |
|---|----------------|-----------|-----------|-----------|
| | A | B | C | D |
| Each of the voltages between phase and neutral and between any two phases shall not differ from the average corresponding voltage by more than | $\pm 1\%$ | $\pm 1\%$ | $\pm 1\%$ | $\pm 1\%$ |
| Each of the currents in the conductors shall not differ from the average current by more than | $\pm 2\%$ | $\pm 2\%$ | $\pm 1\%$ | $\pm 1\%$ |
| The phase displacement of each of these currents from the corresponding phase to neutral voltage, irrespective of the phase angle, shall not differ from each other more than | $\pm 2\%$ | $\pm 2\%$ | $\pm 1\%$ | $\pm 1\%$ |

Table B.2: Reference conditions.

| Influence quantity | Reference value | Permissible tolerances for accuracy class | | | |
|-----------------------------------|--|---|-----------------------|-----------------------|-----------------------|
| | | A | B | C | D |
| Ambient temperature | Reference temperature or, in its absence, 23°C | $\pm 2^\circ\text{C}$ | $\pm 2^\circ\text{C}$ | $\pm 2^\circ\text{C}$ | $\pm 2^\circ\text{C}$ |
| Voltage | Reference voltage | $\pm 1\%$ | $\pm 1\%$ | $\pm 1\%$ | $\pm 1\%$ |
| Frequency | Reference frequency | $\pm 0.5\%$ | $\pm 0.3\%$ | $\pm 0.3\%$ | $\pm 0.3\%$ |
| d.c., even, odd and sub-harmonics | Sinusoidal voltages and currents | Distortion factor less than: | | | |
| | | $\pm 3\%$ | $\pm 2\%$ | $\pm 2\%$ | $\pm 2\%$ |

Appendix C

ADE7878A Calibration

To calibrate the metering IC, the procedure described in [103] has been followed using the “accurate source method”, i.e. supposing that the AWG can provide exact voltages and currents. The readings of the ADE7878A in calibration are compared against expected values, and the quantities to calibrate are adjusted accordingly. A full calibration of the IC should be performed including:

- V_{rms} and I_{rms} , (gain and offset compensation);
- P , Q , S , E_1 E_{Q_1} (gain and offset compensation);
- phase delay compensation.

Before starting the calibration, the voltage and current full scale and nominal values have to be defined. The defined values are depicted in Table C.1.

Table C.1: Definitions of meter quantities for calibration.

| Quantity | Symbol | Value | AWG output |
|--------------------|-----------|---------------|------------|
| Full scale voltage | V_{FS} | $389 V_{rms}$ | 1000 mVpp |
| Nominal voltage | V_N | $230 V_{rms}$ | 590 mVpp |
| Minimum Voltage | V_{min} | 230 V | 590 mVpp |
| Full scale current | I_{FS} | 100 A | 1000 mVpp |
| Nominal current | I_N | 20 A | 200 mVpp |
| Minimum current | I_{min} | 1 A | 10 mVpp |

Appendix C. ADE7878A Calibration

As a part of the ADE7878A configuration, the *VLEVEL* internal register needs to be initialized as follows:

$$VLEVEL = \frac{V_{FS}}{V_N} \times 491520 \quad (C.1)$$

$$VLEVEL = \frac{389}{230} \times 491520 = 831310 = 0x000CAFAE$$

rms gain calibration

To calibrate the voltage and current rms values, the *Vrms_{ref}* and *Irms_{ref}* values needs to be calculated as follows:

$$Vrms_{ref} = round\left(\frac{V_N}{V_{FS}} \times 4191910\right) \quad (C.2)$$

where the 4191910 number is the ideal rms value computed by the ADE7878A when the inputs are at full scale

$$Vrms_{ref} = round\left(\frac{230}{389} \times 4191910\right) = 2478507$$

and

$$Irms_{ref} = round\left(\frac{I_N}{I_{FS}} \times 4191910\right) \quad (C.3)$$

$$Irms_{ref} = round\left(\frac{20}{100} \times 4191910\right) = 838382$$

Now, the voltage and current gain can be calibrated following the procedure described below:

- a) Supply the ADE7878A with a nominal current, nominal voltage and a power factor of 1.
- b) Enable the zero crossing interrupts and read the voltage or current rms values when the interrupt is triggered for multiple times and average them. Let this

Appendix C. ADE7878A Calibration

average be RMS .

- c) Decide the desired rms representation for the nominal voltage or current. Let it be RMS_{REF}

The voltage gain $VGAIN$ and the current gain $IGAIN$ calibrated values are the signed 24-bit hexadecimal representation of:

$$VGAIN = \frac{RMS_{REF}}{RMS} - 1 \quad (C.4)$$

$$VGAIN = \frac{230}{229.5617} - 1 = 0.0019$$

where 229.5617 is the average of 1024 voltage rms measurements from the ADE7878A as per step 2

$$VGAIN = 0.0019 \times 2^{23} = 15938 = 0x00003E42$$

and

$$IGAIN = \frac{RMS_{REF}}{RMS} - 1 \quad (C.5)$$

$$IGAIN = \frac{20}{81.7186} - 1 = -0.75525269$$

where 81.7186 is the average of 1024 current rms measurements from the ADE7878A as per step 2.

$$IGAIN = -0.75525269 \times 2^{23} = -6335561 = 0xFF9F53B7$$

rms offset calibration

The rms offset calibration compensate the d.c. offsets produced by the noise in the current and voltage channels. The compensation procedure is as follows:

- a) Supply the ADE7878A with a nominal voltage or current signal.

Appendix C. ADE7878A Calibration

- b) Enable the zero crossing interrupts and read the voltage or current rms values when the interrupt is triggered for multiple times and average them. The result is $VRMS_N$ or $IRMS_N$.
- c) Supply the ADE7878A with the minimum current I_{min} or minimum voltage V_{min} .
- d) Read the $IRMS$ or $VRMS$ registers multiple times at the zero-crossing interrupts, average the readings and call this number $IRMS_{min}$ or $VRMS_{min}$.

The voltage offset $VRMSOS$ and the current offset $IRMSOS$ calibrated values are the signed 24-bit hexadecimal representation of:

$$VRMSOS = \frac{VRMS_{min}^2 \times V_N^2 - VRMS_N^2 \times V_{min}^2}{128 \times (V_{min}^2 - V_N^2)} \quad (C.6)$$

$$= \frac{49.92113129^2 \times 230^2 - 229.9768986^2 \times 50^2}{128 \times (50^2 - 230^2)} = \frac{-390321.14762}{-6451200} = 0.06050365$$

where 229.9768986 is the average of 1024 voltage rms measurements from the ADE7878A when it is supplied with $VRMS_N = 230$ Vrms; and 49.92113129 is the average of 1024 voltage rms measurements from the ADE7878A when it is supplied with $VRMS_{min} = 50$ Vrms.

$$VRMSOS = 0.06050365 \times 2^{23} = 507541 = 0xFFF7BE95$$

and

$$IRMSOS = \frac{IRMS_{min}^2 \times I_N^2 - IRMS_N^2 \times I_{min}^2}{128 \times (I_{min}^2 - I_N^2)} \quad (C.7)$$

$$= \frac{0.999325675^2 \times 20^2 - 19.9983204^2 \times 1^2}{128 \times (1^2 - 20^2)} = \frac{-0.4720969}{-51072} = 9.2437 \times 10^{-6}$$

where 19.9983204 is the average of 1024 voltage rms measurements from the ADE7878A

Appendix C. ADE7878A Calibration

when it is supplied with $IRMS_N = 20$ A; and 0.999325675 is the average of 1024 voltage rms measurements from the ADE7878A when it is supplied with $IRMS_{min} = 1$ A.

$$IRMSOS = 9.2437 \times 10^{-6} \times 2^{23} = 77 = 0x\text{FFFFFF4D}$$

Total and fundamental active energy calibration

To calibrate the total active energy, the next procedure was followed:

- a) Supply the meter with accurate nominal voltage, nominal current, and power factor equal to 1.
- b) Calibrate the WGAIN register.
- c) Supply the meter with accurate nominal voltage, nominal current, and power factor equal to 0.5.
- d) Calibrate the PHCAL register.
- e) Supply the meter with accurate nominal voltage, minimum current at which the meter must be certified, and power factor equal to 1.
- f) Calibrate the WATTOS register.

Calibration of the WGAIN register

The calibration of WGAIN register compensate for the time measurement error introduced by the ADE7878A clock. To perform WGAIN calibration, the following procedure was followed:

- a) Supply the ADE7878A with accurate nominal current, nominal voltage, and a power factor of 1.
- b) Compute the content that the WATTHR register would have if under ideal conditions by

$$WATTHR_{REF} = \frac{V_N \times I_N}{10^{-3} \times 3600} \times \frac{100}{2} \times \frac{5118}{256 \times 10^3}$$

Appendix C. ADE7878A Calibration

- c) Read the WATTHR register multiple times and use the arithmetical average of WATTHR in Equation C.8.

WGAIN is the signed 24-bit hexadecimal representation of:

$$WGAIN = \frac{WATTHR_{REF}}{WATTHR} - 1 \quad (C.8)$$

The aforementioned procedure was followed to calibrate gain registers for the total active power (WGAIN), the fundamental active power (FWGAIN), and the total apparent power (VAGAIN). The results from the performed calibration of this registers are presented below.

$$WGAIN = \frac{WATTHR_{REF}}{WATTHR} - 1 = \frac{1277.2786}{1278.795194} - 1 = -0.0011859$$

$$WGAIN = -0.0011859 \times 2^{23} = -9948 = 0xFFFD924$$

$$FWGAIN = \frac{FWATTHR_{REF}}{FWATTHR} - 1 = \frac{1277.2786}{1279.059079} - 1 = -0.00139198$$

$$FWGAIN = -0.00139198 \times 2^{23} = -11677 = 0xFFFFD263$$

$$VAGAIN = \frac{VAWATTHR_{REF}}{VAWATTHR} - 1 = \frac{1277.2786}{1278.767424} - 1 = -0.001164$$

$$VAWGAIN = -0.001164 \times 2^{23} = -1135 = 0xFFFFD9DA$$

Total and fundamental reactive energy calibration

The total and fundamental reactive energy can be calibrated using the same procedures presented for the total active energy calibration. The only difference is that the current and voltage must have a power factor of 0 (the current has a delay of 90° relative to the voltage). The results from the performed calibration of registers for the total reactive

Appendix C. ADE7878A Calibration

energy (VARGAIN) and the fundamental reactive energy (FVARGAIN) are presented below.

$$VARGAIN = \frac{VARWATTHR_{REF}}{VARWATTHR} - 1 = \frac{1277.2786}{1278.632534} - 1 = -0.001058$$

$$VARWGAIN = -0.001058 \times 2^{23} = -8882 = 0XFFFFDD4E$$

$$FVARGAIN = \frac{FVARWATTHR_{REF}}{FVARWATTHR} - 1 = \frac{1277.2786}{1278.649458} - 1 = -0.001072$$

$$FVARWGAIN = -0.001072 \times 2^{23} = -8993 = 0xFFFFDCDF$$

Phase angle calibration

The phase angle calibration is necessary to compensate for the phase delay introduced by the current sensor. The procedure to calibrate the PHCAL register is as follows:

- a) Supply the ADE7878A with nominal current, nominal voltage, and a power factor of 0.5 inductive (the current has a delay of 60° relative to the voltage).
- b) Use the same initializations as in calibration of the WGAIN register.
- c) Compute the content that the WATTHR register would have if under ideal conditions by

$$WATTHR_{REF} = \frac{V_N \times I_N \times 0.5}{10^{-3} \times 3600} \times \frac{100}{2} \times \frac{5118}{256 \times 10^3}$$

- d) Read the WATTHR register multiple times and use the arithmetical average of WATTHR in the next Equation.
- e) Compute the angle representing the delay error between the phase current and phase voltage by

$$x = \arcsin \left[\frac{1}{\sqrt{3}} \left(1 - \frac{WATTHR}{WATTHR_{REF}} \right) \right]$$

Appendix C. ADE7878A Calibration

The phase resolution of the timer used to compensate the phase delay is

$$phase_resolution = \frac{360 \times f_L}{1.024 \times 10^6} = \frac{90}{Period} = 0.01758499 \quad (C.9)$$

where f_L is the line frequency of the system (50 Hz) and $Period$ is the ADE7878A register indicating the line period of the voltage. Divide x by the $phase_resolution$ and compute the PHCAL number by

$$PHCAL = \left| \frac{x}{phase_resolution} \right| = \left| \frac{-0.265}{0.01758499} \right| = 15.0696 \quad (C.10)$$

Appendix D

Waveform Parameters

This appendix contains figures to illustrate some terms used in this thesis to describe waveform parameters. Definitions of such terms have been taken from the IEEE 181-2011 standard for transitions, pulses, and related waveforms [95]. Figure D.1 present an example of positive-going transition from the *Switched-mode power supply* test waveform and Figure D.2 exemplify a negative-going transition occurring in the *1/8 falling* test waveform.

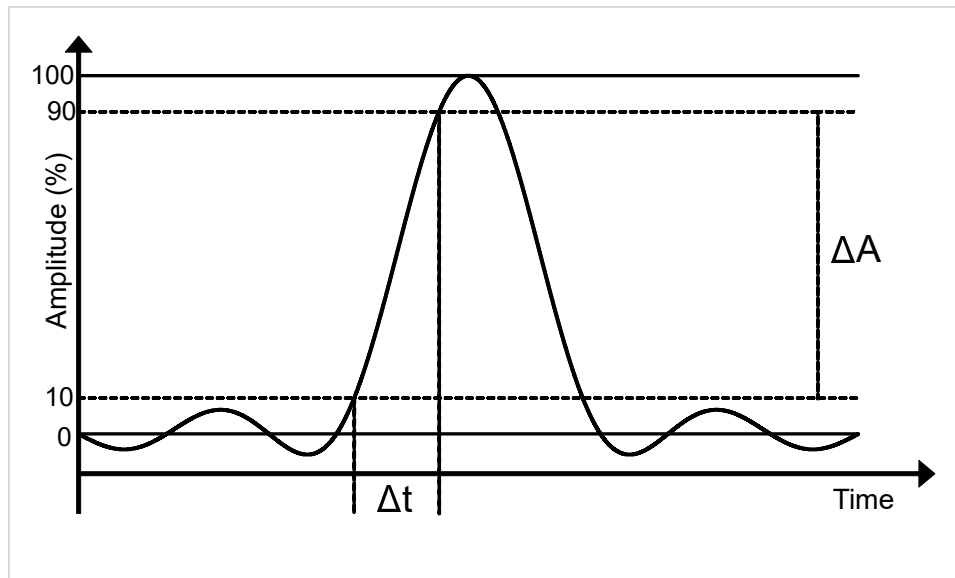


Figure D.1: Positive-going transition

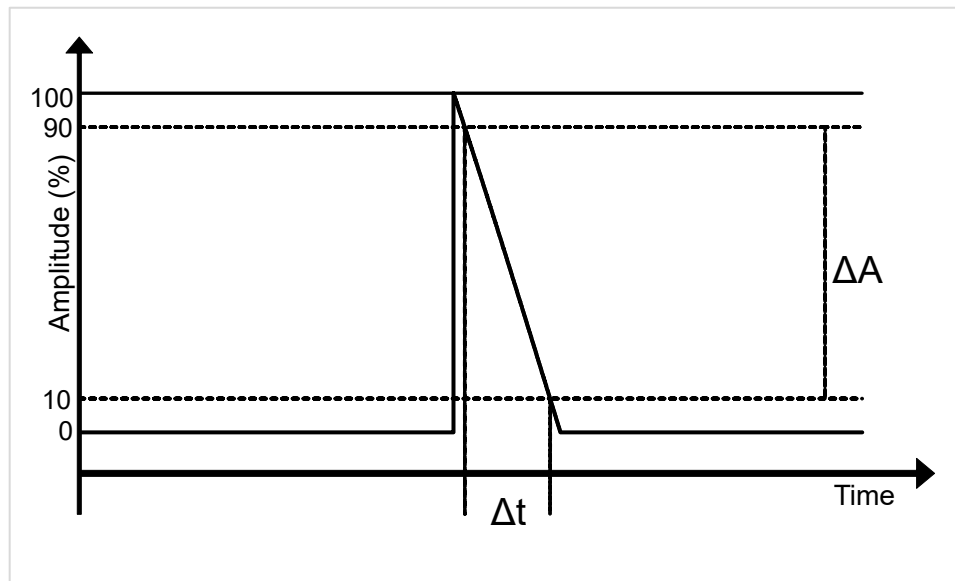


Figure D.2: Negative-going transition

Parameter Definition

| | |
|---------------------|---|
| Transition | Contiguous region of a waveform that connects, either directly or via intervening transients, two state occurrences that are consecutive in time but are occurrences of different states. In Figures D.1 and D.2, the transition is represented by ΔA symbol. |
| Transition duration | The difference between the two reference level instants of the same transition. Unless otherwise specified, the two reference levels are the 10% and 90% reference levels. In Figures D.1 and D.2, the transition duration is represented by Δt symbol. |
| Slope | Ratio of the transition amplitude to the transition duration between two distinct points on a waveform. $Slope = \Delta A / \Delta t$ |

Appendix E

Step-like Shaped Current Waveforms Gallery

This appendix presents step-like shaped current waveforms which were used in recent studies to evaluate the effects of such pulsed signals on SEM measurement errors. The waveforms were recorded in real-world power systems (Figures E.1 to E.7) or were mathematically defined (Figures E.8 to E.10).

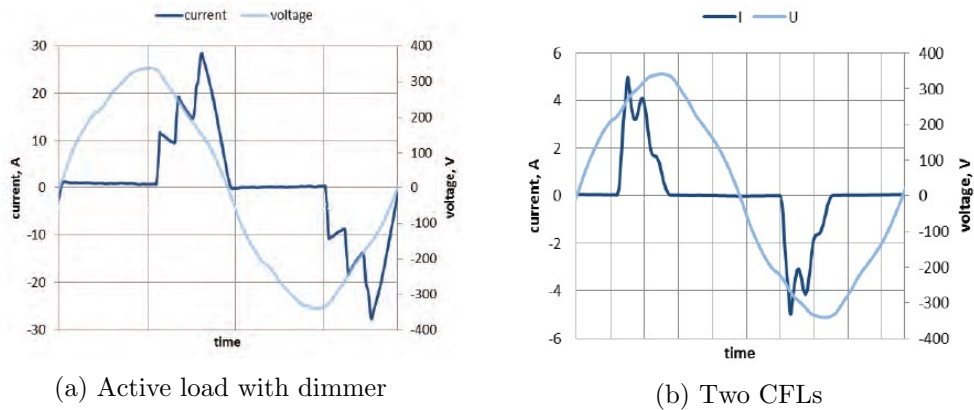


Figure E.1: Pulsed current waveforms drawn by: (a) a set of pure active load with dimmer and (b) two CFLs. Figures taken from the paper *Analysis of Electricity Meters under Distorted Load Conditions* [12].

Appendix E. Step-like Shaped Current Waveforms Gallery

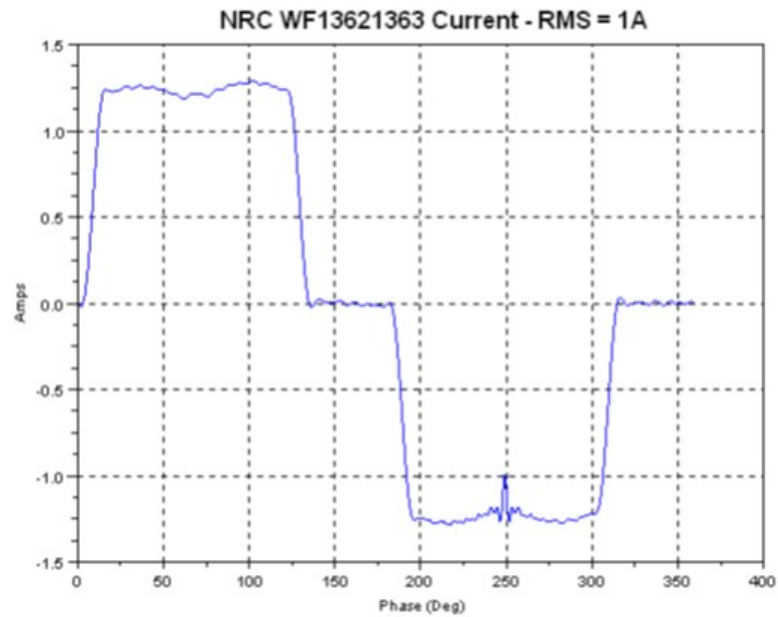


Figure E.2: Current waveform NRC WF1363 recorded in the field by the National Research Council Canada (NRC) and presented in [96].

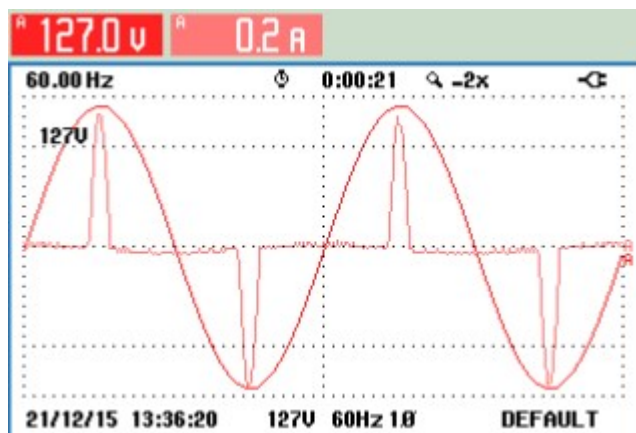


Figure E.3: Pulsed current waveform drawn by a LED TV. Figure taken from the paper *Analysis of the Influence of Non-Linear Loads on the Measurement and Billing of Electrical Energy Compared with the CPT* [97].

Appendix E. Step-like Shaped Current Waveforms Gallery

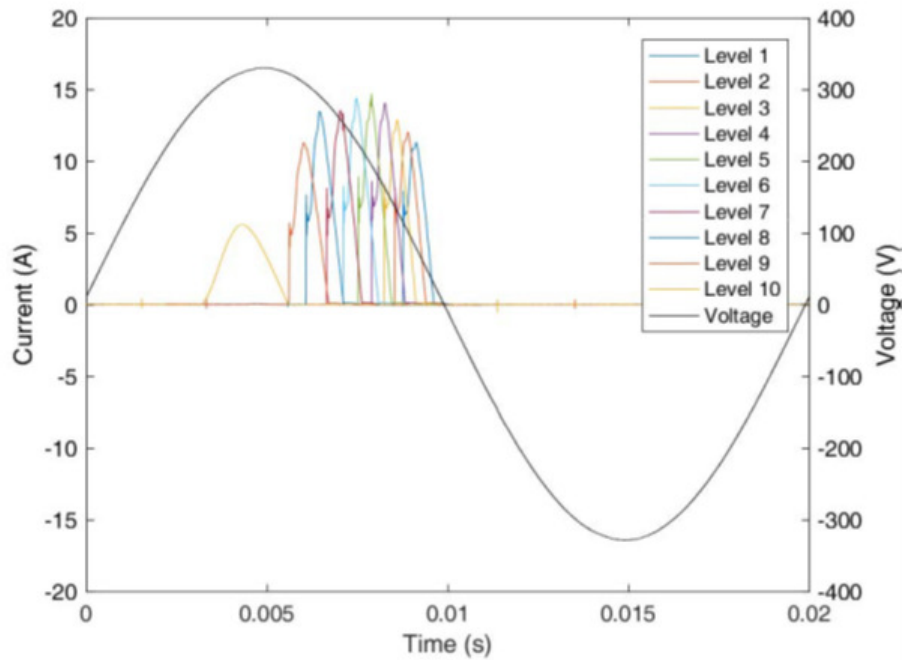


Figure E.4: Current waveforms generated by remote control at different power output levels in combination with a water pump. Figure taken from the paper *Faulty Readings of Static Energy Meters Caused by Conducted Electromagnetic Interference from a Water Pump* [61].

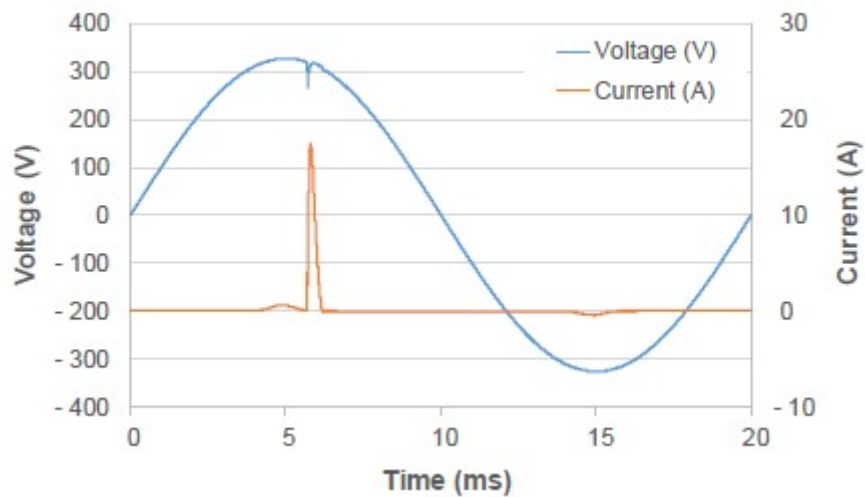


Figure E.5: Current waveforms generated by a water pump with included dimmer used for fish ponds. Figure taken from the paper *A Testbed for Static Electricity Meter Testing with Conducted EMI* [19].

Appendix E. Step-like Shaped Current Waveforms Gallery

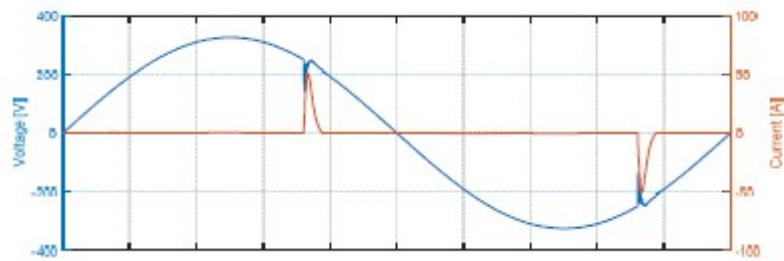
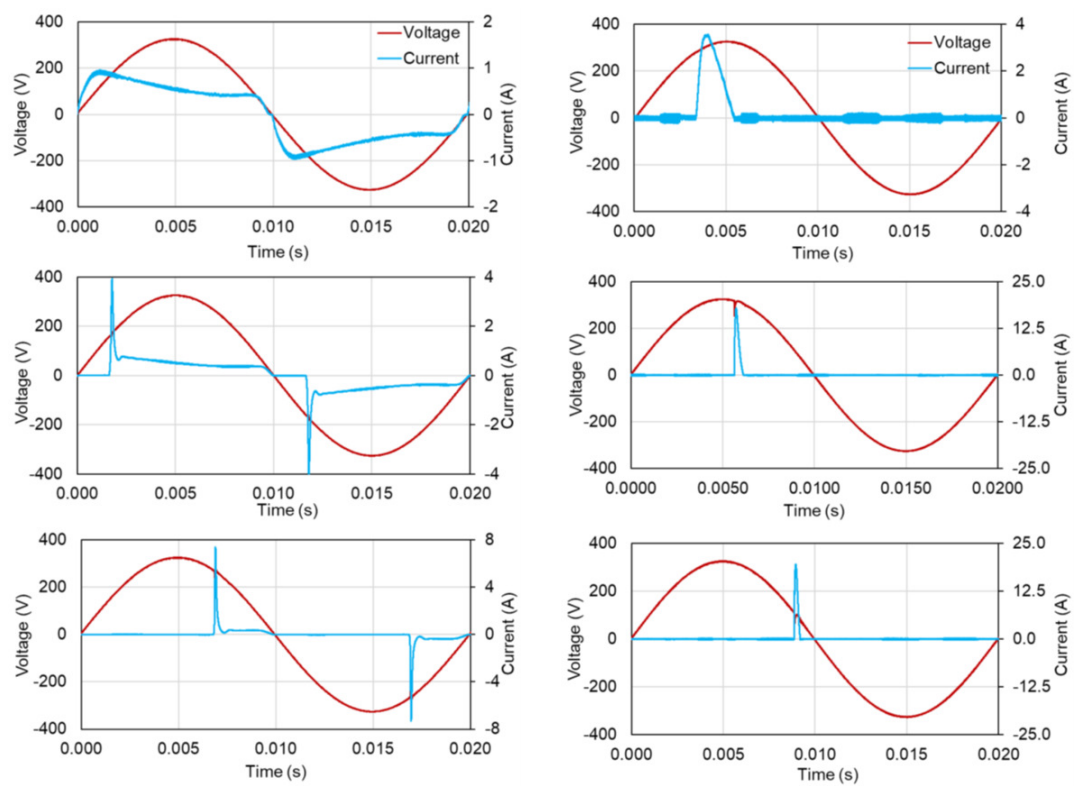


Figure E.6: Current waveform generated by a set of 30 non-dimmable energy-saving lamps controlled by a dimmer set at 135 degrees. Figure taken from the paper *Conducted EMI causing Error Readings of Static Electricity Meters* [59].



(a) Eight LED lamps with a dimmer

(b) A water pump with a dimmer

Figure E.7: Pulsed current measured waveforms of household appliances: (a) a wall mounted dimmer with eight dimmable LED lamps and (b) water pump and dimmer. Figures taken from the paper *Current waveforms of household appliances for advanced meter testing* [60].

Appendix E. Step-like Shaped Current Waveforms Gallery

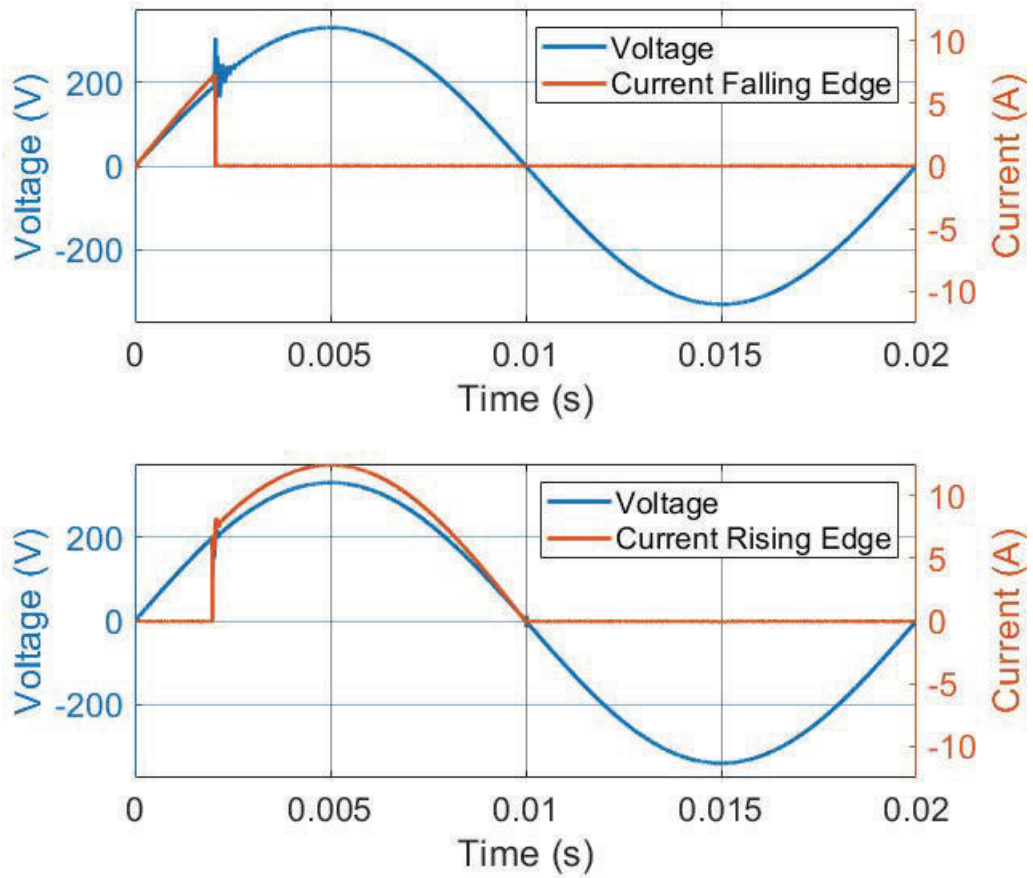


Figure E.8: Theoretically designed step-like current waveforms: falling and rising edge dimming in the first quarter of a cycle. Figures taken from *The Effects of Falling and Rising Edge Dimming on Static Energy Meter Errors* [94].

Appendix E. Step-like Shaped Current Waveforms Gallery

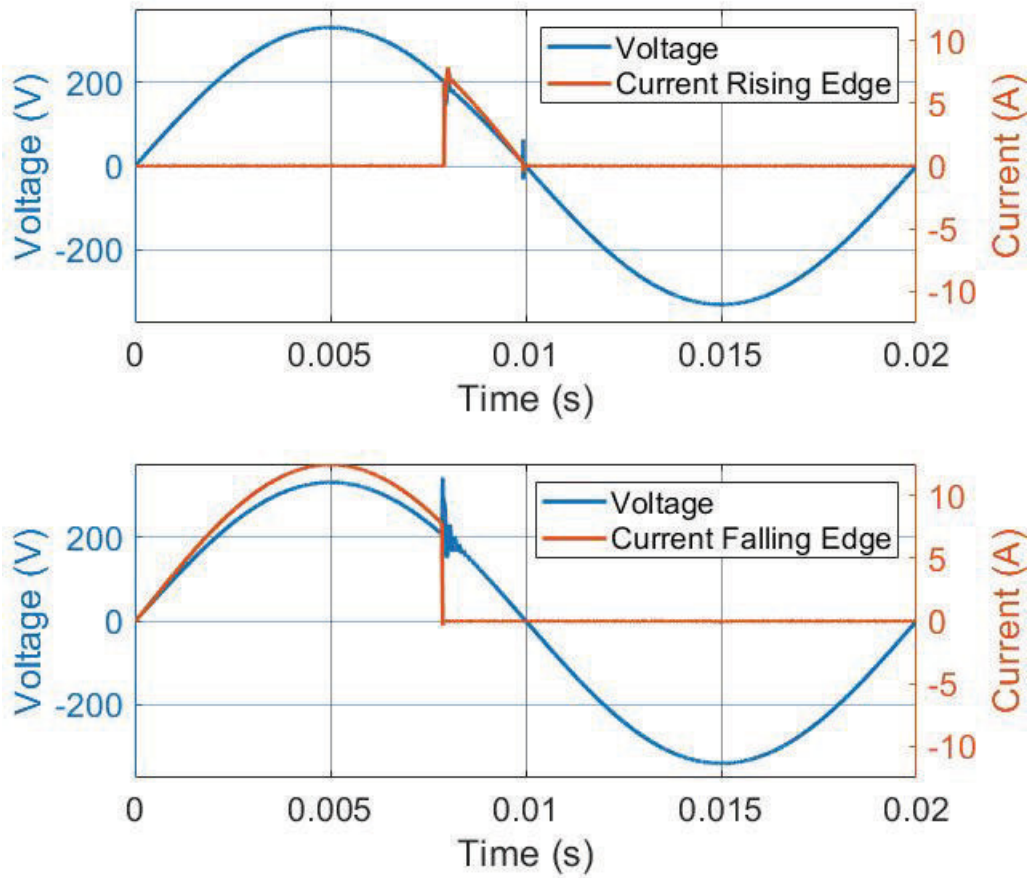


Figure E.9: Theoretically designed step-like current waveforms: falling and rising edge dimming in the second quarter of a cycle. Figures taken from *The Effects of Falling and Rising Edge Dimming on Static Energy Meter Errors* [94].

Appendix E. Step-like Shaped Current Waveforms Gallery

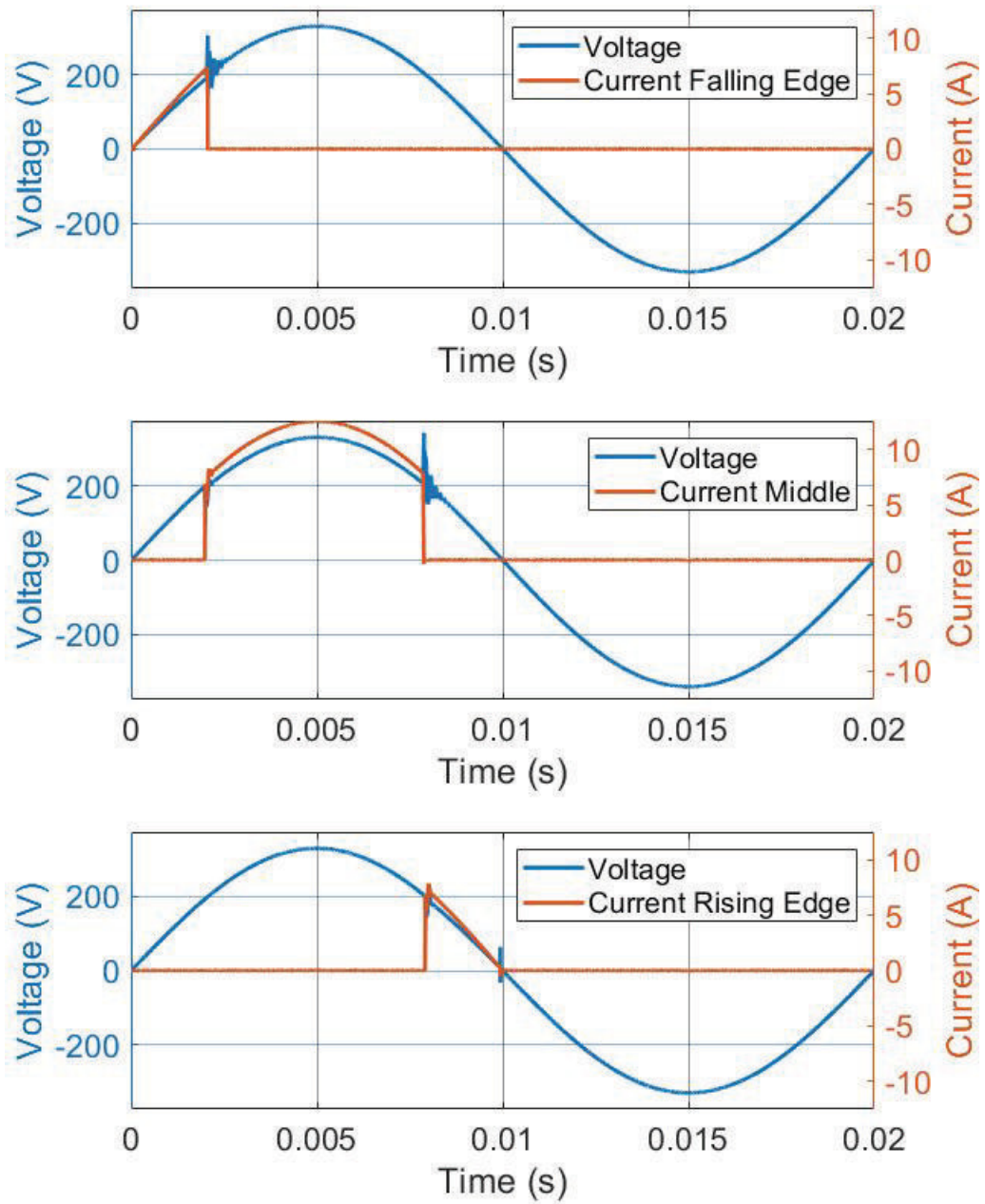


Figure E.10: Theoretically designed step-like current waveforms: falling and rising edge dimming. Figures taken from *The Effects of Falling and Rising Edge Dimming on Static Energy Meter Errors* [94].

Appendix F

ADE7878A Model Calculations

In this appendix, the formulas implemented in the ADE7878A model are described. Most implemented formulas use predefined LabVIEW functions (i.e. predefined calculation blocks) to estimate relevant electrical quantities from the waveforms.

rms values To calculate the voltage and current rms values, the IC model uses the LabVIEW's rms function as can be seen in Figure F.1.

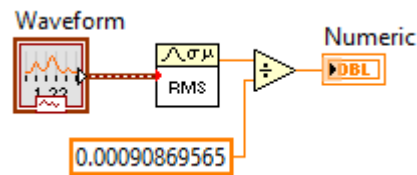


Figure F.1: ADE7878A IC model rms calculation.

The rms LabVIEW's function in Figure F.1 implements the following equation to obtain the rms values from a given waveform:

$$\Psi_x = \sqrt{\frac{1}{n} \sum_{i=0}^{n-1} |x_i|^2} \quad (\text{F.1})$$

where Ψ_x is the rms value and n is the number of elements in x .

Current peak value

To calculate the current peak value, the IC model uses the Statistics function (Figure

Appendix F. ADE7878A Model Calculations

F.2), which can give the highest point in a set of values, i.e. the maximum value.

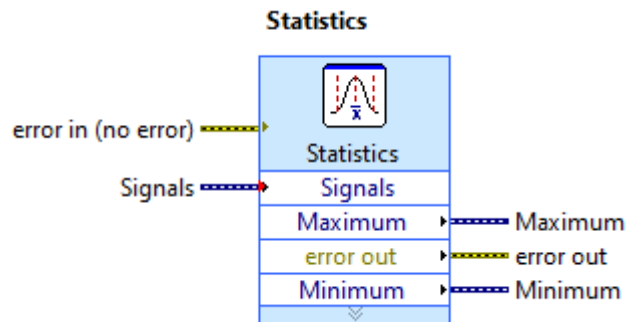


Figure F.2: ADE7878A IC model current peak value calculation.

Phase Angle

To calculate the phase angle, the IC model follows the procedure described in 4.3.2.2 and depicted in Figure F.3.

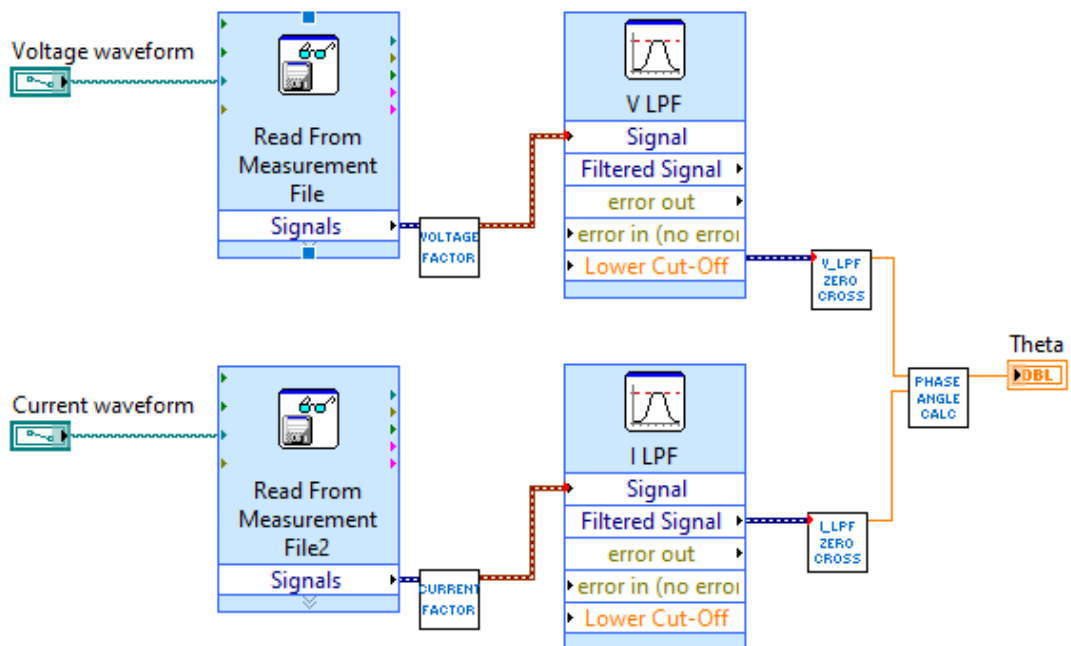


Figure F.3: ADE7878A IC model phase angle calculation.

The ADE7878A model applies low-pass filters to the voltage and current signals to calculate the phase angle θ by means of measuring the time difference between the

Appendix F. ADE7878A Model Calculations

negative to positive zero-crossing occurrence of the filtered signals, previously discussed in 4.3.2.2. These filters are represented in Figure F.3 by the VLPF and ILPF blocks and their specifications, based on the limited information provided in the IC's documentations are:

- Cutoff frequency = 80 Hz
- Order = 1
- Topology = Butterworth (IIR)

Total Active Power

To calculate the total active power, the IC model employs a summation function (Figure F.4) to add continuously 163840 instantaneous power values (i.e. one 50 Hz cycle) and then divide the result over the number of samples, which is equivalent to equation 4.10.

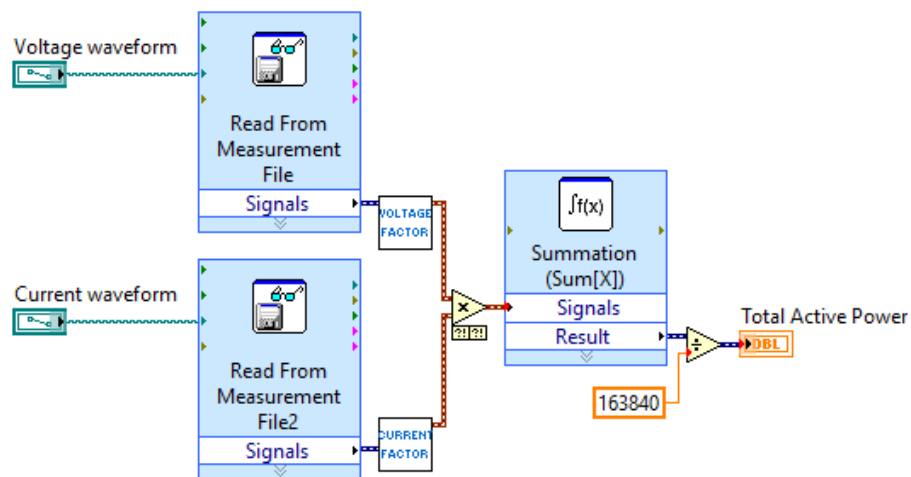


Figure F.4: ADE7878A IC model total active power calculation.

Total Reactive Power

To calculate the total reactive power, the IC model employs a summation function to add continuously 163840 instantaneous power values (i.e. one 50 Hz cycle) and multiply the summation with the sine of the phase angle (Figure F.5). Then the result is divided over the number of samples. This procedure is equivalent to equation 4.14.

Appendix F. ADE7878A Model Calculations

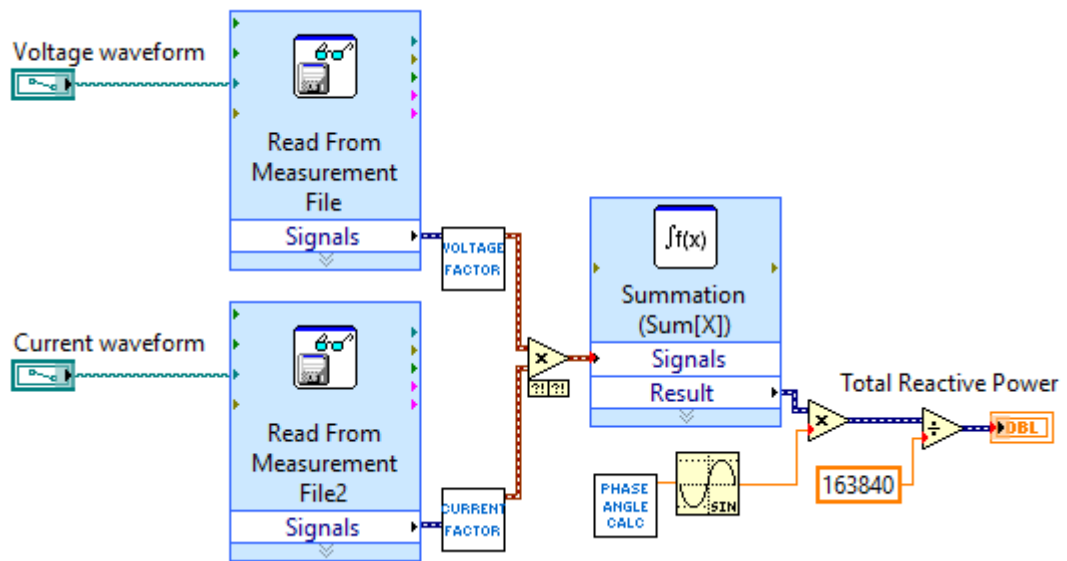


Figure F.5: ADE7878A IC model total reactive power calculation.

Total Apparent Power

To calculate the total apparent power, the IC model multiplies the current and voltage rms values as per equation 4.15 (see Figure F.6).

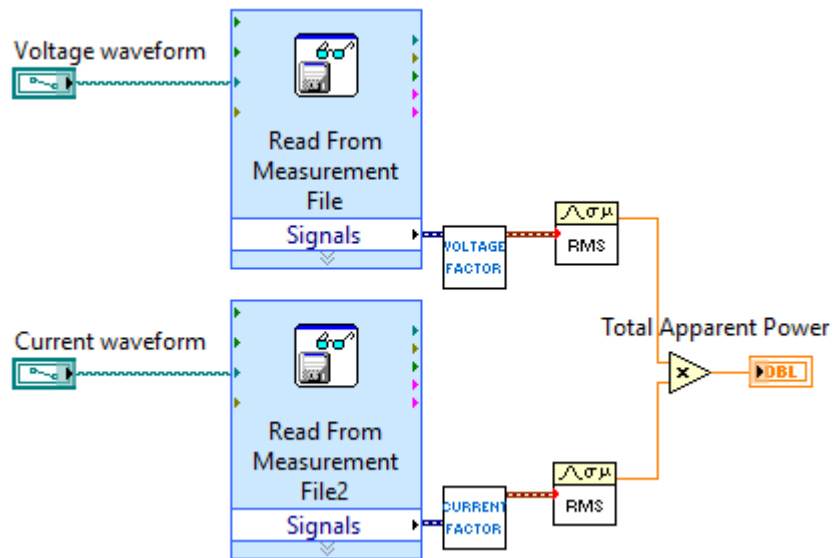


Figure F.6: ADE7878A IC model total apparent power calculation.

Total Active Energy

Appendix F. ADE7878A Model Calculations

To calculate the total active energy, the IC model multiplies the current and voltage instantaneous values to obtain the total active power. Then, the total active power values are accumulated over one cycle in the summation LabVIEW's function (Figure F.7). Finally, the sub-virtual instrument (Sub-VI) Energy Factor divide the summation result to obtain the total active energy calculation in kWh.

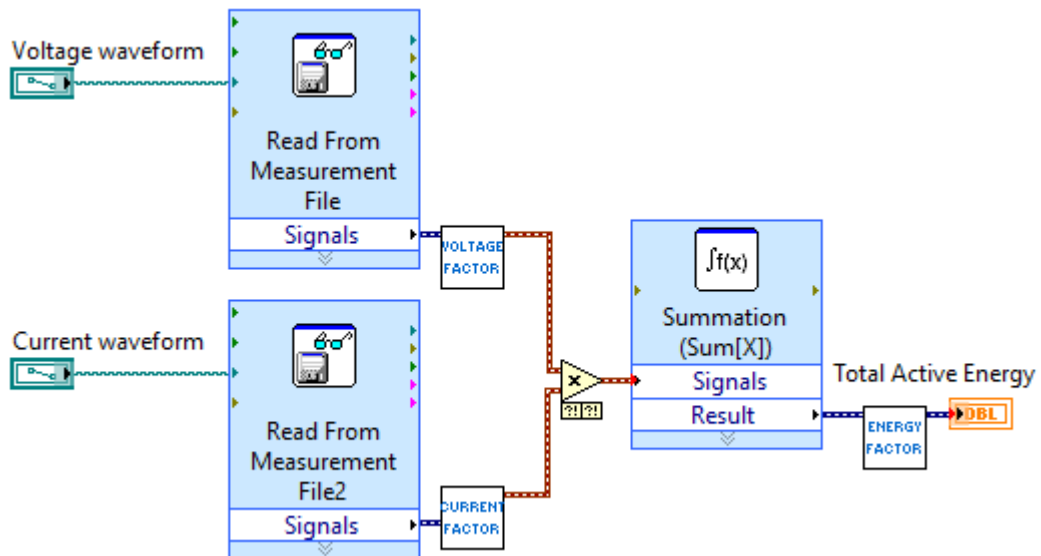


Figure F.7: ADE7878A IC model total active energy calculation.

Fundamental Active Energy

To calculate the fundamental active energy, the IC model applies band-pass filters (BPF) to extract the fundamental signal components (i.e. 50 Hz) of the voltage and current waveforms. The parameters of the BPF have been chosen to emulate the ADE7878A implemented digital filters, based on the very limited information provided in the IC's documentation. The specifications of the BPF are:

- Low cutoff frequency = 45Hz
- High cutoff frequency = 65Hz
- Order = 4
- Topology = Butterworth (IIR)

Appendix F. ADE7878A Model Calculations

Next, the rms values of filtered voltage and current signals are obtained and multiplied. Then, the result is multiplied by the cosine of θ_1 as can be seen in Figure F.8. Finally, resulting values are accumulated in the summation LabVIEW's function and the E_1 Sub-VI divide the summation result to obtain the fundamental active energy calculation in kWh.

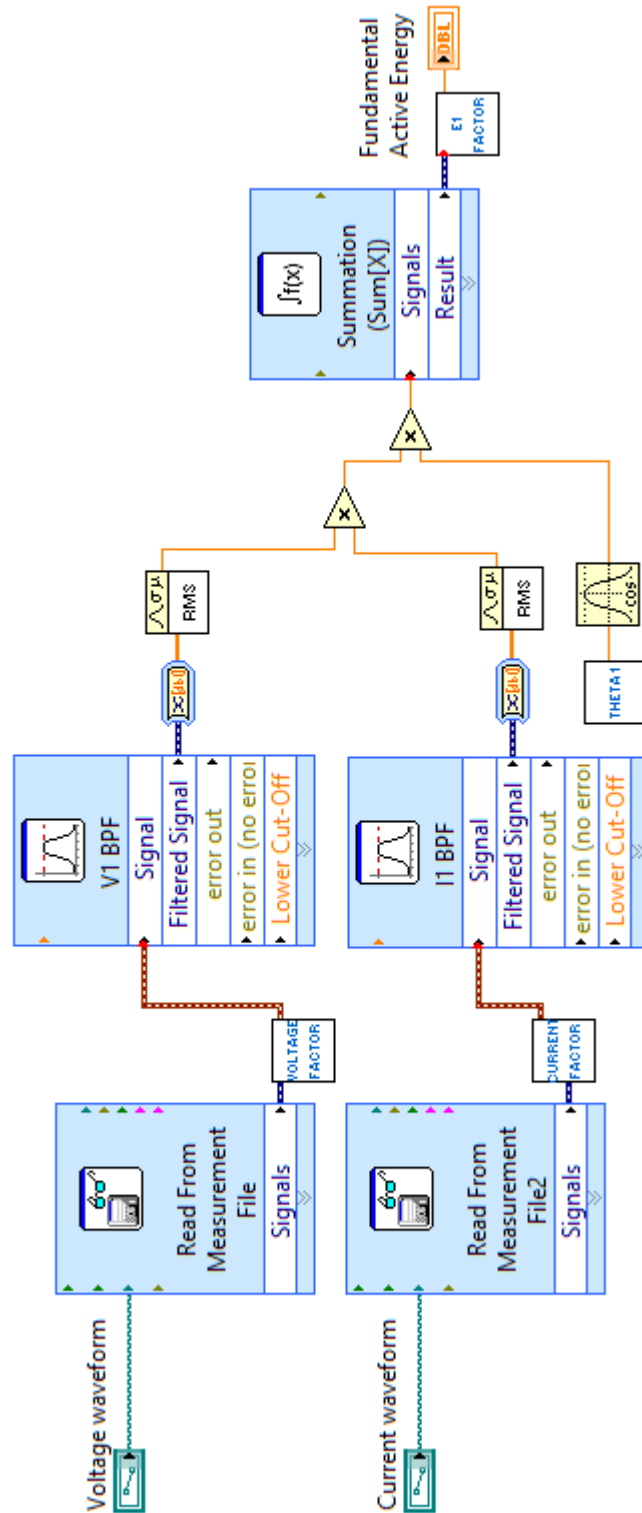


Figure F.8: ADE7878A IC model fundamental active energy calculation.

Total Reactive Energy

To calculate the total reactive energy, the IC model multiplies the current and voltage instantaneous values and the result is multiplied by the sine of the phase angle θ as can be observed in Figure F.9.

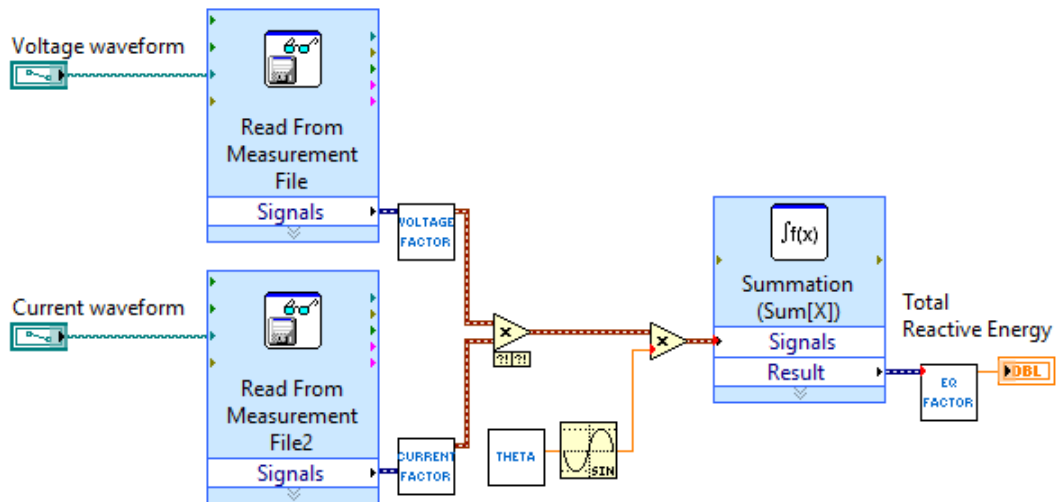


Figure F.9: ADE7878A IC model total reactive energy calculation.

Next, the results are accumulated in the summation LabVIEW's function and a factor is applied to obtain the total active energy calculations in kvarh.

Fundamental Reactive Energy

To calculate the fundamental reactive energy, the IC model applies band-pass filters (BPF) to extract the fundamental signal components (i.e. 50 Hz) of the voltage and current waveforms, as has been done for the total active energy calculation, previously discussed. The signal path to calculate fundamental active power and fundamental reactive power is the same and consequently, the BPF are the same utilized to calculate the fundamental active power (see F).

Next, the rms values of filtered voltage and current signals are obtained and multiplied. Then, the result is multiplied by the sine of θ_1 as can be seen in Figure F.10. Finally, resulting values are accumulated in the summation LabVIEW's function and the E_Q1 Sub-VI divide the summation result to obtain the fundamental reactive energy calculation in kvarh.

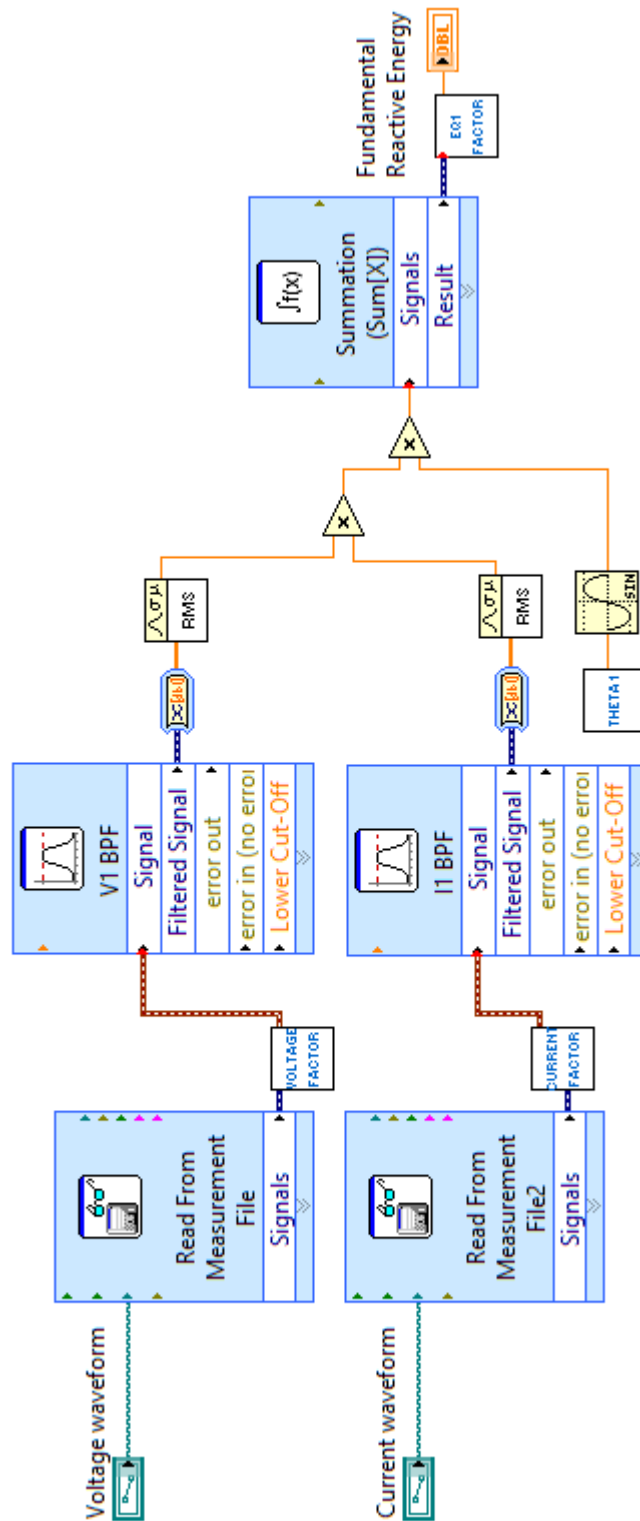


Figure F.10: ADE7878A IC model fundamental reactive energy calculation.

Bibliography

- [1] NIST, “Advanced Metering in Smart Distribution Grids,” tech. rep., National Institute of Standards and Technology, 2012.
- [2] IEC, “BS EN IEC 62052-11:2021 Electricity metering equipment (AC) — General requirements, tests and test conditions — Part 11: Metering equipment,” 2021.
- [3] IEC, “BS EN IEC 62053-11:2003+A1:2017 Electricity metering equipment (AC) — General requirements, tests and test conditions — Part 11: Metering equipment,” 2018.
- [4] IEC, “BS EN IEC 62053-21:2021+A11:2021 Electricity metering equipment (a.c.) — Particular requirements — Part 21: Static meters for active energy (classes 1 and 2),” 2021.
- [5] IEC, “BS EN IEC 62053-22:2021 Electricity metering equipment (a.c.) — Particular requirements — Part 22: Static meters for active energy (classes 0,2 S and 0,5 S),” 2021.
- [6] “ANSI C12.20-2010 American National Standard for Electricity Meters— 0.2 and 0.5 Accuracy Classes,” 2010.
- [7] “Global Smart Metering Markets, 2018-2019 & Forecast to 2024,” 2019.
- [8] A. J. Berrisford, “A Smarter Meter: IEEE-1459 power definitions in an off-the-shelf Smart Meter,” 2015.
- [9] B. Jakovljevic, Z. Hederic, D. Baresic, and N. Cvetkovic, “FEM analysis of single-phase electromechanical meter at non-sinusoidal power supply,” 2016.

Bibliography

- [10] M. Gul, N. Tai, M. A. Mahar, W. Huang, and A. S. Larik, "Performance evaluation of energy meters under nonlinear loads," *Journal of Shanghai Jiaotong University (Science)*, vol. 22, pp. 133–138, 4 2017.
- [11] J. Novotny, J. Drapela, and D. Topolánek, "Frequency response of revenue meters in measured active energy," 2016.
- [12] A. Haas, J. Niitsoo, P. Taklaja, and I. Palu, "Analysis of electricity meters under distorted load conditions," 2012.
- [13] A. Ferrero and C. Muscas, "On the selection of the "best" test waveform for calibrating electrical instruments under nonsinusoidal conditions," *IEEE Transactions on Instrumentation and Measurement*, vol. 49, no. 2, pp. 382–387, 2000.
- [14] M. Youhannaei, M. E. Honarmand, S. Ouni, R. Mehri, H. Mokhtari, and J. Talebi, "Performance evaluation of energy meters in nonsinusoidal environment based on IEEE 1459 standard," 2013.
- [15] P. Bilik, M. Prauzek, and T. Josefova, "Precision check of energy meters under nonsinusoidal conditions," 2013.
- [16] D. Georgakopoulos and P. S. Wright, "Calibration of energy and power meters under non-sinusoidal conditions," 2006.
- [17] A. D. Femine, D. Gallo, C. Landi, and M. Luiso, "Advanced Instrument For Field Calibration of Electrical Energy Meters," *IEEE Transactions on Instrumentation and Measurement*, vol. 58, no. 3, pp. 618–625, 2009.
- [18] A. Ferrero, M. Faifer, and S. Salicone, "On Testing the Electronic Revenue Energy Meters," 2009.
- [19] H. E. v. d. Brom, Z. Marais, D. Hoogenboom, R. v. Leeuwen, and G. Rietveld, "A Testbed for Static Electricity Meter Testing with Conducted EMI," in *2019 International Symposium on Electromagnetic Compatibility - EMC EUROPE*, pp. 603–608, 2019.

Bibliography

- [20] “IEEE 1459:2010 Standard Definitions for the Measurement of Electric Power Quantities Under Sinusoidal, Nonsinusoidal, Balanced, or Unbalanced Conditions,” 2010.
- [21] OIML, “OIML R 46-1/-2 Active electrical energy meters. Part 1: Metrological and technical requirements,” 2012.
- [22] “Electromagnetic compatibility (EMC) Part 4-19: Testing and measurement techniques — Test for immunity to conducted, differential mode disturbances and signalling in the frequency range 2 kHz to 150 kHz at a.c. power ports, IEC 61000-4-19: 2014,” 2014.
- [23] D. Gallo, C. Landi, N. Pasquino, and N. Polese, “A New Methodological Approach to Quality Assurance of Energy Meters Under Non-Sinusoidal Conditions,” 2006.
- [24] L. S. Czarnecki, “Comments on active power flow and energy accounts in electrical systems with nonsinusoidal waveforms and asymmetry,” 1996.
- [25] R. Quijano Cetina, A. J. Roscoe, and P. Wright, “Challenges for Smart Electricity Meters due to Dynamic Power Quality Conditions of the Grid: A Review,” *2017 IEEE International Workshop on Applied Measurements for Power Systems (AMPS)*, pp. 1–6, 9 2017.
- [26] F. Leferink, C. Keyer, and A. Melentjev, “Static energy meter errors caused by conducted electromagnetic interference,” 2016.
- [27] “PANDA (equiPment hArmoNic DATabase). <https://panda.et.tu-dresden.de/cgi-bin/PANDA.cgi>.”
- [28] R. Quijano, Y. Seferi, S. M. Blair, and P. S. Wright, “Analysis and Selection of Appropriate Components for Power System Metrology Instruments,” in *2nd International Colloquium on Smart Grid Metrology (SMAGRIMET)*, (Split, Croatia), 2019.
- [29] EPRI, “Accuracy of Digital Electricity Meters,” 2010.

Bibliography

- [30] “Electricity meter - Wikipedia.”
- [31] R. Kemper, P. Komor, and A. Hoke, “Smart Grids and Renewables: A Guide for Effective Deployment,” tech. rep., IRENA, 2013.
- [32] A. Emanuel, *Power Definitions and the Physical Mechanism of Power Flow: Emanuel/Power Definitions and the Physical Mechanism of Power Flow*. Wiley - IEEE, 2010.
- [33] A. J. Berrisford, “New technology and power definitions make accurate revenue metering possible in the presence of harmonic distortion,” in *2009 IEEE Electrical Power & Energy Conference (EPEC)*, pp. 1–8, 2009.
- [34] A. J. Berrisford, “Smart Meters should be smarter,” 2012.
- [35] A. J. Berrisford, “Metering and Harmonics - The Inequity Issue A Discussion Presentation,” 2016.
- [36] S. Pajic and A. E. Emanuel, “Modern apparent power definitions: theoretical versus practical Approach-the general case,” *IEEE Transactions on Power Delivery*, vol. 21, pp. 1787–1792, 10 2006.
- [37] CENELEC, “BS EN 50160:2010+A3:2019,” 2019.
- [38] “The history of the electricity meter — Smart Energy International,” 2006.
- [39] “ANSI C12.1-2014 American National Standard for Electric Meters — Code for Electricity Metering,” 2016.
- [40] “ANSI C12.20-2015 American National Standard for Electricity Meters - 0.1, 0.2, and 0.5 Accuracy Classes,” 2017.
- [41] B. Kelechava, “ANSI C12.20-2015 - Electricity Meters - 0.1, 0.2, and 0.5 Accuracy Classes - ANSI Blog,” 2017.
- [42] “MID approved gas and electricity meters - GOV.UK.”

Bibliography

- [43] “BS EN 50470-1:2006+A1:2018 Electricity metering equipment (a . c .) — General requirements, tests and test conditions — Metering equipment (class indexes A, B and C),” 2019.
- [44] “BS EN 50470-3:2006+A1:2018 Electricity metering equipment (a . c .) — Part 3: Particular requirements — Static meters for active energy (class indexes A, B and C),” 2019.
- [45] J. Lundquist, “THESIS FOR THE DEGREE OF LICENTIATE OF ENGINEERING On Harmonic Distortion in Power Systems,” tech. rep., CHALMERS UNIVERSITY OF TECHNOLOGY, Göteborg, Sweden, 2001.
- [46] W. Kui, G. Shuhua, H. Qian, H. Yuanhong, and W. Qinfang, “Investigation of harmonic distortion and losses in distribution systems with non-linear loads,” in *2008 China International Conference on Electricity Distribution*, pp. 1–6, 12 2008.
- [47] S. Vlahinic, D. Brnobic, and N. Stojkovic, “Indices for Harmonic Distortion Monitoring of Power Distribution Systems,” *IEEE Transactions on Instrumentation and Measurement*, vol. 58, pp. 1771–1777, 5 2009.
- [48] R. Quijano Cetina, A. J. Roscoe, and P. S. Wright, “Challenges for smart electricity meters due to dynamic power quality conditions of the grid: a review,” in *IEEE International Workshop on Applied Measurements for Power Systems (AMPS)*, (Liverpool, UK), 2017.
- [49] A. Berrisford, “A Closer look at the Sub-harmonic Test for Watthour Meters,” 2020.
- [50] CENELEC, “EN 61000-4-4:2012 Electromagnetic compatibility (EMC)-Part 4-4: Testing and measurement techniques-Electrical fast transient/burst immunity test,” tech. rep., CENELEC, Brussels, 2012.
- [51] JCGM, “Evaluation of measurement data-Guide to the expression of uncertainty in measurement,” 2008.

Bibliography

- [52] IEC, “EN 61869-2:2012 Instrument transformers, Part 2: Additional requirements for current transformers,” 2012.
- [53] IEC, “EN 61869-3:2011 Instrument transformers, Part 3: Additional requirements for inductive voltage transformers,” 2011.
- [54] L. Peretto and R. Tinarelli, *Sensors for PMUs*. Elsevier Inc., 2016.
- [55] H. Mani, “AN-639 APPLICATION NOTE Analog Devices Energy (ADE) Products: Frequently Asked Questions (FAQs) How do I obtain samples of a preliminary product and evaluation board?,” tech. rep., Analog Devices, 2013.
- [56] N. G. Paulter, “Method for Measuring the Phase Spectrum of the Output of a Frequency Source Used in the Calibration of an Electroshock Weapon Characterization System,” *Journal of Research of the National Institute of Standards and Technology*, vol. 122, no. 35, 2017.
- [57] Y. Chen, Q. Huang, and A. H. Khawaja, “Interference-rejecting current measurement method with tunnel magnetoresistive magnetic sensor array,” *IET Science, Measurement & Technology*, vol. 12, no. 6, pp. 733–738, 2018.
- [58] Y. C. Chen, W. H. Hsu, S. H. Cheng, and Y. T. Cheng, “Anti-electromagnetic interference and calibration schemes of flexible current sensor tag for reliable current detection in household appliance,” in *2013 Transducers & Eurosensors XXVII: The 17th International Conference on Solid-State Sensors, Actuators and Microsystems (TRANSDUCERS & EUROSENSORS XXVII)*, pp. 1356–1359, 2013.
- [59] G. Rietveld, D. Hoogenboom, and M. Acanski, “Conducted EMI Causing Error Readings of Static Electricity Meters,” in *2018 Conference on Precision Electromagnetic Measurements (CPEM 2018)*, pp. 1–2, 2018.
- [60] R. v. Leeuwen, H. v. d. Brom, D. Hoogenboom, G. Kok, and G. Rietveld, “Current waveforms of household appliances for advanced meter testing,” in *2019 IEEE 10th International Workshop on Applied Measurements for Power Systems (AMPS)*, pp. 1–6, 2019.

Bibliography

- [61] B. Ten Have, T. Hartman, N. Moonen, C. Keyer, and F. Leferink, “Faulty Readings of Static Energy Meters Caused by Conducted Electromagnetic Interference from a Water Pump,” *Renewable Energy & Power Quality Journal*, 2019.
- [62] M. J. Cunningham and G. L. Bibby, “11 - Electrical Measurement,” in *Electrical Engineer’s Reference Book (Sixteenth Edition)* (M. A. Laughton and D. J. Warne, eds.), pp. 11–43, Oxford: Newnes, sixteenth ed., 2003.
- [63] R. Masnicki and J. Mindykowski, “What Should Be Measured Using Static Energy Meters,” in *2018 International Conference and Exposition on Electrical And Power Engineering (EPE)*, pp. 183–188, 2018.
- [64] Analog Devices Inc, “ADE7878 Evaluation Board User Guide UG-146,” 2010.
- [65] F. Hohn, J. Wang, and L. Nordström, “Design of a Distributed Signal Processing Unit for Transmission Line Protection in a Centralized Substation Protection Architecture,” in *IECON 2018 - 44th Annual Conference of the IEEE Industrial Electronics Society*, pp. 138–144, 2018.
- [66] B. Pisani, “Accounting for delay from multiple sources in delta-sigma ADCs,” tech. rep., Texas Instruments, 2018.
- [67] A. J. Roscoe, S. M. Blair, B. Dickerson, and G. Rietveld, “Dealing With Front-End White Noise on Differentiated Measurements Such as Frequency and ROCOF in Power Systems,” *IEEE Transactions on Instrumentation and Measurement*, vol. 67, no. 11, pp. 2579–2591, 2018.
- [68] R. J. Baker, *Data Converter Architectures*. Wiley, 2010.
- [69] “IEEE Recommended Practice for Monitoring Electric Power Quality,” 2009.
- [70] M. Mason, “Reduce System Cost for Advanced Powerline Monitoring by Leveraging High-Performance, Simultaneous-Sampling ADCs,” *Maxim Engineering Journal*, vol. 67, pp. 3 – 7, 2009.

Bibliography

- [71] MAXIM, “Selecting the Right ADC for Your Application,” *ElectronicProducts.com*, 2015.
- [72] M. Jiménez, R. Palomera, and I. Couvertier, *Introduction to Embedded Systems Using Microcontrollers and the MSP430*. New York, NY: Springer New York, 2014.
- [73] “ADE7878 Poly Phase Multifunction Energy Metering IC with Total and Fundamental Powers.”
- [74] L. S. Czarnecki, “What is wrong with the Budeanu concept of reactive and distortion power and why it should be abandoned,” *IEEE Transactions on Instrumentation and Measurement*, vol. IM-36, no. 3, pp. 834–837, 1987.
- [75] B. t. Have, T. Hartman, N. Moonen, and F. Leferink, “Inclination of Fast Changing Currents Effect the Readings of Static Energy Meters,” in *2019 International Symposium on Electromagnetic Compatibility - EMC EUROPE*, pp. 208–213, 2019.
- [76] L. G. Durnte and P. K. Ghosh, “Active power measurement in nonsinusoidal environments,” *IEEE Transactions on Power Systems*, vol. 15, no. 3, pp. 1142–1147, 2000.
- [77] T. Hartman, M. Pous, M. A. Azpúrua, F. Silva, and F. Leferink, “On-site Waveform Characterization at Static Meters Loaded with Electrical Vehicle Chargers,” in *2019 International Symposium on Electromagnetic Compatibility - EMC EUROPE*, pp. 191–196, 2019.
- [78] Z. Marais, H. van den Brom, G. Rietveld, R. van Leeuwen, D. Hoogenboom, and J. Rens, “Sensitivity of static energy meter reading errors to changes in non-sinusoidal load conditions,” in *2019 International Symposium on Electromagnetic Compatibility - EMC EUROPE*, pp. 202–207, IEEE, 9 2019.

Bibliography

- [79] O. Andrzej and M. Piotr, “Testing Of Energy Meters Under Three-Phase Determined And Random Nonsinusoidal Conditions,” *Metrology and Measurement Systems*, vol. 21, no. 2, p. 217, 2014.
- [80] P. S. Wright, G. Rietveld, F. Leferink, H. E. V. d. Brom, F. R. I. Alonso, J. P. Braun, K. Ellingsberg, M. Pous, and M. Svoboda, “Evaluation of EMI Effects on Static Electricity Meters,” in *2018 Conference on Precision Electromagnetic Measurements (CPEM 2018)*, pp. 1–2, 2018.
- [81] R. Quijano Cetina, Y. Seferi, S. M. Blair, and P. S. Wright, “Energy Metering Integrated Circuit Behavior beyond Standards Requirements,” *Energies*, vol. 14, no. 2, 2021.
- [82] F. Leferink, “Conducted Interference, Challenges and Interference Cases,” *IEEE Electromagnetic Compatibility Magazine*, vol. 4, no. 1, pp. 78–85, 2015.
- [83] A. Ortiz, M. Lehtonen, M. Mañana, C. J. Renedo, S. Muranen, and L. I. Egufluz, “Evaluation of Energy Meters’ Accuracy Based on a Power Quality Test Platform,” *Electric Power Components and Systems*, vol. 35, pp. 221–237, 2 2007.
- [84] A. Domijan, E. Embriz-Santander, A. Gilani, G. Lamer, C. Stiles, and C. W. Williams, “Watthour meter accuracy under controlled unbalanced harmonic voltage and current conditions,” 1996.
- [85] A. Bernieri, G. Betta, L. Ferrigno, and M. Laracca, “Electrical energy metering in compliance with recent european standards,” in *2012 IEEE International Instrumentation and Measurement Technology Conference Proceedings*, pp. 1541–1545, 2012.
- [86] R. P. B. da Silva, R. Quadros, H. R. Shaker, and L. C. P. da Silva, “Analysis of the Electrical Quantities Measured by Revenue Meters Under Different Voltage Distortions and the Influences on the Electrical Energy Billing,” *Energies*, vol. 12, p. 4757, 12 2019.

Bibliography

- [87] L. Bartolomei, D. Cavaliere, A. Mingotti, L. Peretto, and R. Tinarelli, “Testing of Electrical Energy Meters Subject to Realistic Distorted Voltages and Currents,” *Energies*, vol. 13, p. 2023, 4 2020.
- [88] B. t. Have, T. Hartman, N. Moonen, and F. Leferink, “Misreadings of Static Energy Meters due to Conducted EMI caused by Fast Changing Current,” in *2019 Joint International Symposium on Electromagnetic Compatibility, Sapporo and Asia-Pacific International Symposium on Electromagnetic Compatibility (EMC Sapporo/APEMC)*, pp. 445–448, 6 2019.
- [89] P. Buckley, “Analog Devices unveils new generation of energy metering ics to deliver highest accuracy for billing and power quality monitoring applications — EE Times,” *EE Times*, 2009.
- [90] H. Sharma, M. Rylander, and D. Dorr, “Grid Impacts Due to Increased Penetration of Newer Harmonic Sources,” *IEEE Transactions on Industry Applications*, vol. 52, pp. 99–104, 1 2016.
- [91] “NPL Power Quality Waveform Library. <http://resource.npl.co.uk/waveform/>.”
- [92] A. M. Blanco, M. Gupta, A. G. de Castro, S. K. Ronnberg, and J. A. Meyer, “Impact of flat-top voltage waveform distortion on harmonic current emission and summation of electronic household appliances,” *Renewable energy & power quality journal*, vol. 1, pp. 698–703, 2018.
- [93] D. Agudelo-Martínez and A. Pavas, “Measurement and simulation of power quality disturbances between 2–150 kHz from compact fluorescent lamps,” in *2018 18th International Conference on Harmonics and Quality of Power (ICHQP)*, pp. 1–6, 5 2018.
- [94] T. Hartman, R. Grootjans, N. Moonen, and F. Leferink, “The Effects of Falling and Rising Edge Dimming on Static Energy Meter Errors,” in *Proceedings 2021 Asia-Pacific International Symposium on Electromagnetic Compatibility, APEMC 2021*, Proceedings Asia-Pacific International Symposium on Electromagnetic Compatibility (APEMC), (United States), IEEE, 11 2021.

Bibliography

- [95] IEEE, “IEEE Standard for Transitions, Pulses, and Related Waveforms,” 2011.
- [96] S. Edwards, D. Bobick, and S. Weinzierl, “Impact of harmonic current on energy meter calibration,” in *IEEE 2011 EnergyTech*, pp. 1–6, 2011.
- [97] V. H. F. Brito, G. Y. Kume, M. S. Quinalia, M. A. Sachetti, R. P. B. Silva, W. A. Souza, and L. C. P. Silva, “Analysis of the influence of non-linear loads on the measurement and billing of electrical energy compared with the CPT,” in *2016 17th International Conference on Harmonics and Quality of Power (ICHQP)*, pp. 617–622, 2016.
- [98] “RIGOL DG952 Two channel Arbitrary Waveform Generator. Datasheet. https://telonicinstruments.co.uk/rigol-uk/DG/Rigol_DG952_Waveform_Generator_Datasheet.pdf.”
- [99] NI, “LabVIEW,” 2020.
- [100] I. V. Florinsky, “Chapter 5 - Errors and Accuracy,” in *Digital Terrain Analysis in Soil Science and Geology (Second Edition)* (I. V. Florinsky, ed.), pp. 149–187, Academic Press, second edi ed., 2016.
- [101] D. B. Williams and V. Madisetti, *Digital Signal Processing Handbook*. USA: CRC Press, Inc., 1st ed., 1997.
- [102] W. A. D. Koon, “Current Sensing for Energy Metering.”
- [103] P. Minciunescu, “AN-1076 Calibrating an ADE7878-Based, 3-Phase Energy Meter,” tech. rep., Analog Devices, 2010.